HAL
open science

ORCHIDEE-MICT (v8.4.1), a land surface model for the high latitudes: model description and validation

Matthieu Guimberteau, Dan Zhu, Fabienne Maignan, Ye Huang, Chao Yue, Sarah Dantec-Nédélec, Catherine Ottle, Albert Jornet-Puig, Ana Bastos, Pierre Laurent, et al.

To cite this version:

Matthieu Guimberteau, Dan Zhu, Fabienne Maignan, Ye Huang, Chao Yue, et al.. ORCHIDEE-MICT (v8.4.1), a land surface model for the high latitudes: model description and validation. Geoscientific Model Development, 2018, 11 (1), pp.121 - 163. 10.5194/gmd-11-121-2018 . hal-01806766

HAL Id: hal-01806766

https://hal.science/hal-01806766v1

Submitted on 8 Sep 2020

HAL is a multi-disciplinary open access archive for the deposit and dissemination of scientific research documents, whether they are published or not. The documents may come from teaching and research institutions in France or abroad, or from public or private research centers.

L'archive ouverte pluridisciplinaire **HAL**, est destinée au dépôt et à la diffusion de documents scientifiques de niveau recherche, publiés ou non, émanant des établissements d'enseignement et de recherche français ou étrangers, des laboratoires publics ou privés.

Geosci. Model Dev., 11, 121–163, 2018
https://doi.org/10.5194/gmd-11-121-2018
© Author(s) 2018. This work is distributed under
the Creative Commons Attribution 3.0 License.

Geoscientific Model Development
Open Access

ORCHIDEE-MICT (v8.4.1), a land surface model for the high latitudes: model description and validation

Matthieu Guimberteau[1,*], Dan Zhu[1,*], Fabienne Maignan[1], Ye Huang[1], Chao Yue[1], Sarah Dantec-Nédélec[1], Catherine Ottlé[1], Albert Jornet-Puig[1], Ana Bastos[1], Pierre Laurent[1], Daniel Goll[1], Simon Bowring[1], Jinfeng Chang[2], Bertrand Guenet[1], Marwa Tifafi[1], Shushi Peng[3], Gerhard Krinner[4], Agnès Ducharne[5], Fuxing Wang[6], Tao Wang[7,8], Xuhui Wang[1,9], Yilong Wang[1], Zun Yin[1], Ronny Lauerwald[10,1,11], Emilie Joetzjer[1,12], Chunjing Qiu[1], Hyungjun Kim[13], and Philippe Ciais[1]

[1]Laboratoire des Sciences du Climat et de l'Environnement, LSCE/IPSL, CEA – CNRS – UVSQ, Université Paris-Saclay, 91191 Gif-sur-Yvette, France
[2]Sorbonne Universités (UPMC), CNRS-IRD-MNHN, LOCEAN/IPSL, 4 place Jussieu, 75005 Paris, France
[3]Sino–French Institute for Earth System Science, College of Urban and Environmental Sciences, Peking University, Beijing 100871, China
[4]CNRS, Univ. Grenoble Alpes, Institut des Géosciences de l'Environnement (IGE), 38000 Grenoble, France
[5]UMR 7619 METIS, Sorbonne Universités, UPMC, CNRS, EPHE, 4 place Jussieu, 75005 Paris, France
[6]Laboratoire de Météorologie Dynamique, Ecole Polytechnique, 91128 Palaiseau, France
[7]Key Laboratory of Alpine Ecology and Biodiversity, Institute of Tibetan Plateau Research, Chinese Academy of Sciences, Beijing 100085, China
[8]CAS Center for Excellence in Tibetan Plateau Earth Sciences, Chinese Academy of Sciences, Beijing 100085, China
[9]Laboratoire de Météorologie Dynamique, Université Pierre et Marie Curie, 75005 Paris, France
[10]Université Libre de Bruxelles, Belgium
[11]University of Exeter, Exeter, UK
[12]CNRS, Université Paul Sabatier, ENFA; UMR5174 EDB (Laboratoire Evolution et Diversité Biologique), 118 route de Narbonne, 31062 Toulouse, France
[13]Institute of Industrial Science, The University of Tokyo, Tokyo, Japan
[*]These authors contributed equally to this work.

Correspondence: Matthieu Guimberteau (matthieu.guimberteau@lsce.ipsl.fr) and Dan Zhu (dan.zhu@lsce.ipsl.fr)

Received: 17 May 2017 – Discussion started: 16 June 2017
Revised: 4 October 2017 – Accepted: 27 November 2017 – Published: 15 January 2018

Abstract. The high-latitude regions of the Northern Hemisphere are a nexus for the interaction between land surface physical properties and their exchange of carbon and energy with the atmosphere. At these latitudes, two carbon pools of planetary significance – those of the permanently frozen soils (permafrost), and of the great expanse of boreal forest – are vulnerable to destabilization in the face of currently observed climatic warming, the speed and intensity of which are expected to increase with time. Improved projections of future Arctic and boreal ecosystem transformation require improved land surface models that integrate processes specific to these cold biomes. To this end, this study lays out relevant new parameterizations in the ORCHIDEE-MICT land surface model. These describe the interactions between soil carbon, soil temperature and hydrology, and their resulting feedbacks on water and CO_2 fluxes, in addition to a recently developed fire module. Outputs from ORCHIDEE-MICT, when forced by two climate input datasets, are extensively evaluated against (i) temperature gradients between the atmosphere and deep soils, (ii) the hydrological components comprising the water balance of the largest high-latitude basins, and (iii) CO_2 flux and carbon stock observations. The model performance is good with respect to empirical data, despite a simulated excessive plant water stress and

a positive land surface temperature bias. In addition, acute model sensitivity to the choice of input forcing data suggests that the calibration of model parameters is strongly forcing-dependent. Overall, we suggest that this new model design is at the forefront of current efforts to reliably estimate future perturbations to the high-latitude terrestrial environment.

1 Introduction

At the high latitudes, the complex coupling between soil thermal and hydraulic processes, snowpack properties, and plant and soil carbon pools is of great importance. Snow accumulation and freezing of soil water lead to a net storage of water from October to April. Through the processes of snowmelt and the onset of soil thaw in spring, water is made available for plant uptake and growth. Simultaneously, however, much of this is "lost" as runoff to rivers, causing peak discharge rates in May–June (Yang et al., 2003) and the flooding of large flatland areas from May to September (Papa et al., 2008; Biancamaria et al., 2009). In summertime, the peak in incident solar radiation causes a temperature maximum that increases water evaporative demand on the land surface. Many boreal and Arctic regions thus have a negative water balance in summer (Schulze et al., 1999), which may impose powerful constraints on plant growth. Siberian and Canadian boreal forests have thus been shown to experience water stress, with ratios of surface sensible to latent heat flux of up to ~ 2 (Jarvis et al., 1997; Baldocchi et al., 1997; Schulze et al., 1999) causing further heating of the near-surface atmosphere.

These large seasonal shifts of the high-latitude water balance – how water input from precipitation is shared between changes in water storage in snow, ice and soil moisture, and balanced against losses from evapotranspiration, sublimation and river discharge – can now be better assessed and evaluated using state-of-the-art observation datasets. In addition, in terms of realistic process representation, land surface models (LSMs) focusing on high-latitude phenomena require the inclusion of the following non-exhaustive series of pivotal hydrological and biogeochemical interactions.

1. A representation of permafrost physics and seasonal freeze–thaw cycles, which determine the soil hydrologic and thermal budgets and the volume and timing of lateral water flows to rivers.

2. The impact of winter snow acting as an insulating "barrier" between soils and overlying air from fall to early spring. These have subsequent effects on soil temperature and water content, feeding back onto snow thickness itself.

3. The seasonal mediation of plant water availability via snowmelt water, transpiration losses and the depth of the permafrost table (active layer thickness), which in turn determine the availability of the lateral water flows that feed rivers in the warmer months.

4. The limitations on plant productivity and biomass due to acute climatic conditions in high-latitude regions. These primarily involve biotically prohibitive cold temperatures from fall to late spring, low soil moisture in dry-summer regions, and fire events caused by hot and dry conditions.

5. The buildup of large soil carbon stocks under cold conditions through the slow burial of organic matter in the permafrost via cryoturbation and sedimentary soil formation processes (e.g., Hugelius et al., 2013; Tarnocai et al., 2009).

6. Feedbacks between high soil carbon concentrations and profiles of soil temperature, water and permafrost carbon content (e.g., Lawrence and Slater, 2008; Decharme et al., 2016).

We represent the above processes in an updated version of the ORCHIDEE LSM (ORganizing Carbon and Hydrology in Dynamic EcosystEms), known as ORCHIDEE-MICT (aMeliorated Interactions between Carbon and Temperature), which we describe in this study. Since the comprehensive description of the ORCHIDEE model by Krinner et al. (2005), the model has gone through major modifications and improvements; we present here the major ones linked to high-latitude processes. ORCHIDEE-MICT is evaluated over the last 2 to 3 decades (depending on the variable) against empirically generated datasets. Against these, we are able to evaluate model performance regarding the distribution of permafrost and the effect of snow on soil thermics (mechanisms 1 and 2); the different components of the water cycle over a wide range of high-latitude basins (mechanism 3); plant primary productivity as constrained by high-latitude conditions (mechanisms 3 and 4); and replication of soil carbon stocks and feedback dynamics (mechanisms 5 and 6).

2 ORCHIDEE model overview

The starting point for our updated land surface model (ORCHIDEE-MICT) is ORCHIDEE-TRUNK revision 3976. As detailed in Sect. 3, its description of soil temperature and vertical water transport dynamics is based on coupled diffusion equations with identical vertical discretization (F. Wang et al., 2016), and includes soil freezing, its effect on water infiltration, and phase change-induced heat sources and sinks in the soil column (Gouttevin et al., 2012a). The snow model described by Wang et al. (2013) is incorporated into this version, where snow is discretized into three layers of variable thickness, conductivity and density, accounting for snow liquid water content (Boone and Etchevers, 2001). In terms of large-scale hydrology, a river routing scheme including floodplains and their dynamics

(d'Orgeval et al., 2008; Guimberteau et al., 2012) is coupled to simulated grid-cell runoff (Sect. 3.2), permitting the calculation of "natural" river discharge (i.e., in the absence of dams or human water withdrawals).

The carbon cycle model includes half-hourly photosynthesis (GPP), daily allocation of GPP assimilates to autotrophic respiration and eight plant biomass pools (foliage, roots, above-/below-ground sapwood and heartwood, fruits and carbon reserves), and prognostic phenology (Botta et al., 2000). These pools are characterized by different turnover times, mortality rates and subsequent litter and soil carbon decomposition rates. Litter carbon is funneled between structural and metabolic fractions, and soil carbon between active, slow and passive pools, following Parton et al. (1987).

The model divides vegetation into 13 plant functional types (PFTs). Each PFT follows the same suite of equations but with PFT-specific parameter values and phenology functions (Krinner et al., 2005). PFT fractions are assigned to three soil tiles corresponding to bare soil, short vegetation (grass and crop PFTs) and forests (all tree PFTs). The soil moisture budget of each soil tile is calculated separately, but different PFTs in the same soil tile interact as they share the same soil moisture source. While transpiration is calculated separately for each PFT, and soil moisture for each soil tile, the energy budget of a grid cell with multiple PFTs is calculated using the area-weighted average of those PFTs. This in turn defines mean grid-cell land surface temperature, giving the upper boundary condition for the vertically discretized soil thermal module.

Temperature, water and carbon interactions described in ORCHIDEE revision 3976 are summarized in Fig. 1 by the black arrows. Air temperature and humidity impact phenology, photosynthesis, autotrophic respiration and the water and heat fluxes comprising the surface energy budget. Soil moisture in the root zone modulates photosynthesis and transpiration, which depends on wilting point and field capacity. In ORCHIDEE revision 3976, while soil carbon decomposition is impacted by soil water and temperature, soil carbon stocks themselves exert no feedback on the soil physical state.

The key model developments presented here in ORCHIDEE-MICT (v8.4.1) thus include the feedback effects of soil organic carbon (SOC) concentration on both soil thermic and soil water dynamics (Fig. 1, red arrows). Because these SOC-affected soil physics alter the above- and below-ground components of the carbon cycle, as well as plant transpiration via hydraulic stress, we can expect complex indirect effects on the energy, water and carbon budgets (Fig. 1). Note that in the simulations here, soil thermal and hydrological modules read a prescribed observational SOC map (NCSCD in permafrost regions and HWSD in non-permafrost regions) instead of the prognostically simulated SOC, to exclude the impact of bias in the carbon cycle module, for the purpose of model evaluation for the present day in this study. Note that several other updates were implemented in ORCHIDEE-TRUNK (revision 3976) and passed to ORCHIDEE-MICT (v8.4.1), including a revised background albedo based on satellite observations, and updates of the photosynthesis scheme. These will be described in an upcoming paper for ORCHIDEE-TRUNK (version close to revision 3976) that will be used for the CMIP6 exercise. In the following, we describe the parameterizations that define ORCHIDEE-MICT (v8.4.1).

3 High-latitude processes in the initial ORCHIDEE version

3.1 Soil freezing and snow processes

The soil freezing scheme developed by Gouttevin et al. (2012a) describes phase changes of soil water, simulating the latent heat exchanges involved in the freezing and melting of soil water, and subsequent changes in thermal and hydrological ground properties. Soil heat conductivity and heat capacity are dependent on soil ice content. The hydraulic conductivity of the soil is parameterized according to its liquid water content and decreases with the frozen soil fraction. Heat transfer through the soil column is represented by a one-dimensional heat conduction equation, with latent heat acting as a source or sink term (Gouttevin et al., 2012a), in the following function:

$$c\,\frac{\partial T}{\partial t} = \frac{\partial}{\partial z}\left(\lambda \frac{\partial T}{\partial z}\right) + \rho_{\mathrm{ice}}\, L\, \frac{\partial \theta_{\mathrm{ice}}}{\partial t}, \tag{1}$$

where c is volumetric soil heat capacity ($\mathrm{J\,K^{-1}\,m^{-3}}$); T is soil temperature (K); λ is soil thermal conductivity ($\mathrm{J\,m^{-1}\,s^{-1}\,K^{-1}}$); ρ_{ice} is ice density ($\mathrm{kg\,m^{-3}}$); L is latent heat of fusion ($\mathrm{J\,kg^{-1}}$); θ_{ice} is volumetric ice content ($\mathrm{m^3\,m^{-3}}$); t is time (s) and z is depth (m). In ORCHIDEE-MICT, this equation is discretized on the 32 vertical layers of the model with a total soil depth of 38 m (Fig. S1 in the Supplement). Note that the soil hydrology has only 11 layers up to 2 m, so the volumetric contents of water and ice below 2 m take the values of the bottom layer (i.e., the 11th layer).

Snowpack is represented by a three-layer snow model of intermediate complexity, as described in Wang et al. (2013). This scheme was implemented to resolve the energy and water budgets inside the snowpack, accounting for thawing and refreezing of liquid water. The snow model produces prognostic snow temperature, density and SWE for the three snow layers. Modifications were recently implemented to represent snowpack sub-grid-scale variability. A snow cover fraction over the grid cell was introduced as a function of SWE. This was used for improving albedo and surface temperature estimates. Although this snow cover fraction was calculated for glacier and vegetated-surface areas separately, it is not dependent on the vegetation cover. Additional modifications were implemented (uniformization of the energy budget calculation, update of the snow-covered vegetation albedo…)

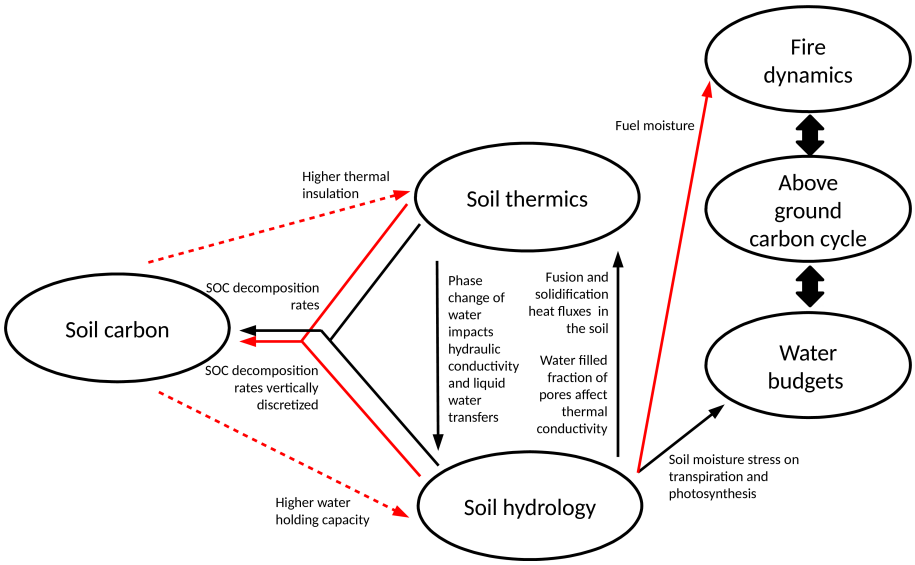

Figure 1. Temperature, water and carbon interactions in the initial version of ORCHIDEE (black), and processes included in ORCHIDEE-MICT in this study (red). Note that in the simulations in this study, the soil thermics and hydrology modules read a prescribed observation-based soil carbon map (see Eq. 9), which is independent of the prognostically simulated SOC by the carbon module; thus, the two red arrows here are dashed lines.

and will be described in the upcoming CMIP6 ORCHIDEE paper as mentioned in Sect. 2.

3.2 Soil hydrology and river routing

ORCHIDEE simulates soil water fluxes and storage through a multi-layer soil hydrology scheme described by de Rosnay et al. (2000, 2002) and Campoy et al. (2013). Soil moisture is redistributed in the column by solving the Richards equation for vertical unsaturated flow under the effect of root uptake. The hydraulic conductivity and diffusivity depend on soil moisture, following the Mualem–van Genuchten model (Mualem, 1976); (Van Genuchten, 1980), and using parameters defined by Carsel and Parrish (1988). These variables depend on the dominant soil texture in each grid cell, based on the 12 USDA texture classes provided at the 0.08° resolution from Reynolds et al. (2000). For frozen soils, the decrease in the hydraulic conductivity (Gouttevin et al., 2012a) reduces infiltration into the soil and drainage, and increases surface runoff. The 2 m soil column is divided into 11 layers, with layer thickness increasing geometrically with depth (Fig. S1). The saturated hydraulic conductivity is modified according to the scheme in d'Orgeval et al. (2008). This decreases exponentially below a top-30 cm depth boundary to account for increased soil compaction, as suggested by Beven and Germann (1982), and increases above that boundary towards the soil surface due to the enhanced infiltration capacity afforded by vegetative roots, whose presence increases soil porosity in the root zone (Beven, 1984). The canopy throughfall rate and soil hydraulic conductivity govern the partitioning between surface runoff and soil infiltration. This partitioning involves a time-splitting procedure inspired by Green and Ampt (1911), describing the propagation of the wetting front. The second physical factor contributing to total runoff is free gravitational drainage at the bottom of the soil.

The runoff routing module (Polcher, 2003; Ngo-Duc et al., 2005; Guimberteau et al., 2012) aggregates surface runoff and drainage produced at a 30 min time step to calculate daily flow between grid cells and discharge to the ocean. Grid cells are subdivided into basins in which water is transferred through a series of linear reservoirs along the drainage network, derived from a 0.5° resolution dataset (Vörösmarty et al., 2000; Oki et al., 1999). In a given basin, a "slow" reservoir collects drainage water, while a "fast" reservoir collects surface runoff, each with different linear response timescales. Corresponding outflows are transferred to the stream reservoir of the downstream basin. The process is fully detailed in Guimberteau et al. (2012).

The routing scheme includes a parameterization of floodplains (d'Orgeval et al., 2008; Guimberteau et al., 2012), the maximum extent of which is prescribed by the GLWD (Global Lakes and Wetlands Database) map (Lehner and Döll, 2004). In grid cells with flooded areas, river discharge from upstream basins is diverted to a floodplain reservoir, which then feeds a delayed return flow back to the stream reservoir of the basin.

4 New processes and parameterizations

4.1 Soil carbon discretization

In ORCHIDEE-MICT, the three soil carbon pools (active, slow and passive) share a common 32-layer discretization scheme with that of soil temperature, to a maximum depth of 38 m. Carbon inflows to the soil pools from decomposed litter are partitioned along this depth using an exponential function that corresponds to the prescribed PFT root profile. Decomposition of soil carbon is calculated at each layer as a function of soil temperature, moisture, and texture (Koven et al., 2009; Zhu et al., 2016). Vertical mixing of soil carbon due to cryoturbation (mixing of soil layers induced by repeated freeze–thaw cycles) and bioturbation are accounted for by adding a diffusion term in the soil carbon equation:

$$\frac{\partial C_i(z,t)}{\partial t} = I_i(z,t) - g_i(z,t)\,C_i(z,t) + D\,\frac{\partial C_i^2(z,t)}{\partial z^2}, \qquad (2)$$

where $C_i(z,t)$ is carbon content of pool i at depth z and time t ($\mathrm{g\,C\,m^{-3}}$); $I_i(z,t)$ is carbon input ($\mathrm{g\,C\,m^{-3}\,d^{-1}}$); $g_i(z,t)$ is decomposition rate ($\mathrm{d^{-1}}$); D is diffusive mixing rate, set as $10^{-3}\,\mathrm{m^2\,yr^{-1}}$ through the active layer, and decreases linearly to zero at 3 m in permafrost regions, to represent cryoturbative mixing (Koven et al., 2009), and set as $10^{-4}\,\mathrm{m^2\,yr^{-1}}$ above 2 m in non-permafrost regions to represent bioturbation (Koven et al., 2013).

4.2 SOM-dependent soil thermal and hydraulic parameters

Soil organic matter (SOM) significantly modifies soil thermal and hydraulic properties. SOM lowers thermal conductivity and increases heat capacity (e.g., Lawrence and Slater, 2008; Decharme et al., 2016), and increases soil porosity, which in turn increase saturated hydraulic conductivity and available water capacity (e.g., Hudson, 1994; Morris et al., 2015). As a consequence, the presence of SOM modulates heat transfer from the surface through the soil column, typically leading to cooler soil temperature during summer. SOM-effected increases in soil water holding capacity also enhance plant available water and thus primary productivity (Krull et al., 2004) and transpiration. SOM impacts on soil thermics and hydraulics have previously been parameterized in the global LSMs CLM (Lawrence and Slater, 2008), JULES (Chadburn et al., 2015b) and ISBA (Decharme et al., 2016). In ORCHIDEE, SOM thermal insulation was previously investigated by Koven et al. (2009), but its parameterization was imbedded in a prior model version which employed bucket-type soil hydrology. This, however, is not applicable to ORCHIDEE-MICT, which uses a new vertically discretized hydrology scheme and its coupling with the thermal module. In addition, the Koven et al. (2009) study did not include SOM effects on soil hydraulic properties, which are addressed in ORCHIDEE-MICT and described in detail below.

Thermal conductivity and heat capacity

By default, soil thermal conductivity and heat capacity in ORCHIDEE are calculated in each soil layer as empirical functions of the 12 USDA soil texture classifications (see Table S1 in the Supplement) and soil water and ice contents, following F. Wang et al. (2016):

$$\lambda_i = Ke_i\lambda_{i,\mathrm{sat}} + (1 - Ke_i)\lambda_{i,\mathrm{dry}}, \qquad (3)$$

with

$$\lambda_{i,\mathrm{sat}} = \lambda_{i,\mathrm{solid}}^{(1-\theta_{i,\mathrm{sat}})}\,\lambda_{\mathrm{liq}}^{\left(\theta_{i,\mathrm{sat}}\frac{\theta_{i,\mathrm{liq}}}{\theta_{i,\mathrm{liq}}+\theta_{i,\mathrm{ice}}}\right)}\,\lambda_{\mathrm{ice}}^{\left(\theta_{i,\mathrm{sat}}\frac{\theta_{i,\mathrm{ice}}}{\theta_{i,\mathrm{liq}}+\theta_{i,\mathrm{ice}}}\right)}, \qquad (4)$$

$$c_i = c_{i,\mathrm{dry}} + \theta_{i,\mathrm{liq}}\,c_{\mathrm{liq}} + \theta_{i,\mathrm{ice}}\,c_{\mathrm{ice}}, \qquad (5)$$

where $\lambda_{i,\mathrm{sat}}$ and $\lambda_{i,\mathrm{dry}}$ are saturated and dry thermal conductivities for layer i; λ_{liq} and λ_{ice} are thermal conductivities of liquid water and ice, equaling 0.57 and 2.2, respectively ($\mathrm{W\,m^{-1}\,K^{-1}}$); $\lambda_{i,\mathrm{solid}}$ is thermal conductivity of soil solids (see Table S1); c_{liq} and c_{ice} are heat capacities of liquid water and ice, equaling $4.18\,10^6$ and $2.11\,10^6$, respectively ($\mathrm{J\,K^{-1}m^{-3}}$); c_{dry} is dry soil heat capacity depending on soil texture; $\theta_{i,\mathrm{sat}}$ is volumetric moisture content at saturation (porosity), and it varies with soil textures; $\theta_{i,\mathrm{liq}}$ and $\theta_{i,\mathrm{ice}}$ are prognostic volumetric liquid water and ice contents ($\mathrm{m^3\,m^{-3}}$) that are computed by the soil hydrology model; Ke_i is the Kersten number given by the following.

For unfrozen soils:

$$Ke_i = \begin{cases} \log_{10}(S_r) + 1 \\ 0.7\log_{10}(S_r) + 1 \\ 0 \end{cases} \text{if} \begin{cases} S_r > 0.1 \\ 0.05 < S_r \leq 0.1 \\ S_r \leq 0.05 \end{cases} \qquad (6)$$

with

$$S_r = \frac{\theta_i}{\theta_{i,\mathrm{sat}}}. \qquad (7)$$

For frozen soils:

$$Ke_i = S_r, \qquad (8)$$

where S_r is the degree of saturation.

To account for the impacts of organic carbon on soil thermal properties in ORCHIDEE-MICT, we follow Lawrence and Slater (2008) in assuming that soil physical properties are weighted averages of mineral soil (as the default values in standard ORCHIDEE) and pure organic soil, with the organic soil fraction $f_{i,\mathrm{soc}}$ calculated as

$$f_{i,\mathrm{soc}} = \min\left(1, \frac{\rho_{i,\mathrm{soc}}}{\rho_{\mathrm{soc,\,max}}}\right), \qquad (9)$$

where $\rho_{i,\mathrm{soc}}$ is the carbon content for layer i ($\mathrm{kg\,C\,m^{-3}}$), derived from an observation-based soil organic carbon map

from NCSCD (Hugelius et al., 2013) in permafrost regions and from HWSD (FAO, 2012) in non-permafrost regions, after linear vertical interpolation from their original soil horizons to fit ORCHIDEE-MICT vertical layers; $\rho_{\mathrm{soc,\,max}}$ equals $130\,\mathrm{kg\,C\,m^{-3}}$, a typical soil carbon density of peat (Lawrence and Slater, 2008). Therefore, the parameters in Eqs. (3)–(7) are calculated as

$$P_i = (1 - f_{i,\mathrm{soc}})\, P_{\mathrm{mineral}} + f_{i,\mathrm{soc}}\, P_{\mathrm{soc}}, \tag{10}$$

where P_i represents different properties $\lambda_{i,\mathrm{dry}}$, $\lambda_{i,\mathrm{solid}}$, $c_{i,\mathrm{dry}}$, and $\theta_{i,\mathrm{sat}}$. The values of P_{mineral} for each soil texture and P_{soc} are listed in Table S1. Note that here we followed Lawrence and Slater (2008) to use linear weighting organic and mineral soil properties, while in some other models like JULES (Chadburn et al., 2015a) and ISBA (Decharme et al., 2016), soil thermal conductivities are calculated as geometric averages of organic and mineral soils, consistent with the treatment for soil water and ice (Eq. 4). The geometric averaging method increases the effect of the organic fraction compared to arithmetic averages, and would be tested in ORCHIDEE-MICT in future developments.

Available water capacity

Plant available water capacity, defined as the difference in the amount of water held by each soil layer between field capacity (θ_{fc}) and permanent wilting point (θ_{wp}), determines the capacity of the soil to store and supply water for plants, and is therefore an important aspect of soil fertility (Hudson, 1994). For mineral soils in ORCHIDEE, θ_{fc} and θ_{wp} are derived from measurements of the soil matric potential at field capacity and wilting point, based on the soil water retention curve described by the van Genuchten equation (Van Genuchten, 1980):

$$\theta = \frac{(\theta_{\mathrm{sat}} - \theta_r)}{\left[1 + (\alpha\,(-\Psi))^n\right]^{\left(1-\frac{1}{n}\right)}} + \theta_r, \tag{11}$$

where ψ is soil matric potential (kPa), and $\psi = -33\,\mathrm{kPa}$ (or $-10\,\mathrm{kPa}$ for the three sandy soils; see Table S2) corresponds to field capacity θ_{fc}, while $\psi = -1500\,\mathrm{kPa}$ corresponds to wilting point θ_{wp} for all textures; θ_r is the residual volumetric water content ($\mathrm{m^3\,m^{-3}}$); α and n are empirical fitting coefficients, with their values for different soil textures listed in Table S2.

SOC has been shown to significantly increase water retention (Rawls et al., 2003). To parameterize this SOM effect, we assume that θ_r and the coefficients in Eq. (11) do not change with carbon content, while porosity θ_{sat} increases with organic carbon (Eq. 10). Therefore, both θ_{fc} and θ_{wp} increase under higher carbon contents, but θ_{fc} increases faster, resulting in a higher available water capacity (Fig. S2), consistent with the patterns observed in Hudson (1994).

4.3 Reformulation of soil hydric stress above the permafrost table

It is known that reduced soil moisture availability decreases the rate of photosynthesis, but the parameterization of this photosynthetic stress differs amongst models (Medlyn et al., 2015). ORCHIDEE-MICT lacks a fully mechanistic plant hydraulic structure that calculates plant internal water movement via constraints from water potential (ψ) and conductance of roots, stems and leaves. Instead, a stress factor, which ranges from 0 to 1, is calculated based on the relative moisture content at each soil layer. This factor is applied to stomatal conductance and mesophyll conductance, as well as the maximum RuBisCO activity rate (Vcmax) and maximum electron transport rate (Jmax), in order to account for experimentally observed effects of drought on stomatal and non-stomatal photosynthetic limitation (Zhou et al., 2014). The stress factor (γ) of water limitation is calculated as

$$\gamma_i = \frac{\theta_i - \theta_{\mathrm{wp}}}{\theta_{\mathrm{wp}} + \rho(\theta_{\mathrm{fc}} - \theta_{\mathrm{wp}})}, \tag{12}$$

$$\gamma = \sum_{i=1}^{11} \gamma_i\, w_i, \tag{13}$$

where γ_i is relative moisture content at each soil layer i, bounded between 0 and 1; ρ represents the fraction above which photosynthesis rate is not limited by soil moisture, and is set at 0.8; w_i is the weighting factor for each layer.

In the initial version of ORCHIDEE, the profile of w_i was assumed to be constant over time, although it differed between tree and grass PFTs, with the highest value at 1.5 m depth for trees and 0.37 m depth for grasses. We considered this description inappropriate for the high latitudes, and in particular for permafrost regions, where trees develop shallow and lateral roots above the permanently frozen layer (Kajimoto et al., 2003). Thus, in ORCHIDEE-MICT, w_i is modified to be a dynamic profile which optimizes plant water use, in a manner inspired by the representation given in Beer et al. (2007):

$$w_i = \frac{\gamma_i}{\sum_{i=1}^{11} \gamma_i}, \tag{14}$$

where if layer i is below the modeled active layer thickness, w_i is set to zero, and the remaining w are re-normalized to one.

4.4 Fires

The SPITFIRE (SPread and InTensity of FIRE) prognostic fire module, which has been previously integrated into and calibrated for a standard version of ORCHIDEE (Thonicke et al., 2010; Yue et al., 2014), was merged into ORCHIDEE-MICT. Ignitions were re-calibrated using the GFED4s dataset (http://www.globalfiredata.org/data.html) by using region-specific scaling factors (see Table S3)

and the exclusion of cropland fires to ensure that simulated mean annual burned area for 1997–2013 was equal to that of the GFED4s dataset. Note that this method only calibrated for mean annual regional burned area, and that simulated latitudinal distributions and grid cell spatial patterns of burned area and fire carbon emissions, and their interannual and seasonal variabilities, could still be compared with observation-based data. Deforestation and peatland fires are not explicitly simulated, but as both fire types rely on suitable weather conditions to occur, which could be partly captured by SPITFIRE (Yue et al., 2015), model simulations are expected to partially include these fire types.

5 Simulation protocol, forcing and evaluation datasets

5.1 Simulation protocol and forcings

5.1.1 Simulation setup

Two separate runs using different climate forcing input data – CRUNCEP v7 (hereafter CRUNCEP) and GSWP3 – were performed with ORCHIDEE-MICT for the terrestrial Northern Hemisphere (> 30° N) at 1° spatial resolution. Both sets of runs encompass the 20th century and the beginning of the 21st century, and were preceded by separate spin-ups for each climate dataset, forced by fixed pre-industrial conditions of atmospheric CO_2 (286 ppm) and vegetation maps. The dynamic vegetation model is de-activated throughout both runs. In order to accumulate soil organic carbon in the model, which requires substantial computing time before reaching near-equilibrium in the presence of the slow mixing processes described in Sect. 4.1, the spin-up procedure comprised three steps. (1) The full ORCHIDEE-MICT model was forced by looped climate fields over the period 1960–1990 for 100 years to reach equilibria for soil temperature, soil moisture, vegetation productivity, soil carbon inputs from dead plants, etc. We used the 1960–1990 loop, instead of pre-industrial climate, to approximate the higher Holocene temperatures relative to the "pre-industrial" period that have been reconstructed in Marcott et al. (2013). (2) A soil carbon sub-model was run for 20 000 years, forced by the outputs from the preceding step. (3) The full ORCHIDEE-MICT model was run for 100 years, forced by looped 1901–1920 climate data, to approach to the pre-industrial equilibrium for physical variables, carbon fluxes, and fast carbon pools. A final transient simulation from 1861 to 2007 (using the 1901–1920 climate loop for the period 1861–1900 due to the lack of climate forcing before the 20th century) was then run from the last year of spin-up stage 3, forced by historical climate forcing and land cover maps, and rising CO_2 concentrations, as detailed below.

5.1.2 Atmospheric forcing datasets

The use of two different forcing datasets represents a first step in documenting atmospheric-forcing-based uncertainty in model output. Runoff has been shown for instance to be particularly affected by differences in precipitation from different datasets (Fekete et al., 2004; Biancamaria et al., 2009), and by the methods to partition total precipitation volumes between rainfall and snowfall during the cold season (Haddeland et al., 2011). The bias of meteorological drivers also impacts the carbon budget (Zhao et al., 2012). A description of the two datasets used follows.

GSWP3 v0

This 3-hourly 0.5° global forcing product (1901–2007) was developed for the third phase of GSWP3 (http://hydro.iis.u-tokyo.ac.jp/GSWP3/). It is based on the 20th Century Reanalysis (20CR) version 2 performed with the NCEP land–atmosphere model (Compo et al., 2011). 20CR was dynamically downscaled to T248 (0.5°) resolution using the Global Spectral Model (GSM) by data assimilation using the spectral nudging technique (Yoshimura and Kanamitsu, 2008). Bias corrections for precipitation, temperature and longwave and shortwave downward radiations were made using the GPCC v6 (Global Precipitation Climatology Centre), CRU TS v3.21 (Climate Research Unit), and SRB (Surface Radiation Budget) datasets, respectively. Precipitation was partitioned into rainfall and snowfall referring to the ratio of the downscaled 20CR, and wind-induced undercatch correction (Motoya et al., 2002) was applied separately. We upscaled the GSWP3 forcing for 1° spatial resolution.

CRUNCEP v7

This 6-hourly 0.5° global forcing product (1901–2015) is a combination of the annually updated CRU TS v3.24 monthly climate dataset (New et al., 2000) and NCEP reanalysis (Kalnay et al., 1996). The latter is only used to generate diurnal and daily anomalies added to CRU TS monthly means, after bi-linear interpolation to the 0.5° resolution of CRU, except for the precipitations which were linearly interpolated. A threshold of 0 °C in 2 m temperature was used to partition the precipitation into rainfall and snowfall in the CRUNCEP forcing. Rainfall, cloudiness, relative humidity and temperature are taken from the CRU, while the other fields (pressure, longwave radiation, windspeed) were directly derived from NCEP (see more details at https://vesg.ipsl.upmc.fr/thredds/fileServer/store/p529viov/cruncep/readme.html). We upscaled the forcing to a 1° spatial resolution dataset, which can be found at https://vesg.ipsl.upmc.fr/thredds/catalog/store/p529viov/cruncep/V7_1901_2015/catalog.html.

Table 1. List of the datasets used for the ORCHIDEE-MICT evaluation, with their references, the original spatial resolution, and period of availability.

Dataset	Variable	Resolution	Period	URL	References
Evaluation datasets for water budget					
GRACE	TWS	1°	Jul 2003–Dec 2007	http://grace.jpl.nasa.gov	Swenson and Wahr (2006); Swenson (2012) Landerer and Swenson, 2012
GlobSnow	Snow water mass	25 km	1979–2013	www.globsnow.info	Takala et al. (2009)
GLEAM v3.0a	Evapotranspiration	0.25°	1980–2014	http://www.gleam.eu	Miralles et al. (2011)
GRDC	River discharge	–	1981–2007	http://www.bafg.de/GRDC/EN/Home/homepage_node.html	–
Naturalized discharge	River discharge	–	1981–2007	http://www.r-arcticnet.sr.unh.edu/ObservedAndNaturalizedDischarge-Website	Shiklomanov and Lammers (2009)
ESA CCI SM v2.2	Topsoil moisture	25 km	Nov 1978–Dec 2014	http://esa-soilmoisture-cci.org	–
GLEAM v3.0a	Root-zone soil moisture	0.25°	1980–2014	http://www.gleam.eu	Martens et al. (2017)
Evaluation datasets for air-to-soil temperature continuum					
ECA&D	Snow depth	–	1975–2005	http://ecad.knmi.nl/dailydata/predefinedseries.php	–
National Climate Data and Info. Archive of Env. Canada	Snow depth	–	1975–2005	http://climate.weather.gc.ca/historical_data/search_historic_data_e.html	–
USHCN	Snow depth	–	1975–2005	http://cdiac.ornl.gov/epubs/ndp/ushcn/ushcn.html	–
RIHMI-WDC	Snow depth	–	1975–2005	–	Bulygina et al. (2011)
National Meteo. Info. Center of the China Meteo. Admin.	Snow depth	–	1975–2005	–	Peng et al. (2010)
–	Surface soil temperature	25 km	2000–2011	http://doi.pangaea.de/10.1594/PANGAEA.833409	André et al. (2015)
–	In situ air and soil temperatures	–	1980–2000	–	Sherstiukov (2012)
CALM	Active-layer thickness	–	1990–2015	–	–
For Yakutia	Active-layer thickness	–	1960–1987	https://doi.org/10.1594/PANGAEA.808240	Beer et al. (2013)
Evaluation datasets for leaf area, carbon stocks and fluxes					
GIMMS	Leaf area index	0.08°	Jul 1981–Dec 2011	http://cliveg.bu.edu/modismisr/lai3g-fpar3g.html	Zhu et al. (2013)
GLASS	Leaf area index	0.05°	1982–2012	http://glcf.umd.edu/data/lai	Liang and Xiao (2012)
CAMS	NEE	1.875° × 3.75°	1979–2015	https://apps-test.ecmwf.int/datasets/data/cams-ghg-inversions	Chevallier et al. (2010)
Jena s96 v3.8	NEE	3.8° × 5.0°	1996–2015	http://www.bgc-jena.mpg.de/CarboScope/?ID=s96_v3.8	Rödenbeck (2005)
–	GPP	–	Not known	–	Campioli et al. (2015)
MTE-GPP	GPP	0.5°	1982–2010	–	Jung et al. (2009, 2011)
–	NPP	–	Not known	–	Campioli et al. (2015)
MOD17A3.005	NPP	1 km	2000–2010	–	–
NCSCD	Soil carbon inventories	0.01°	–	http://bolin.su.se/data/ncscd/netcdf.php	Hugelius et al. (2013)
SoilGrids	Soil carbon inventories	1 km	–	https://doi.org/10.5879/ecds/00000001	Hengl et al. (2014)
–	Biomass carbon stocks	0.01°	–	–	Avitabile et al. (2016)
–	Biomass carbon stocks	0.01°	–	http://www.biomasar.orghttp://www.bgc-jena.mpg.de/geodb/projects/Home.php	Thurner et al. (2014)
GFED4s	Burned area and fire emissions	0.25°	1997–2015	http://www.globalfiredata.org/data.html	van der Werf et al. (2010)

5.1.3 Vegetation and soil texture map

The ESA CCI Land Cover map (Bontemps et al., 2013) was used to produce the PFT map for ORCHIDEE. The ESA CCI land cover product is given by three maps at a 300 m spatial resolution, corresponding to the years 2010, 2005 and 2000. These maps were derived from the interpretation of MERIS full and reduced resolutions and SPOT-Vegetation time series. Land cover was classified according to the 22 classes used in the UN-LCCS (land cover classification system) scheme, which was translated into PFT fractions used in ORCHIDEE, following the cross-walking method presented by Poulter et al. (2011, 2015). Historical land use maps from the Harmonized Global Land Use dataset (Chini et al., 2014) were incorporated to reconstruct PFT fractions since 1860, following Peng et al. (2017), which will be detailed in the upcoming ORCHIDEE-TRUNK paper for CMIP6.

For soil texture, we use the 12 USDA texture classes provided at a global 0.08° resolution from Reynolds et al. (2000) and upscaled these to the resolution of the atmospheric dataset (1° × 1°). Only the dominant texture type for a grid cell is used at the 1° resolution for defining soil hydraulic parameters (Carsel and Parrish, 1988) in ORCHIDEE-MICT.

5.2 Evaluation datasets

The selected datasets used to evaluate ORCHIDEE-MICT are summarized in Table 1 and described in the Appendix. For the water budget evaluation, we selected six Arctic river basins (Fig. 2b) which are important contributors to total Arctic Ocean river inflow: the four largest Eurasian Arctic basins (Ob, Yenisei, Lena and Kolyma), the Mackenzie Basin in northwestern Canada and the Yukon Basin in Alaska. The four Eurasian basins (with the smaller Pechora and Severnaya Dvina basins) drain about two-thirds of the Eurasian Arctic landmass (Peterson et al., 2002), while the Mackenzie is the largest North American river, bringing freshwater to the Arctic Ocean (Woo and Thorne, 2003). We also evaluated the Volga Basin (Fig. 2b), which is subject to snowfall events during the year but is not underlain by permafrost, in order to compare results with the high-permafrost Arctic basins (Fig. 2a and Table S4).

6 Evaluation of the atmosphere–snow–soil continuum

In the following, we analyze model performance in replicating the transfer of heat from atmosphere to deep soils. This is done by evaluation against measured temperature gradients, starting from snow depth controls on winter ΔT, followed by evaluation of surface (skin) temperature in summer, and the

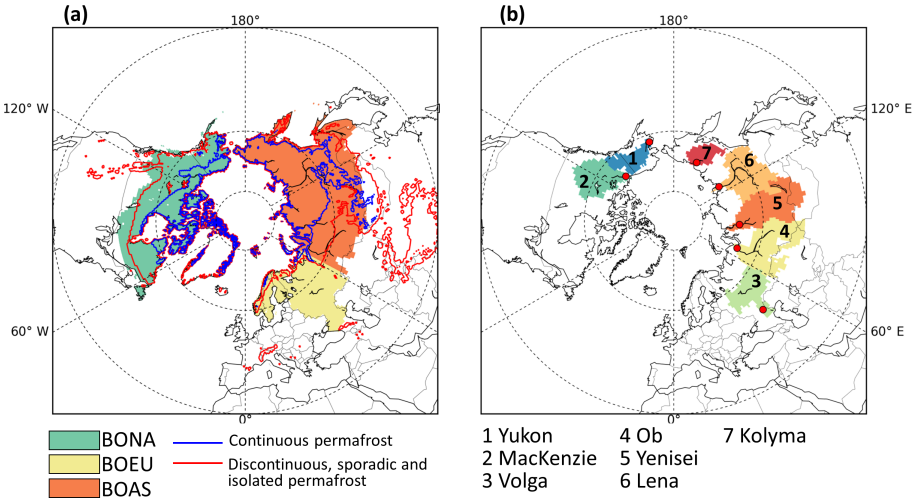

Figure 2. (a) The three high-latitude sub-regions used in this study, including boreal North America (BONA), boreal Europe (BOEU) and boreal Asia (BOAS), following McGuire et al. (2016). Blue and red lines indicate the extent of continuous permafrost and all permafrost categories, respectively, according to the IPA permafrost map (Brown et al., 2002). **(b)** The seven high-latitude basins selected for this study with the gauge stations (red circles on the map, more information in Table S4).

temperature gradients between the near-surface and deeper soils.

6.1 Snow insulation controls on the temperature gradient between air and topsoil

6.1.1 Snow depth

ORCHIDEE-MICT correctly captures the spatial distribution of maximum monthly average snow depth (Fig. 3a, b), and the seasonal decrease in snow depth from March to June (Fig. 3c), but modeled snow depth strongly depends on the atmospheric forcing used. GSWP3 climate forcing tends to produce a larger maximum snow depth than CRUNCEP, greater than those observed in all northern regions, especially over boreal Europe (BOEU) (Fig. 3c). This shows that uncertainty from climate forcing data is as large as the model bias compared with observations, making it difficult to attribute a model bias to a particular component of the snow model. However, the rate of sublimation in winter (Pomeroy et al., 1998) and the prescribed albedo value of fresh snow have been shown to be critical in determining the peak value and phase of both snow depth and SWE (T. Wang et al., 2015).

6.1.2 Snow conductivity and snow density

Mean snow density and mean snow thermal conductivity are computed at the month of maximum snow depth over the 1981–2007 period as weighted averages over the three snow layers. Gouttevin et al. (2012b) report density values of 200 $kg\,m^{-3}$ for taïga and 330 $kg\,m^{-3}$ for tundra and conductivity values of 70 $mW\,m^{-1}\,K^{-1}$ for taïga and 250 $mW\,m^{-1}\,K^{-1}$ for tundra, from Sturm and Johnson (1992) and Domine et al. (2010). These higher values over tundra were attributed to snow compaction by wind. This process is not modeled in ORCHIDEE-MICT and we thus simulate similarly high values of conductivity for both biomes (Fig. S3): approximating tundra with C3 grass PFT between 55 and 85° N, and taïga with the boreal forests PFTs between 45 and 70° N and considering only grid cells with a fraction of the dominant biome above 0.6. The model yields a mean snow conductivity of 266 ± 203 (GSWP3) and 219 ± 197 (CRUNCEP) $mW\,m^{-1}\,K^{-1}$ for tundra compared to 221 ± 113 (GSWP3) and 182 ± 100 (CRUNCEP) $mW\,m^{-1}\,K^{-1}$ for taïga and a mean density of 269 ± 102 (GSWP3) and 239 ± 103 (CRUNCEP) $kg\,m^{-3}$ for tundra and of 233 ± 67 (GSWP3) and 207 ± 63 (CRUNCEP) $kg\,m^{-3}$ for taïga. Note that a recent study (Domine et al., 2016) suggests for tundra a complex structure with depth-hoar developing at the base of snowpack during the course of the snow season, causing conductivities as low as 20 $mW\,m^{-1}\,K^{-1}$ in late winter, whereas snow-compacted upper layers have conductivities of 200 to 300 $mW\,m^{-1}\,K^{-1}$, more comparable to ORCHIDEE-MICT.

6.2 Summer land surface temperature

ORCHIDEE-MICT overestimates summer (June–August) LST by about 1.36 °C when forced by GSWP3 (Fig. 4b) and 0.49 °C by CRUNCEP (Fig. 4c). The bias is larger in northern and southern Siberia, where it can reach 4 °C. These differences may be linked to the overall underestimation of ET (see Fig. 11). This is further addressed in the Discussion (Sect. 10).

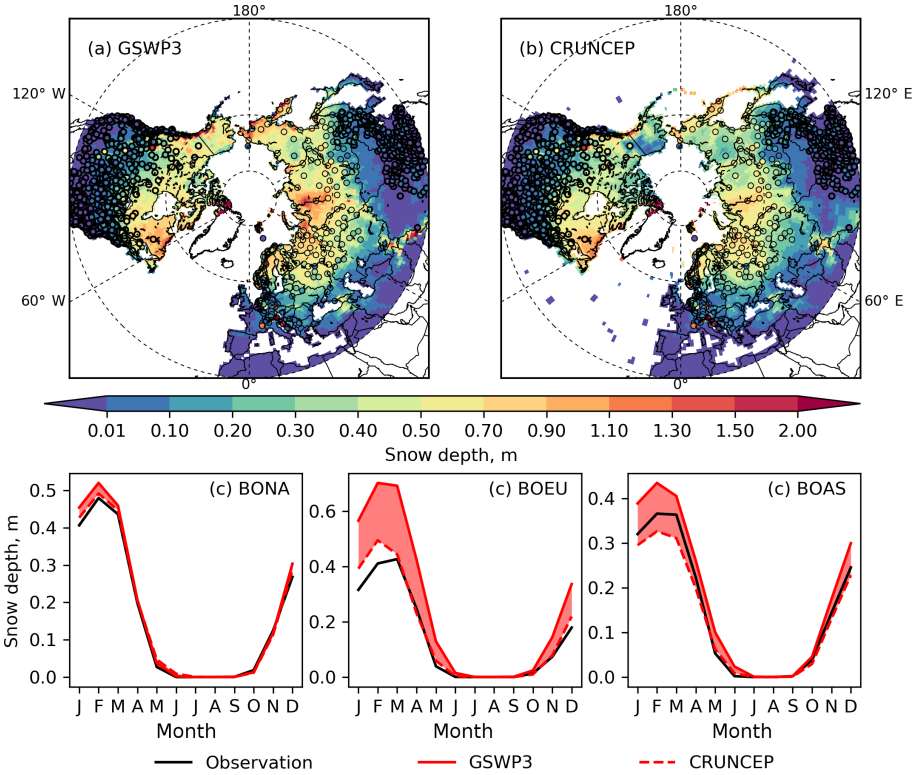

Figure 3. Maximum monthly snow depth (m) simulated (background maps) with **(a)** GSWP3 and **(b)** CRUNCEP forcings compared to observations (color filled circles), averaged over the period 1975–2005. **(c)** Monthly mean seasonal snow depth (m) from observation and the two simulations, averaged over the observation sites in the three high-latitude sub-regions (shown in Fig. 2a).

6.3 Soil temperature

The simulated spatial patterns of mean annual topsoil (0.2 m) temperature generally reproduce the observed gradient along a southwest–northeast transect in Siberia (Fig. 5a, b). However, the CRUNCEP-forced simulation results are colder than those from the GSWP3 ones as well as relative to observations in the permafrost region (Fig. 5a, b), mainly driven by a strong cold bias in CRUNCEP-based winter soil temperatures (Fig. 5c, d).

During winter, the snowpack acts as an insulating layer above the soil surface, reducing soil heat loss. Snow thus causes a large positive temperature gradient (ΔT), which is controlled by both snow depth and snow thermal properties, such as thermal conductivity, density and albedo. Generally, the model underestimates snow insulation in the early (November to January) and late (February to April) cold seasons for the same snow depth, as compared to observations (Fig. 6). This indicates that relatively congruent wintertime soil temperatures in the GSWP3-forced simulation in permafrost regions (Fig. 5c) may be due to a bias compensation from overestimated snow depth (Fig. 3) and underestimated snow thermal insulation.

A prominent component of the ΔT–snow depth relationship observed at Russian stations (black in Fig. 6) is the significantly lower insulation during the late cold season, probably due to snow compaction and densification leading to higher snow conductivity (Decharme et al., 2016). This differential sensitivity of ΔT to snow depth between the two periods is effectively captured by ORCHIDEE-MICT, despite small modeled negative ΔT values (i.e., topsoil colder than air) compared to observations at the termination of the snow season, when snow depth is diminished (<20 cm).

Summer soil temperatures are higher in the GSWP3-forced simulation relative to those of CRUNCEP, and warmer than observations from the Russian meteorological stations in continuous permafrost regions by $1\sim2$ °C on average at 0.8 and 1.6 m depths (Fig. 5c, d). Spatially, however, the bias in peak summer soil temperature varies for different regions, with a large warm bias for the Lena Basin below 0.8 m, and some cold bias for the further eastern sites (Fig. S4). This is consistent with the overestimation of ALT for Yakutia (Fig. S5) compared to the empirically derived map by Beer et al. (2013) (see Sect. 6.4). Differences between the two simulations in summertime soil temperatures may be partly driven by warmer GSWP3 land skin temperatures during summer (Fig. 4) than CRUNCEP. In addition, the cold bias in winter soil temperatures in the CRUNCEP-forced simulation might be carried over to summer via soil thermal inertia. This

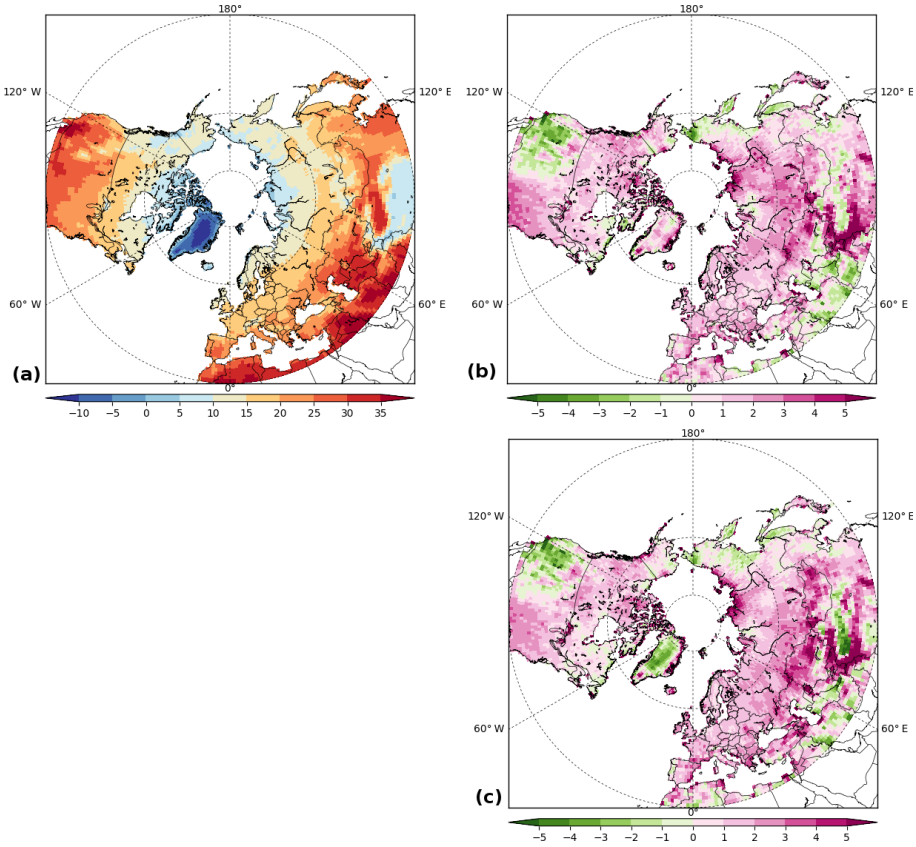

Figure 4. (a) Observed mean summer (JJA) land surface temperature (°C) and bias in the **(b)** GSWP3 and **(c)** CRUNCEP-forced simulations, averaged over the period 1996–2007.

would partly offset the warm bias in CRUNCEP land surface temperatures during summer (Fig. 4c).

6.4 Active layer thickness and permafrost area

Figure 7a, b show the simulated spatial pattern of ALT, as calculated from modeled soil temperatures using a linear interpolation between soil layers to locate the first depth that remains frozen (below 0 °C) year-round. Compared with CALM observations, in which most of the sites have ALT < 1 m, the GSWP3-forced model generally overestimates ALT by more than 1 m (also see Fig. S5, which compares modeled ALT of Yakutia, eastern Siberia with the map of Beer et al., 2013), whereas CRUNCEP-forced output shows relatively better agreement with the observations. Apart from the uncertainty induced by climate forcing, the model–data mismatch may also arise from scale differences for the organic carbon content that is used to calculate soil physical properties for each grid cell. As mentioned in Sect. 4.2, the empirical SOC map from NCSCD (Hugelius et al., 2013) is prescribed for permafrost regions in the soil thermal and hydrological modules, which is upscaled by the model to the target spatial resolution (1° by 1° in this study). These SOC values thus do not represent the site-level soil conditions, aside from the uncertainty of the NCSCD database itself. To further investigate this impact, we conducted additional simulations for the sites that provide explicit organic layer thicknesses (in total, 69 sites), forced by CRUNCEP. In these runs, we assumed pure organic soil, i.e., $f_{i,\mathrm{SOC}}$ in Eq. (9) equaling one, for the soil layers above the site-specific organic layer thickness, but kept the SOC concentration unchanged below this thickness, i.e., from NCSCD. Note that the moss layer, vegetation mat, and/or organic root zone as described in some sites were all summed to derive a total organic layer thickness. The other configurations including climate forcing and soil texture were the same as the regional simulation. The result is displayed in Fig. S6, showing significantly shallower ALTs simulated by these site runs which better match the observations (Fig. S6a), with different magnitudes of ALT reductions among the sites (Fig. S6b).

For simulated permafrost extent, two typical definitions of permafrost in LSMs, one defined as ALT less than 3 m to give "near surface" permafrost (e.g., Koven et al., 2013), the other defined if any of the soil layers stay frozen (e.g., Ekici et al., 2014; Burke et al., 2017b), produce quite different permafrost extents (Fig. 7c, d). This result highlights that the intercomparison of permafrost areas among different LSMs

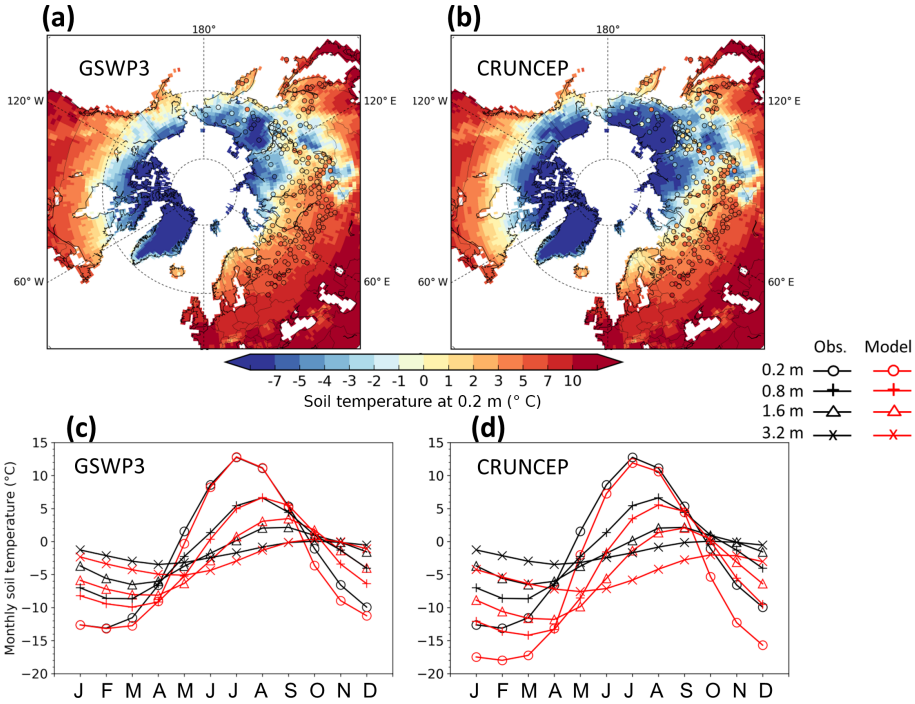

Figure 5. Mean annual soil temperature at 0.2 m depth (°C) in the **(a)** GSWP3 and **(b)** CRUNCEP-forced simulations (background maps), compared to the site observations (color filled circles), averaged over the period 1981–2000. Monthly mean seasonal soil temperatures at different depths (°C) in the **(c)** GSWP3 and **(d)** CRUNCEP-forced simulations, compared with the observation, averaged over the 51 sites in continuous permafrost region (according to the IPA map) and over the period 1981–2000. The spatial patterns of maximum monthly soil temperature are also shown in Fig. S4.

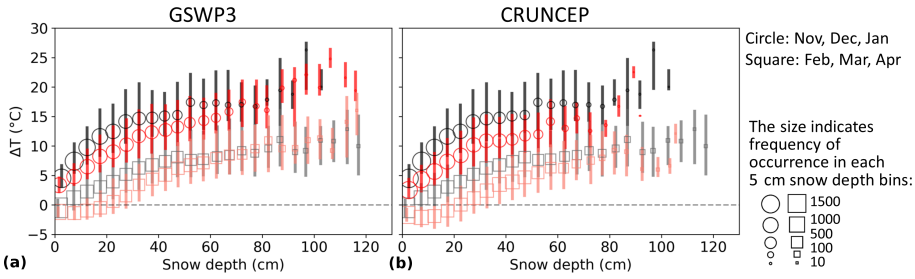

Figure 6. Relationship between ΔT (soil temperature at 20 cm depth minus air temperature) and snow depth (cm) over the period 1981–2000, for site-level observations (black), and for model results (red) (9612 site-month values in total), forced by **(a)** GSWP3 and **(b)** CRUNCEP. Circles and squares are medians of 5 cm snow depth bins, representing the early (November–January) and late (February–April) snow season, respectively. Upper and lower bars indicate the 25th and 75th percentiles of each bin. The size of circles/squares indicates the frequency of occurrence in each bin.

with differing soil vertical discretizations may include uncertainties brought by the arbitrarily chosen definition, whereas evaluation and comparison directly for soil temperatures and ALT should be more robust. A qualitative comparison against the empirical IPA (International Permafrost Association) permafrost map (Brown et al., 2002) shows better agreement for CRUNCEP compared to GSWP3-forced output, since CRUNCEP-forced simulation generally matches the distribution of continuous permafrost using the former definition, while GSWP3-forced simulation seems to underestimate permafrost extent (Fig. 7c, d). This is consistent with the deeper simulated ALT under GSWP3 climate forcing.

7 Evaluation of large-scale water storage and fluxes

Simulated water budget components are evaluated over selected northern basins (Fig. 2b), most of which are underlain by permafrost (e.g., Lena, Kolyma), with the exception of the warmer Volga. The Ob and Yenisei catchments have contrasting north–south precipitation and temperature regimes,

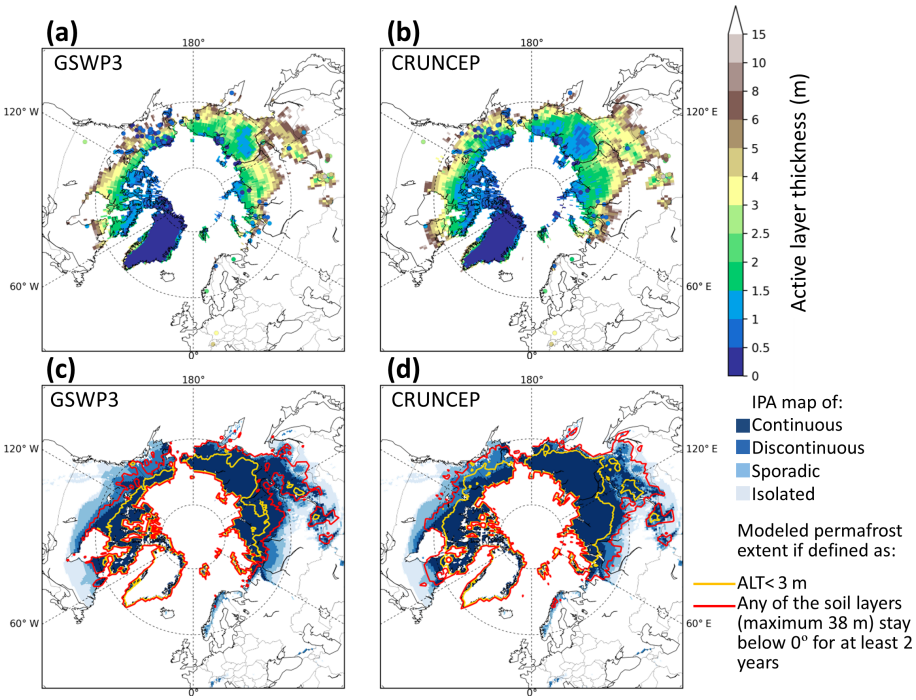

Figure 7. Active layer thickness (ALT in m) from the **(a)** GSWP3 and **(b)** CRUNCEP-forced simulations (background maps), compared to the observed ALT from the CALM network (color filled circles), averaged over the period 1990–2007. Permafrost extent from the **(c)** GSWP3 and **(d)** CRUNCEP-forced simulations according to two different definitions (yellow and red lines) on top of the IPA permafrost map (Brown et al., 2002).

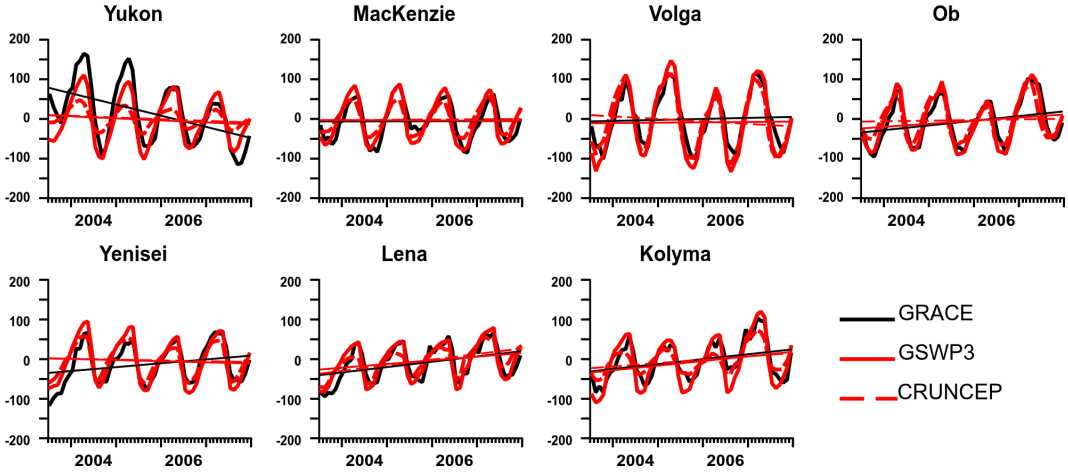

Figure 8. Interannual monthly variation and trend (line) of TWS (mm) simulated with the two forcings compared to GRACE data over the seven basins (see Fig. 2b), for the period July 2003–December 2007.

with attendant impacts on Arctic Ocean discharge and sub-basin-scale water budgets. Here, only basin-scale averages are discussed.

7.1 Total terrestrial water storage change

A realistic phase and amplitude of TWS are simulated with both forcing datasets, although peak-to-peak amplitude is slightly overestimated in the Volga, Yenisei and Kolyma basins under GSWP3 input and the seasonal amplitude underestimated in the Yukon with both forcings, and in the Mackenzie and Lena with CRUNCEP forcing (Fig. 8). The positive temporal trend of TWS in the Ob, Lena and Kolyma basins is captured well by ORCHIDEE-MICT, where it reflects upward precipitation trends (not shown). In general, the GRACE TWS is captured well by ORCHIDEE-MICT

with both forcings, at the seasonal scale and for the 5-year trends, except in the Yukon Basin, where observed TWS decreases are not reproduced in our simulations, with no precipitation decrease in the GSWP3-forced model. The Yukon TWS decline is likely due to glacier melt in the northwestern Cordillera (S. Wang et al., 2015). As glaciers are not represented in ORCHIDEE-MICT, the model does not capture these TWS trends. Note that groundwater storage changes related to the development of closed and open taliks (Muskett and Romanovsky, 2009) which contribute to existing TWS trends – increasing storage in the Lena and Yenisei, decreasing it in the Mackenzie Basin, and no change in the Ob – are not modeled either in ORCHIDEE-MICT. Despite this, the model reproduces observed trends in these basins.

7.2 Snow-related processes controlling land water storage in the cold season

The modeled seasonal cycle of the SWE and the length of the snowmelt period are in agreement with observations (Fig. 9), suggesting a good parameterization of the snowmelt and sublimation processes. However, results differ strongly according to forcing inputs. In basins with a large permafrost fraction (Yukon, Lena and Kolyma) and, to a lesser extent, in the Mackenzie, Ob and Yenisei basins, SWE is underestimated throughout the year compared to GlobSnow data when ORCHIDEE-MICT is forced by CRUNCEP, and it is significantly larger in the GSWP3-forced simulation (in the Volga Basin, the SWE is overestimated in the two simulations). This is due to the low basin-specific snowfall rate in CRUNCEP forcing compared to GSWP3 (Fig. S12), which is probably the result of the criterion used to partition rainfall and snowfall in CRUNCEP, and strongly affects the simulation of snow depth and SWE (Loth et al., 1993; Wen et al., 2013). By contrast, the GSWP3-forced model captures the early winter SWE accumulation in these basins. In spring, the SWE is systematically overestimated except over the Lena, whose seasonal cycle is well reproduced by ORCHIDEE-MICT. This corresponds to an excessive persistence of the snow cover, which may be explained by the absence of hysteresis in the snow depletion curve relating the snow cover extent and the SWE (e.g., Magand et al., 2014). In the Yenisei and Mackenzie basins, the SWE in winter is closer to observations with the GSWP3 forcing, with the exception of springtime values, which are better under CRUNCEP forcing. In basins where the permafrost area is near-zero (Ob and Volga), the SWE from CRUNCEP-forced simulation is closer to Globsnow than those from GSWP3, in which SWE is overestimated in winter and spring. This is related to the large difference in snowfall over these basins between the two forcings (Fig. S12).

7.3 Soil moisture

In the topsoil

Seasonal evolution of topsoil moisture (first 2 cm) is compared to the ESA-CCI-SM product over the seven basins (Fig. 10a). Liquid soil moisture values from the model are used for the comparison because the ESA-CCI-SM product measures only the topsoil moisture when temperature is above 0 °C. Because of scaling issues (the satellite product is rescaled to the 10 cm top layer of the NOAH model, as already noted, but is more representative of a thinner soil layer of about 2 cm), the comparison was performed on relative liquid soil moisture values after normalization with their respective SD. The observed seasonal moisture variations are captured well by ORCHIDEE-MICT with both forcings over the seven basins (Fig. 10a). The maximum values occur in summer, in contrast to lower latitudes, because of the thawing processes occurring in summer. The local minimum simulated in summer in the Volga and Ob basins is underestimated, suggesting a too slow infiltration front of the water in the topsoil layers of the model. Thus, less water in the root zone is available for transpiration, which is found to be underestimated when compared to GLEAM (see Fig. 11b). Compared to observations, a more rapid increase (decrease) in the modeled topsoil moisture in spring during snowmelt (in fall) is found in the Yukon and Mackenzie basins, related to a more rapid thawing (freezing) of the topsoil.

In the root zone

The soil water deficit is of primary importance during spring and summer at the high latitudes because of its potential impacts on the vegetation transpiration, leading to a surface temperature increase and a reduction in the productivity. However, a soil water comparison between GLEAM and ORCHIDEE-MICT is difficult because of differences in soil depth, which in GLEAM varies with vegetation cover, but is fixed at 2 m in ORCHIDEE-MICT. Moreover, the fraction of soil tiles of short vegetation and forests used in the two products is not the same. We therefore normalize the relative root soil moisture (Fig. 10b) by its SD to compare the dynamic of the soil moisture rather than the total amount of water in the soil. The intensity of water uptake by the roots of the vegetation in summer is generally well simulated by the model in both simulations. In basins underlain by permafrost, except in the Lena Basin, water uptake is delayed by 1 month for both forcing sets, while the rate of decrease in root soil moisture is underestimated for GSWP3-forced output only. The similarity in output in this respect, despite very different SWE, highlights the low impact of the latter on the root soil moisture, and further underscores how the snowmelt differential is lost through runoff rather than being available for vegetation.

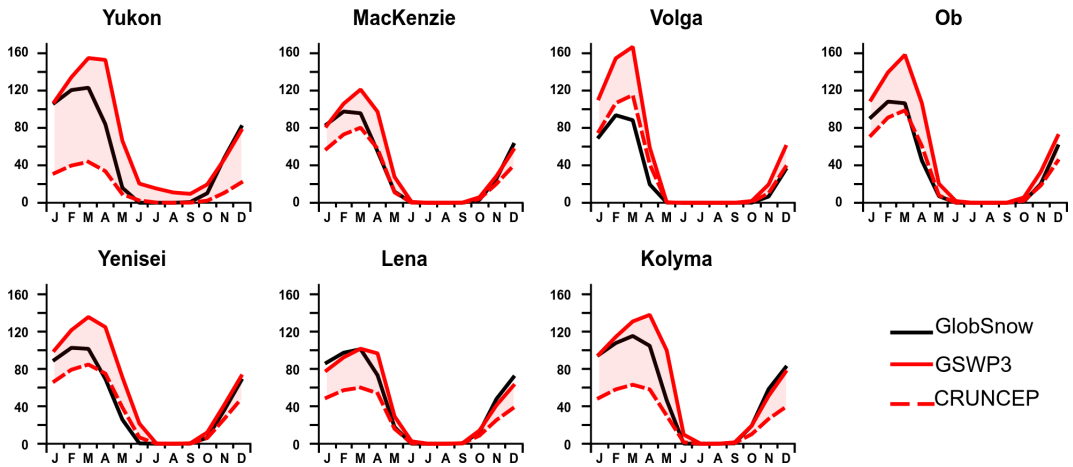

Figure 9. Monthly mean seasonal SWE (mm) simulated with the two forcings compared to GlobSnow over the seven basins (see Fig. 2b), averaged over the period 1981–2007.

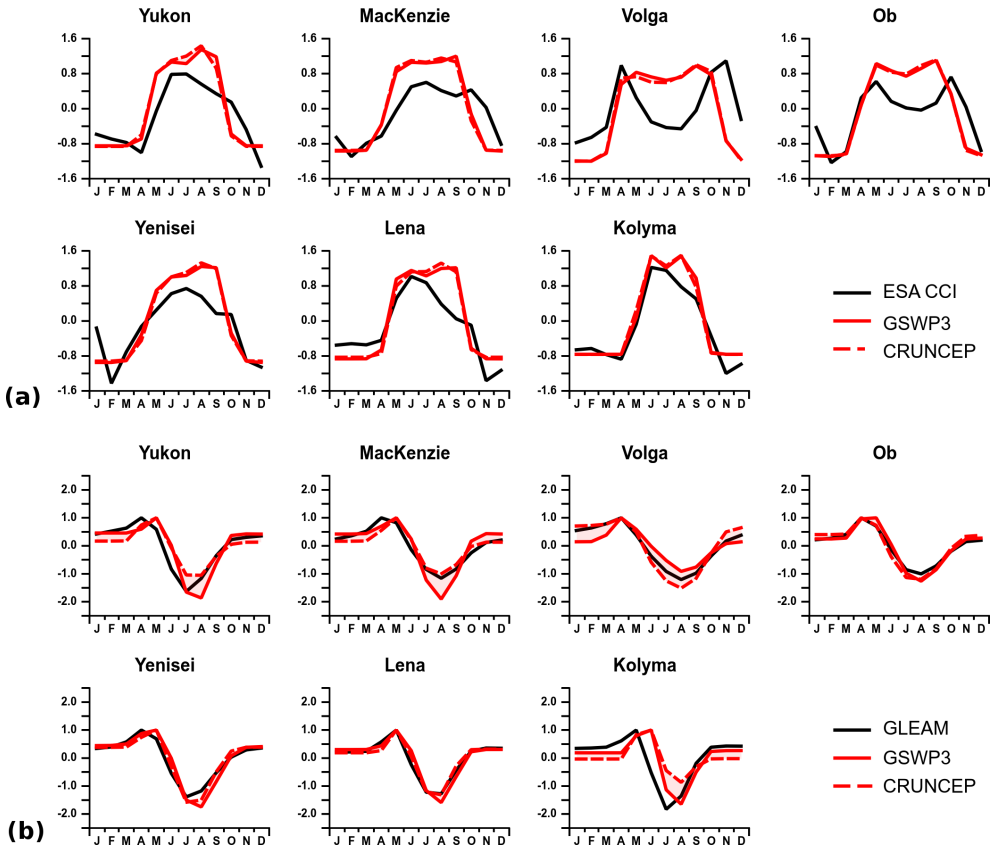

Figure 10. Monthly mean seasonal relative **(a)** topsoil (–) and **(b)** root soil moisture (–), both normalized by their multi-year SD, simulated with the GSWP3 and CRUNCEP forcings over the seven basins (see Fig. 2b), averaged over the period 1981–2007. The results are compared with **(a)** satellite-derived observations from ESA CCI and **(b)** the GLEAM data-driven model assimilated against satellite data.

7.4 Evapotranspiration and component fluxes

The amplitude of the ET seasonal cycle is generally well captured by the model in most basins, when compared to the GLEAM product, despite a systematic underestimation by ORCHIDEE-MICT, whatever the input forcing (Fig. 11a). The disparity between modeled peak ET and GLEAM data is reduced under GSWP3 forcing in the Yukon, and under CRUNCEP forcing in the Yenisei and Lena. ET increase is

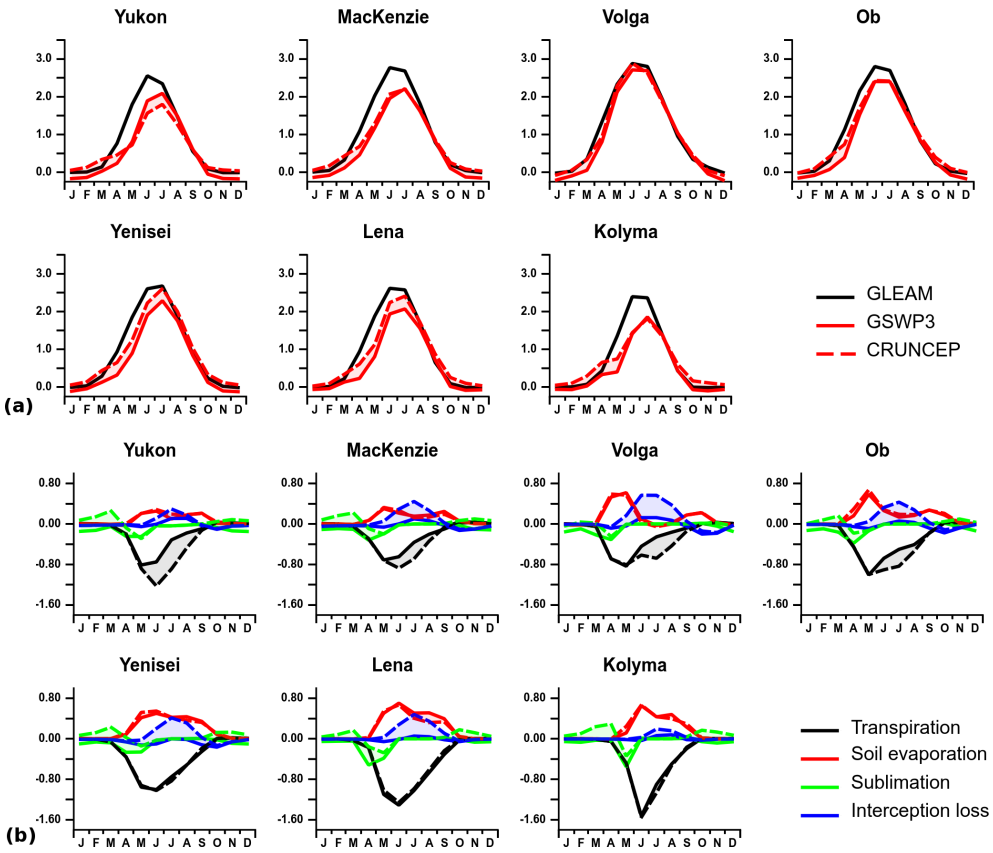

Figure 11. **(a)** Monthly mean seasonal evapotranspiration (mm d^{-1}) simulated with the two forcings compared to the GLEAM data-driven model over the seven basins (see Fig. 2b), averaged over the period 1981–2007. **(b)** Seasonal bias of ET components (mm d^{-1}) averaged over the same period, with the GSWP3 (solid line) and CRUNCEP (dashed line) forcings.

underestimated in spring and early summer for both forcings, except in the Volga Basin. This is consistent with modeled LAI increasing too late in spring (see Fig. 13), which could be due, at least partially, to an excessive persistence of the snow cover in spring. In fall, the timing of the decrease in ET is reproduced by both forcings. Model biases with respect to GLEAM data in the sublimation, soil evaporation and transpiration components of ET are shown in Fig. 11b. In all basins, sublimation bias in simulations forced by GSWP3 is ~ 0 in winter, in agreement with GLEAM. By contrast, CRUNCEP-forced simulations slightly overestimate sublimation in early spring across basins with the exception of the Volga. These results are consistent with SWE underestimation (except in the Volga) (Fig. 9) and higher downward shortwave radiation (Fig. S14) that results when CRUNCEP forcing is used. The general underestimation of summer ET by ORCHIDEE-MICT in the Yukon, Mackenzie and Kolyma basins is explained mainly by a too low transpiration despite bare soil evaporation being slightly overestimated (Fig. 11b). When forced by CRUNCEP data, ORCHIDEE-MICT overestimates interception loss in all basins but the Kolyma and Yukon, which is consistent with CRUNCEP LAI overestimation (see Fig. 13).

7.5 River discharge

By comparing the two simulations, it is clear that the meteorological forcing exerts a significant influence on the simulated river discharge (Fig. 12): GSWP3 leads to systematically higher river discharge than CRUNCEP, which is perfectly consistent with the SWE biases (Fig. 9). In a majority of basins, GSWP3-forced simulations better capture the seasonal cycle of observed discharge than CRUNCEP-forced ones, especially in the Yukon and eastern Siberian basins, where the discharge is strongly underestimated under CRUNCEP forcing (between 60 % in the Yenisei and 83 % in the Yukon).

A first feature of the nival regime characterizing the studied high-latitude basins is the occurrence of low flows in winter, when water is frozen in the snowpack, soils, and river ice. This is well simulated by ORCHIDEE-MICT, despite a small underestimation in the Yukon, Mackenzie and Yenisei. Naturalized river discharge is available in the latter, and lower in winter than GRDC values, which reflects the effect of reservoir operations. The winter discharge simulated by ORCHIDEE-MICT in the Yenisei is closer to the naturalized estimates, as the model does not account for artificial reser-

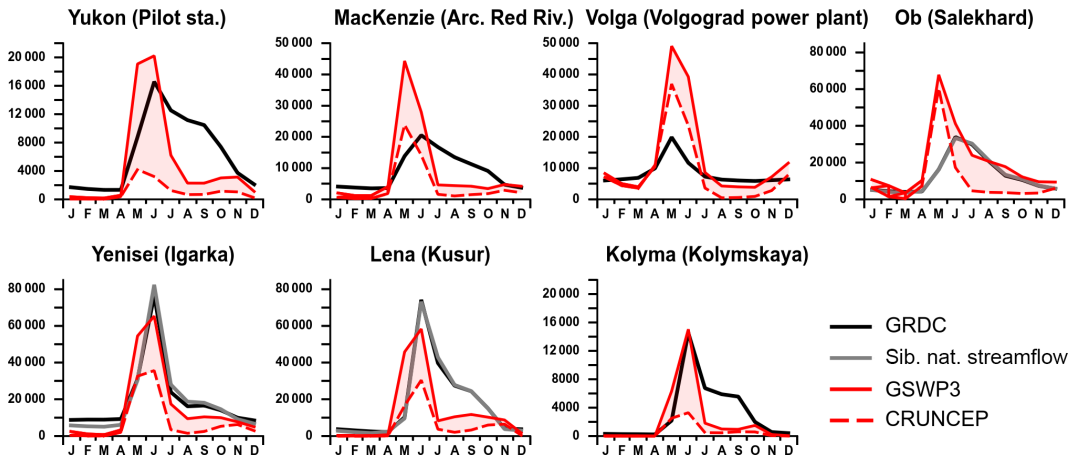

Figure 12. Monthly mean seasonal river discharge ($m^3 s^{-1}$) simulated with the two forcings compared to the observed non-naturalized (GRDC) and Siberian naturalized river discharge dataset at the gauge stations of the seven basins (see Fig. 2b), averaged over the period 1981–2007.

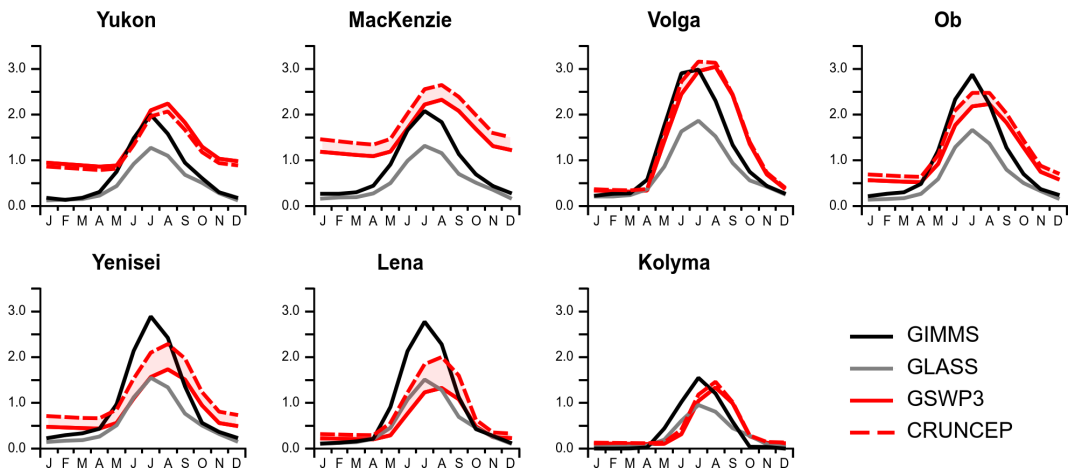

Figure 13. Monthly mean seasonal LAI (–) simulated with the two forcings compared to GIMMS and GLASS products over the seven basins (see Fig. 2b), averaged over the period 1981–2007.

voirs. No natural lakes are simulated by ORCHIDEE-MICT, which may contribute to the winter discharge underestimation, especially for the Mackenzie, which includes massive lakes (Great Slave, Great Bear, and Athabasca).

The nival regime of the studied basins is also characterized by peak flow in late spring, which is broadly captured by the ORCHIDEE-MICT simulations, even if the magnitude of peak flow is strongly biased in some cases, with a strong link to the forcing used and the SWE biases. As an example, the Volga is the only river where both peak flow and SWE are overestimated with both forcings, and closer to river discharge observations under the CRUNCEP forcing. In this human-altered basin, the absence of the simulation of water withdrawals for irrigation in the model can explain the peak flow overestimation.

An almost systematic weakness of the simulated hydrographs is the underestimation of river discharge during summer and fall, which is very strong with both forcings in the Yukon, Mackenzie, Lena and Kolyma, and to a lesser extent in the Yenisei. This makes discharge closer to observations during the second half of the year under GSWP3 than under CRUNCEP, particularly in the Ob. This summer–fall underestimation propagates to underestimated annual mean discharge in a majority of basins (reaching −25 and −30 % under GSWP3 in the Lena and Kolyma rivers) despite the overestimation of peak flows. Eventually, the discharge underestimation found in summer and fall, and on annual means in many basins, is not coherent with the low simulated ET compared to GLEAM data. However, according to S. Wang et al. (2015), biases in precipitation and ET datasets, which are used to evaluate the models, are source of errors for the water imbalances found in the northern high-latitude basins.

These river discharge results highlight deficiencies in the model representation of water infiltration in frozen

soils, which appear to be too drastic in their prevention of snowmelt infiltration under conditions of frozen topsoils. Alternative parameterizations of these dynamics are underway. For example, infiltration of meltwater into frozen soil could be permitted when accounting for sub-grid-scale variability of topsoil freezing and drying which would enhance infiltration (Gray et al., 2001). Other perspectives are the improvement of the floodplain parameterization in ORCHIDEE-MICT (Lauerwald et al., 2017) and the inclusion of natural lakes and artificial reservoirs.

8 Evaluation of the leaf area index, gross and net CO_2 fluxes

8.1 Leaf area index

According to the two evaluation products, the seasonal cycle of LAI (Fig. 13) is similar across the basins, with values near zero during winter, and a maximum in summer. There is a consistent phasing of seasonal LAI between the two evaluation datasets; however, maximum LAI in GIMMS is systematically higher than in GLASS. In all the basins, the LAI simulated by ORCHIDEE-MICT has a phase delay of up to 1 month compared to both products. This is due to a delay in the start of the growing season, which may be related to excessive persistence of the snow cover (Fig. 9). The phenological models in ORCHIDEE (detailed in MacBean et al., 2015, Appendix A) do not explicitly take into account this influence, unlike what is done in Van Wijk et al. (2003), who model the link of the start of the tussock tundra growing season to the soil thaw at 10 cm depth. However, there is a first indirect link between the snow cover and the vegetation phenology through air temperature, which influences both the start of the growing season, determined in ORCHIDEE using growing degree days (GDD)-based phenological models for deciduous species, and the start of the snowmelt season. There is a second indirect link through snowmelt. While there is still a large amount of snow, the soil surface temperature is kept at zero degree Celsius or below, and the soil cannot thaw. Only when snowmelt occurs and when the snow fraction is small enough will the soil start thawing, thus increasing soil liquid water content. This impacts the start of the growing season for grasses and crops, which use both a GDD and a soil moisture thresholds, and also reduces water stress, thus favoring photosynthesis for all PFTs. Note here that ORCHIDEE-MICT is prone to overestimating the timing of senescence (MacBean et al., 2015). This is true in particular for conifers, for which the model lacks an explicit senescence inception model. Except in the Yukon and Mackenzie basins, the maximum LAI simulated by ORCHIDEE-MICT lies between the two satellite product estimates. Winter LAI of ~ 1.0 are overestimated in the Yukon, Mackenzie, Ob and Yenisei basins; however, observations show values around zero. Given that these basins are covered by a larger fraction of evergreen forests compared to the others, these simulated values look reasonable. The mismatch with the observations could be explained here by data errors, the assessment of solar reflectance from space in winter at the high latitudes being less reliable.

8.2 Gross (GPP) and net (NPP) primary productivity

8.2.1 Spatial distribution and seasonal cycle of GPP

GPP at the high latitudes is co-limited by cold temperatures, constraining the duration of the growing season, and by summer water stress (Schulze et al., 1999) in northern Canada and Siberian boreal forests, for which the water balance is usually negative at this time. The simulated spatial pattern of GPP in Eurasia and North America is close to the MTE-GPP dataset (Fig. 14). Values lower than MTE-GPP were simulated in eastern Siberia under the GSWP3 forcing, mainly due to water stress (see also the underestimated biomass for eastern Siberia in Fig. 20). The seasonal GPP cycle in Fig. 14b is generally accurate with respect to observations at the scale of large boreal regions; however, peak GPP is strongly overestimated for boreal North America (BONA).

Interestingly, comparing GPP forced by the two climate datasets shows higher values by CRUNCEP than by GSWP3 (Fig. 14), despite a generally lower precipitation in CRUNCEP (Fig. S13). This could be explained by the higher specific air humidity during summer in CRUNCEP than in GSWP3 (Fig. S16). A low air humidity increases the atmospheric vapor pressure deficit (VPD) and the leaf-to-air vapor pressure difference; plants then partially close the stomata to constrain a potentially fast transpiration (Oren et al., 1999; McAdam and Brodribb, 2015), which leads to a reduced photosynthetic rate. The photosynthesis module in ORCHIDEE largely follows Yin and Struik (2009), in which stomata conductance decreases with an increasing VPD, and thus is able to simulate a lower GPP under dry air conditions. A recent study (Novick et al., 2016) showed that, between the two factors that impact plant water stress, i.e., soil moisture supply and atmospheric demand for water (reflected by VPD), the latter limits evapotranspiration to a greater extent than the former in relatively wet forested ecosystems. In spite of its importance, the effect of VPD on vegetation productivity has been far less studied than soil water availability (Konings et al., 2017), warranting further investigations in both observations and land surface models.

8.2.2 Spatial distribution of NPP and site-level comparison

The distribution of NPP for both ORCHIDEE-MICT simulations is compared to forest site data from Campioli et al. (2015) (Fig. 15), in which NPP measurements are collocated with GPP (118 sites in total north of 30° N). Despite no sampling from western Russia

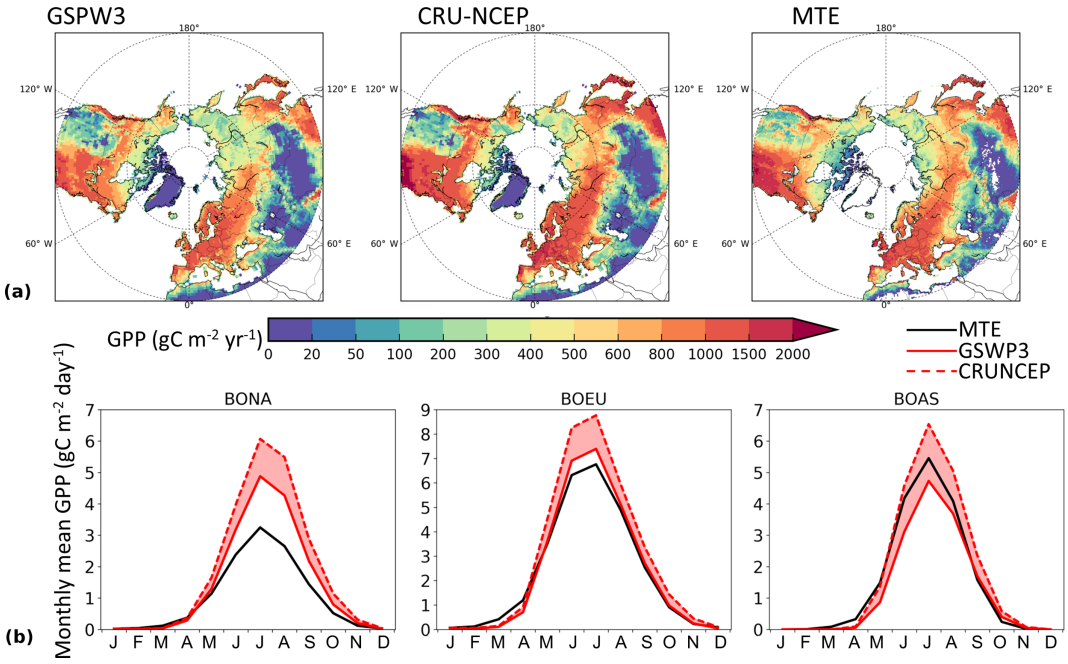

Figure 14. **(a)** Simulated annual GPP ($g\,C\,m^{-2}\,day^{-1}$) from the two climate forcings, compared to the data-driven MTE-GPP, averaged over the period 2000–2007. **(b)** Monthly mean seasonal GPP ($g\,C\,m^{-2}\,day^{-1}$) simulated with the two forcings compared to MTE-GPP over the three high-latitude sub-regions (shown in Fig. 2a), averaged over the same period.

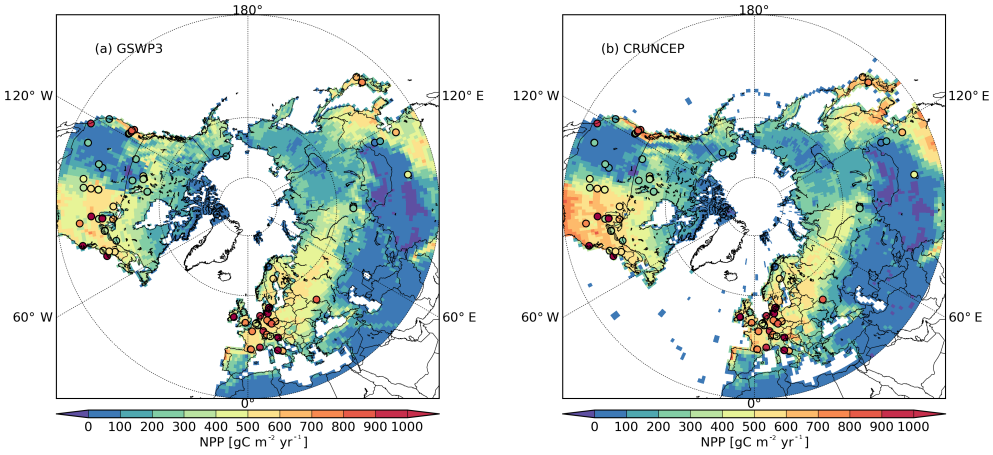

Figure 15. Mean annual NPP ($g\,C\,m^{-2}\,yr^{-1}$) simulated with **(a)** GSWP3 and **(b)** CRUNCEP forcings (background maps) compared to the site observations (color filled circles), averaged over the period 2000–2007.

and Siberia, the model is able to reasonably capture NPP gradients in BONA and BOEU. In temperate forests of western Europe and the eastern US, modeled NPP is too low (see also Fig. 16b for warm sites), possibly due to high water stress in ORCHIDEE-MICT (see below).

Considering only the 52 sites that were selected (as described in Appendix C3), we computed the distributions of GPP and NPP by 5 °C mean annual temperature bins for the sites, the MTE-GPP and MODIS-NPP products, and for the ORCHIDEE-MICT simulations. We plot the 95th percentiles of these distributions in Fig. 16, which arguably defines an upper envelope for temperature-limited GPP and NPP (see Fig. 3 of Luyssaert et al., 2007), and allows us to evaluate the spatial sensitivity of GPP and NPP to mean annual temperature. The behavior of all products is similar to the sensitivities derived from site observations, with a strong positive relationship between GPP, NPP and mean annual temperature over the range −10 to 10 °C. ORCHIDEE-MICT then captures the decrease in GPP (NPP) at warmer sites, but underestimates the values above 5 °C. Global gridded data products generated independently from the Campioli et al. (2015) dataset exhibit sensitivities comparable to those derived from

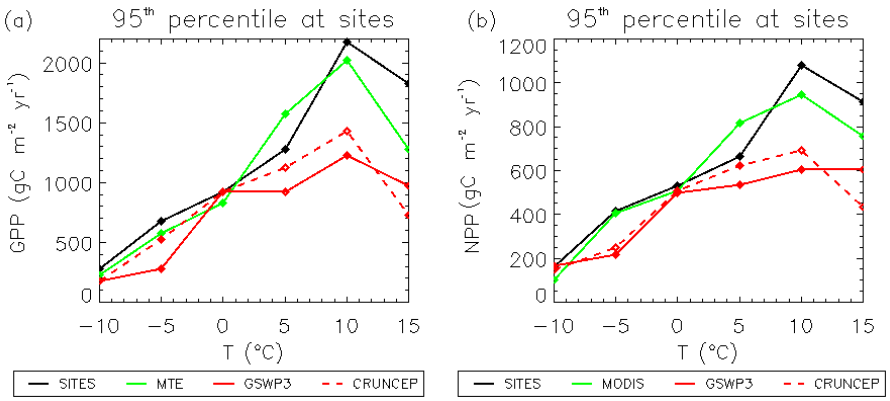

Figure 16. 95th percentiles of mean annual **(a)** GPP ($g\,C\,m^{-2}\,yr^{-1}$) and **(b)** NPP ($g\,C\,m^{-2}\,yr^{-1}$) distributions per temperature bins of 5 °C for in situ measurements, the gridded MTE-GPP (MODIS-NPP) product sampled at the sites' locations and the two simulation results, averaged over the period 2000–2007.

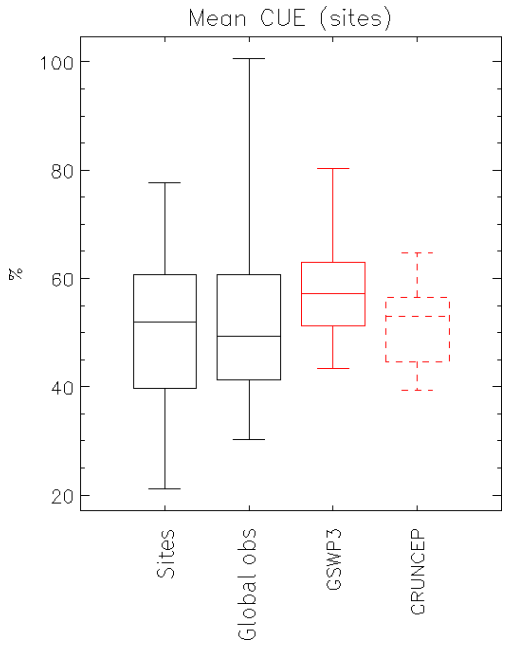

Figure 17. Mean annual CUE (%) over the 52 Campioli sites, averaged over the period 2000–2007. The first black boxplot is computed using the local estimations of the Campioli et al. (2015) database and the second one (global observations) using MODIS-NPP and MTE-GPP. The red boxplots use the values of the two simulations. For each boxplot the median value is the short horizontal bar within the rectangle, whose bottom and top sides illustrate the 25th and 75th percentiles of the distribution, while the vertical segments link those sides to the points representing, respectively, the minimum and maximum values.

local sites, whereas modeled GPP and NPP saturate for temperatures above 10 °C, indicating water stress dominant controls.

The local measurements and the global observations products give similar median CUE values (51 and 49 %, respectively) and first and third quartiles, whereas the model gives a narrower distribution range, with higher median values (57 % for GSWP3 and 53 % for CRUNCEP) (Fig. 17).

8.3 Spatial distribution of burned area and fire emissions

The spatial distribution of burned area is largely reproduced by ORCHIDEE-MICT, with a higher fraction of burned area in central Eurasia, and a decrease in burned area toward higher latitudes (Fig. 18). For the GSWP3 simulation, modeled total burned area over the period 1997–2007 (in the unit of $Mha\,yr^{-1}$) is smaller than GFED4s for BONA (1.7 vs. 2.2 in GFED4s), and higher for BOEU (8.1 vs. 5.0) and BOAS (16.1 vs. 10.4). Modeled spatial distribution of natural fire emissions has greater discrepancies with respect to evaluation data than burned area, bearing in mind that GFED4s data are based on a biosphere model (CASA), not observations. Higher emissions in eastern Eurasia are reproduced by ORCHIDEE-MICT. However, modeled emissions are overestimated for central Eurasia and underestimated in boreal America, with respect to GFED4s. As a result, regional carbon emissions (in the unit of $Tg\,C\,yr^{-1}$) in ORCHIDEE-MICT are lower than in GFED4s for BONA (20 vs. 48), much higher for BOEU (45 vs. 6), and in good agreement for BOAS (104 vs. 111). One possible reason for the discrepancy in BOEU is the lack of forest management and fire suppression measures in ORCHIDEE-MICT, leading to higher simulated burned area and carbon emissions than in GFED4s. Changing the climate forcing from GSWP3 to CRUNCEP yields a smaller burned area (Fig. 18b and c). Because the reduction of burned area mainly occurs in grassland, the impact on carbon emission is small.

Carbon emissions peak in summer for both GFED4s and ORCHIDEE-MICT for BONA and BOEU (Fig. S7d, e).

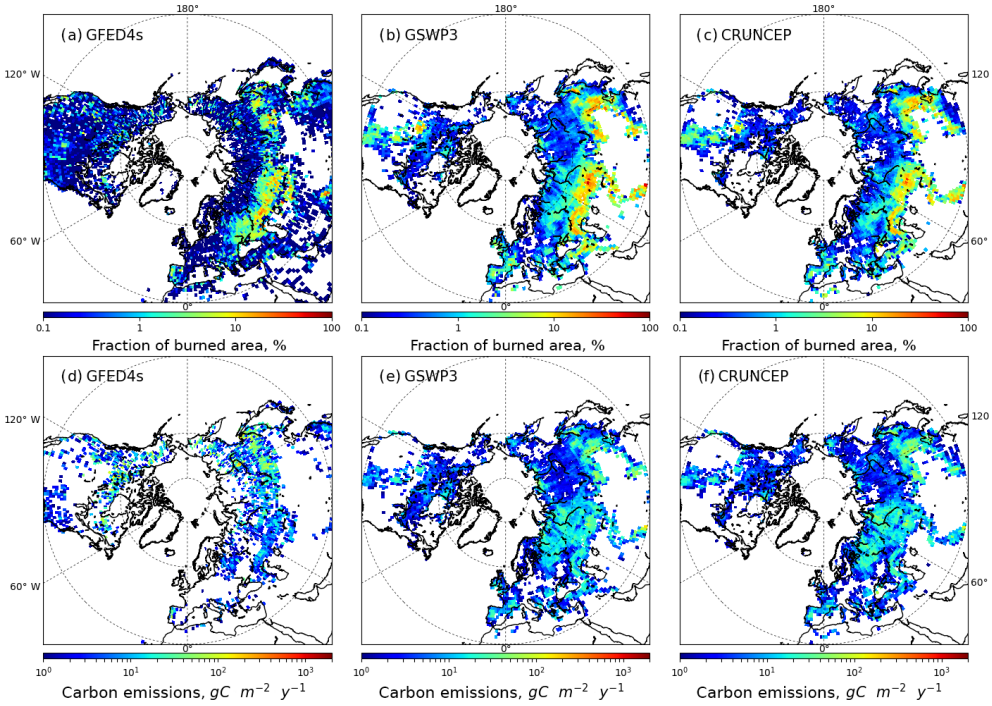

Figure 18. (a–c) Mean annual fractional burned area (%) from **(a)** satellite observation in GFED4s and **(b)** GSWP3 and **(c)** CRUNCEP-forced simulations. **(d–f)** Mean annual carbon emissions from natural fires ($g\,C\,m^{-2}\,yr^{-1}$) from **(d)** satellite observation in GFED4s and **(e)** GSWP3 and **(f)** CRUNCEP-forced simulations, averaged over the period 1997–2007. The burned area fraction simulated from ORCHIDEE-MICT is corrected for the omission of cropland fires in the simulation.

However, for BONA the fire season starts 1 month later in ORCHIDEE-MICT (Fig. S7a). For BOAS and BOEU, there are stronger discrepancies in seasonal carbon emission (Fig. S7e, f). In particular, ORCHIDEE-MICT fails to account for the April peak in carbon emissions. A possible explanation for the missing April emissions in ORCHIDEE-MICT may be the late timing of snowmelt (Fig. 9) and the delayed spring increase in LAI (Fig. 13). This would cause an unavailability of fuel in springtime. Changing the climate forcing from GSWP3 to CRUNCEP has only a very small effect on burned area and carbon emission seasonality.

8.4 Seasonal cycle of NEE

Monthly NEE from inversions, originally provided at the spatial resolution of each transport model, was aggregated at the scale of the three high-latitude sub-regions (Fig. 2a). Spatially averaged NEE is expected to be more consistent between different inversions at a coarser spatial scale, given the sparseness of atmospheric CO_2 stations and differences in transport models. Nevertheless, the seasonal cycle of NEE is generally consistently estimated by the two inversions in each sub-region, although Jena CarboScope estimates generally higher seasonal NEE amplitude, and in BOEU NEE from CAMS peaks 1 month earlier than Jena CarboScope (Fig. 19). Simulated seasonal NEE (defined as GPP minus autotrophic and heterotrophic respiration, fire emissions and emissions from LUC) magnitude and evolution is very similar in both simulations and, in general, ORCHIDEE-MICT was able to reproduce the timing and magnitude of the transition between winter release and spring NEE uptake, despite a later onset of spring uptake for all three boreal sub-regions, and a smaller peak summer NEE for BOAS.

Since the timing of NEE uptake in spring and release in fall is well constrained in the inversions from the observed periodical drawdown and buildup of CO_2 at atmospheric stations, the modeled delayed onset of spring uptake is consistent with the $\sim$ 1-month lag between ORCHIDEE-simulated and satellite-observed LAI in Fig. 13 (and ET in Fig. 11a) in the basins of the three sub-regions. Even though GPP is overestimated in BONA during spring and summer (Fig. 14b), the resulting NEE gives a slightly weaker uptake.

Modeled fall and winter emissions (positive NEE) from soil respiration are well reproduced in the BOEU sub-region, even though the release is overestimated in fall and underestimated in winter. The underestimation of NEE from October to March in BONA and BOAS suggests that cold season respiration in soils is underestimated in the model. This may be because of (i) decomposition in the model being cut off at $T = -1\,°C$, whereas observations suggest it can be sustained well below the freezing point in liquid films of soil pores (Schaefer and Jafarov, 2016); (ii) insufficient snow insulation of soils (see Fig. 6); and (iii) the lack of the carbon cycle of

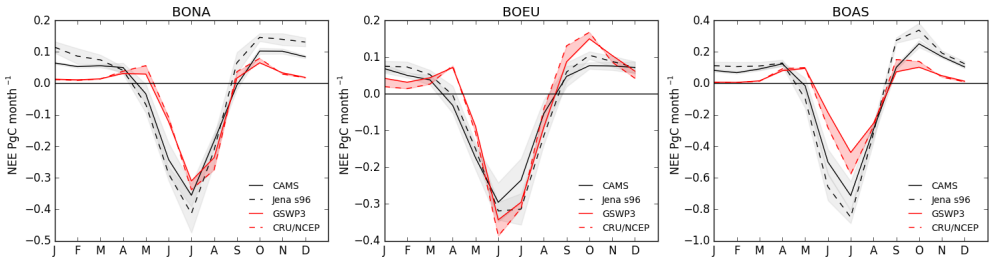

Figure 19. Monthly mean seasonal net land–atmosphere CO_2 fluxes (NEE in Pg C month^{-1}) from the GSWP3 and CRUNCEP-forced simulations compared to atmospheric inversions, over the three high-latitude sub-regions (shown in Fig. 2a), averaged over the period 2000–2007. The grey shaded areas correspond to the SD of the monthly values for each inversion. Note that a negative sign in NEE corresponds to CO_2 uptake from the atmosphere, and a positive sign to release into the atmosphere.

mosses and lichens which could have respiration under winter low temperatures (Atanasiu, 1971). This suggests that we should either allow decomposition below the freezing point, perhaps to account for heat produced in the soil by microbial decomposition (Zimov et al., 1993; Hollesen et al., 2015), improve the snow insulation, prescribe an organic layer of insulating topsoil (e.g., mosses, O-horizons observed in boreal forests; see O'Donnell et al., 2011) into the thermal module, or explicitly represent the moss/lichen plants, including their carbon cycle and physical effects (Porada et al., 2016; Druel et al., 2017).

NEE discrepancies may be related to the different seasonal contributions of evergreen and deciduous trees to GPP and LAI (Fig. S9), as well as to the relative sensitivity of heterotrophic respiration, autotrophic respiration and disturbances to the warming (cooling) at the beginning of the growing season (winter).

9 Evaluation of carbon stocks

9.1 Biomass

Consistent with the LAI and GPP results, the simulation forced by CRUNCEP shows higher forest biomass carbon densities than the GSWP3 simulation (Fig. 20). The two simulations, however, exhibit similar patterns, which reproduce the general spatial pattern of observed biomass, being higher in the western and eastern regions of North America, with a declining gradient across Eurasia from the west to the east. However, in general, the model tends to overestimate carbon density in regions of observed high carbon density (e.g., northwestern Europe and European Russia, eastern North America, the Korean Peninsula and Japan). The model also misplaced the region of the highest biomass density in northwestern Europe and European Russia rather than central Europe as shown by the observation data. Likewise, the model estimates extremely large biomass in eastern North America, especially by CRUNCEP forcing, which almost doubles the observed amount. For the rest of the study region, simulated carbon density is slightly lower than observations, by around 5–25 Mg C ha^{-1}. The two observation datasets show considerable similarities.

Both model output and observation data are subject to the spatial uncertainties introduced by the use of satellite-derived land cover maps. We thus used the forest cover map as prescribed in the model for both datasets, and calculated latitudinal averages to compare with model results (Fig. S8). GSWP3-forced model output agrees well with observations averaged over the whole study region, while CRUNCEP-forced output overestimates biomass at all latitudes (Fig. S8a). For the sub-regions, the overestimation of biomass in BONA is consistent with that of GPP (Fig. 14), while biomass is more overestimated in BOEU compared with GPP, probably because of the lack of forest management and forest age structure for Europe. Comparing the two model results, CRUNCEP-forced biomass is much higher than GSWP3-forced biomass, which cannot solely be explained by the higher GPP by CRUNCEP (Fig. 14), indicating a bias in the allocation scheme in ORCHIDEE. As detailed in Krinner et al. (2005), the photosynthates are partitioned into leaves, roots, sapwood, and carbohydrate reserve, dependent on soil moisture, etc. If the LAI is above a PFT-specific maximum value, carbon will not be allocated to leaves but to the sapwood, which slowly converts to heartwood. Therefore, a higher LAI forced by CRUNCEP leads to more carbon allocation to the wood for some areas, the turnover time of which is much longer than leaves. A new allocation scheme based on the pipe model was implemented in another branch of ORCHIDEE (Naudts et al., 2015), which provides a physiologically meaningful relationship between foliage, roots, and wood. This would be incorporated into ORCHIDEE-MICT in the future developments. Simulated total forest biomass for the whole domain is 95 Pg C under GSWP3 forcing (165 Pg C under CRUNCEP), close to estimates from forest inventory data in Pan et al. (2011) of 92.1 PgC. Somewhat lower estimates are derived by Avitabile et al. (2016) and Thurner et al. (2014), of 73 and 84 PgC, respectively.

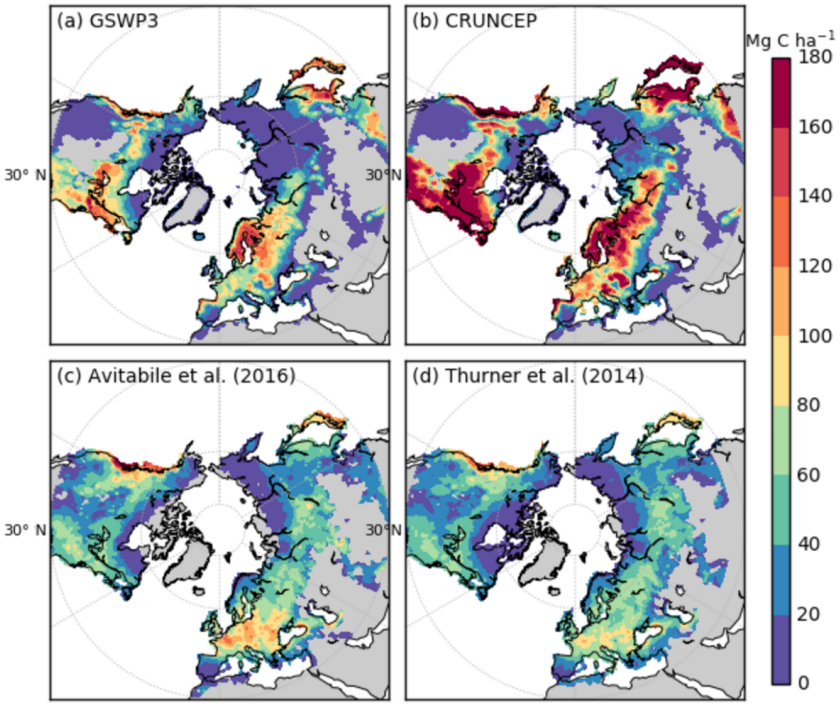

Figure 20. Total forest biomass carbon density (Mg C ha^{-1}) from the **(a)** GSWP3 and **(b)** CRUNCEP-forced simulations compared with satellite-derived observation products from **(c)** Avitabile et al. (2016) and **(d)** Thurner et al. (2014), averaged over the period 2000–2007.

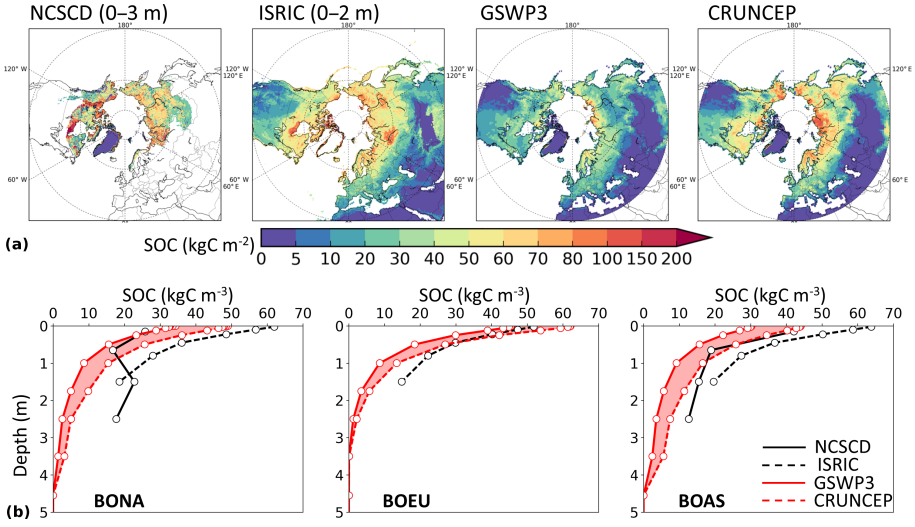

Figure 21. Soil organic carbon from the GSWP3 and CRUNCEP-forced simulations compared with the two inventory datasets NCSCD (Hugelius et al., 2013) and SoilGrids, averaged over the period 2000–2007. **(a)** Spatial distribution (kg C m^{-2}). **(b)** Vertical profiles (kg C m^{-3}) averaged over the three high-latitude sub-regions (shown in Fig. 2a). Since NCSCD does not encompass the whole domain, only grid cells with available data in NCSCD are averaged for BONA and BOAS so that the four vertical profiles are comparable, while for BOEU, NCSCD is not shown, as it has few data in this sub-region.

9.2 Soil carbon

SOC stocks simulated by the model fit to some extent the one of the observed inventory data, including that of NCSCD's permafrost region near-surface SOC density (Fig. 21), but generate lower values than those from SoilGrids in BONA and BOAS. ORCHIDEE-MICT tends to underestimate SOC density in deep soils below ~ 1 m. This underestimation is maybe because the model does not include the sedimentation of soils that characterized peat formation during the

Holocene or simulation of loess carbon or yedoma deposits during the last glacial period (Zimov et al., 2009; Zhu et al., 2016). Further, spin-up was performed with the coarse approximating assumption that Holocene climate is equal to the recent climate. Nevertheless, it is important to note that SoilGrids and NCSCD products also have important dissimilarities in overlapping regions, suggesting that high systematic uncertainties exist in boreal and Arctic SOC inventories. We also observe that modeled SOC stocks are rather dependent on climate forcing inputs, particularly for BONA and BOAS (Fig. 21). Higher stocks are produced under CRUNCEP forcing, mainly due to the higher primary productivity and therefore higher inputs to SOC associated with these forcing data.

10 Discussion

The model performances against datasets being documented in previous sections, we focus here on key mechanisms expected from a "high-latitude" model: (1) the conversion of winter snow and ice storage into a peak river discharge in spring, (2) the ability to capture the rectification of the seasonal amplitude of air temperature through the insulating snowpack and its attenuation at depth in the soil profile, and (3) the ability to reproduce the large-scale gradients of carbon input to ecosystems from GPP and NPP and its further partitioning into live biomass and SOC pools driving soil heterotrophic respiration.

10.1 Conversion of winter water storage to spring and summer river discharge

We have shown that the model simulated very different river discharge values according to the atmospheric forcing used. The spatial distribution estimate of winter snowfall at high latitudes in climate datasets is very difficult. The first reason is the low density of meteorological stations, in particular in the CRU data (Burke et al., 2013), which leads to lower total precipitation in winter and spring (November to April) in CRUNCEP compared to GSWP3 forcing (Fig. S13). Another well-known reason is the difficulty in catching snowfall in a gauge, because of its lower density; the wind prevents the snowfall from being vertical, leading to systematic undercatch (Yang et al., 2005). Then, the way the total precipitation is partitioned into rainfall and snowfall in the atmospheric forcing can also change the SWE in winter and spring. The threshold of 0 °C in 2 m temperature, used to partition the precipitation in the CRUNCEP forcing, can lead to very different results compared to the physical partitioning performed within the dynamical downscaling for the GSWP3 forcing. In the Yukon and Kolyma basins, the proportion of snowfall to total precipitation in winter and spring being 100 % in both forcings, the precipitation partitioning has no influence in these basins. By contrast, the proportion of snowfall to total precipitation in winter and spring largely differs between the two forcings in the other basins, in particular in the Volga (77 % in GSWP3 and 53 % in CRUNCEP), Ob (84 and 72 %), Yenisei (87 and 80 %) and Lena (96 and 89 %) basins.

We can assume that most of the forcing-related bias in SWE is converted into a river discharge bias in spring. Regressing the spring (April to June) river discharge bias for each forcing against the bias of SWE during the pre-melt season (February to March), over the same period of spring discharge and pre-melt season as Rawlins et al. (2007), shows that across the seven basins, 69 % of the spatial variance of the bias of the spring flow is explained by the SWE bias during the pre-melt season (Fig. 22). With GSWP3 forcing, the positive ratio of pre-melt SWE bias to spring flow bias ranges between 7 and 97 % in the different basins (Table S5). With the CRUNCEP forcing, this range is from 9 to 34 %. In some basins such as the Ob or the Mackenzie with CRUNCEP or the Lena with GSWP3, the errors in spring discharge cannot be evidently related to the SWE bias (negative ratio). This can be explained by the periods chosen for spring and pre-melt which are not necessarily the same for all basins, in particular in the Ob, Mackenzie and Lena, the rivers for which the advance of simulated peak flow is the largest. The higher sublimation in the end of winter with CRUNCEP compared to GSWP3 (Fig. 11b), probably related to higher downward shortwave radiation and lower specific air humidity in CRUNCEP (Figs. S14 and S16, respectively), also contributes to the reduced spring discharge between the two simulations (Fig. 12). Over the Lena Basin, higher soil evaporation together with higher interception loss (Fig. 11b), which is coherent with higher LAI (Fig. 13), lead to higher ET in summer with CRUNCEP (Fig. 11a), which reduces the spring discharge compared to GSWP3 (Fig. 12). The excessive persistence of the snow cover can explain the delay of the LAI increase occurrence in the simulations, which may in turn contribute to too early simulated peak flow, also coupled to floodplain buffering. The Yukon, Mackenzie, Ob and Lena rivers have large floodplain areas and wetlands (and, in the Yukon and Mackenzie basins, lakes that enhance the floodplain buffer) that retain snowmelt water (Ringeval et al., 2012), and should attenuate the peak discharge in spring and sustain a significant summer discharge. The ORCHIDEE-MICT model uses a predefined floodplain map from GLWD (Lehner and Döll, 2004), but flooded area data products (e.g., Prigent et al., 2016) show that wider areas are flooded in these catchments in spring, suggesting that better discharge could be obtained by connecting these larger floodplains and wetlands to the river routing scheme. This highlights complex potential interactions between the snow, vegetation, and river discharge dynamics, the overall results of which remain highly uncertain.

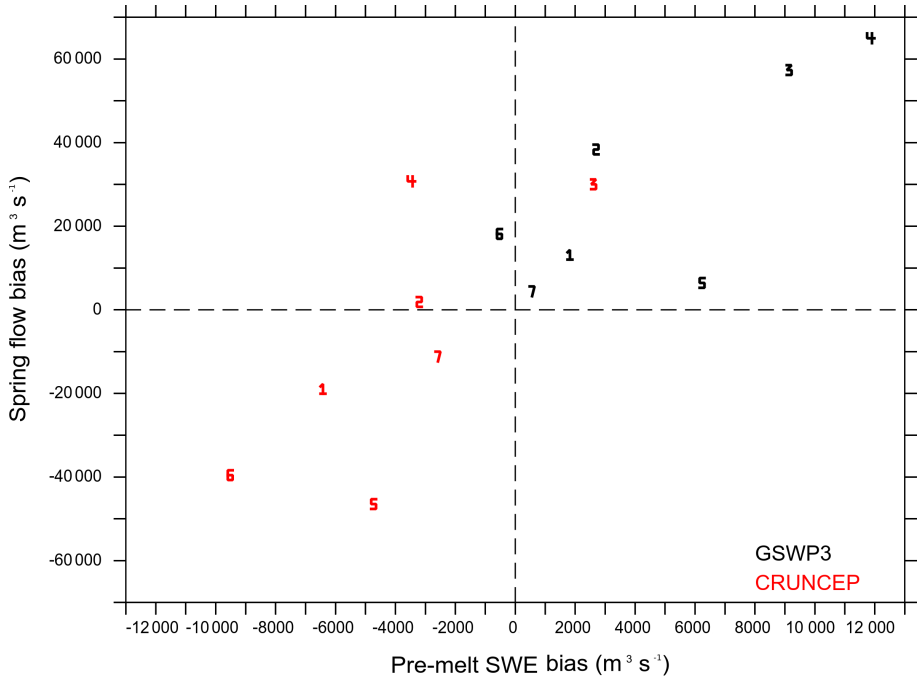

Figure 22. Scatter plot of the pre-melt SWE bias ($m^3 s^{-1}$) defined as the difference between simulated and observed values during the pre-melt season (between February and March) vs. the spring river discharge bias (total discharge at the mouth of the river between April and June) ($m^3 s^{-1}$), averaged over the period 1981–2007. Each number corresponds to one basin: 1: Yukon, 2: Mackenzie, 3: Volga, 4: Ob, 5: Yenisei, 6: Lena and 7: Kolyma (see Fig. 2b). One color represents the result with one atmospheric forcing.

10.2 Seasonal rectification of soil temperature in the atmosphere–snow–soil continuum

A realistic modeling of soil temperature in cold regions requires not only a good soil thermal scheme, but also a good parameterization of snow insulation processes which strongly modulate soil temperatures during winter, as well as a realistic soil–plant hydrology which affects heat transfer in the air–soil interface during summer through ET, and in spring and fall through latent heat uptake and release. Therefore, a better understanding and evaluation of model behaviors call for an integrated examination of all these elements.

In this study, we showed that biases in modeled winter soil temperatures (Fig. 5) are connected with biases in snow depth (Fig. 3), while error compensations seem to exist in terms of snow depth and snow thermal conductivity. The model forced by the GSWP3 climate forcing, which has higher snowfalls than CRUNCEP forcing (Fig. S12), produces significantly larger snow depth and warmer winter soil temperatures than by CRUNCEP. However, the diagnosis from the relationship between ΔT and snow depth, which reveals the model's intrinsic parameterization of snow insulation irrespective of snow depth, shows similar patterns to both GSWP3 and CRUNCEP forcings (Fig. 6). The model can generally capture the broad characters in the ΔT–snow depth relationship, including the different ΔT regimes for different periods of the snow season, yet underestimates the insulation given the same snow depth, compared to observations. This indicates an overestimation of the effective thermal conductivity of snow. In the snow module of ORCHIDEE-MICT, snow compaction is parameterized such that snow density increases due to the weight of the overlying snow, while the top layer of snow keeps relatively low density due to fresh snowfall; thermal conductivity of snow then evolves with time and depth, calculated as a nonlinear function of snow density (Wang et al., 2013). Recent field measurements for Arctic snow, however, show that the formation of a thin layer of soft depth hoar at the base of the snowpack, with its low thermal conductivity around $0.025\,W\,m^{-1}\,K^{-1}$ which is 10 times smaller than the intermediate snow layers, significantly re-shapes the vertical profile of snow thermal conductivity (Domine et al., 2016). It is therefore important to account for such complex metamorphic conditions of snowpack, especially in Arctic/sub-Arctic regions, in order to better model the soil thermal regime in permafrost regions.

Soil temperature during the thawing season is a key driver for microbial decomposition of soil organic carbon at the high latitudes; hence its realistic representation is crucial in modeling the carbon cycle in permafrost regions. ORCHIDEE-MICT produces reasonable summer-time soil temperature and ALT in general, but significant discrepancies exist between the results of the model forced by the two climate forcings (Figs. 5 and 7). As the monthly mean gridded air temperatures of GSWP3 and CRUNCEP forc-

ings are almost identical (Fig. S11), both coming from the CRU data, the differences in the two results are mainly induced by other meteorological fields. A model intercomparison study (Peng et al., 2016) has reported that the surface incident longwave radiation is one of the dominant drivers of soil temperature trends in LSMs. Indeed, GSWP3 forcing has a systematically higher downward longwave radiation than CRUNCEP (Fig. S15), partly explaining the higher land skin and soil temperatures and deeper ALT with GSWP3 than with CRUNCEP forcing (Figs. 4, 5 and 7). What is more, the interactions with hydrology and vegetation also play an important role. The higher ET in Siberian permafrost regions with CRUNCEP than with GSWP3 forcing (Fig. 11a), which is probably driven by the higher LAI in the same regions (Fig. 13), leads to more cooling for the land surface through latent heat release. Besides, the strong cold bias in winter soil temperatures with CRUNCEP forcing affects summer temperature through thermal inertia, especially for the deeper soils below topsoil. All these elements are interconnected, again highlighting the importance of synthetic evaluation of different yet related model aspects in improving our understanding of the system.

Previous land surface modeling studies have shown the critical role of organic matter in soil thermodynamics in permafrost regions (e.g., Lawrence et al., 2008; Chadburn et al., 2015b), while different parameterizations of such effects are implemented in different models. Most of the recent models, like CLM (Lawrence et al., 2008), JULES (Chadburn et al., 2015a), ISBA (Decharme et al., 2016), and ORCHIDEE-MICT in this study, assume weighted combinations of organic soil and mineral soil in the calculation of soil physical parameters for each soil layer in the model. This structure is more flexible than a fixed thickness of organic layer or moss layer as the implementation in JSBACH (Ekici et al., 2014), since the former could approximate the latter by assuming 100 % organic soil above the prescribed thickness. Note that for the insulating effect of moss/lichen layer, the same values of thermal properties as that of the organic soil have usually been used in recent models (Chadburn et al., 2015a; Porada et al., 2016). In this study, however, we did not apply a fixed moss layer in the thermal module for the regional simulations, due to the lack of a gridded map for moss/lichen ground covers especially on the boreal forest floor, and due to the lack of a representation for dynamic moss/lichen coverage as in JULES (Chadburn et al., 2015a) and JSBACH (Porada et al., 2016). This could partly explain the regionally overestimated ALT compared to the empirical map for Yakutia (Fig. S5). An explicit representation for non-vascular plants in ORCHIDEE (Druel et al., 2017) has been worked in parallel with this study at the moment, but would be incorporated into ORCHIDEE-MICT in the future developments.

10.3 Ability of ORCHIDEE-MICT to simulate northern land carbon fluxes and pools

Figure 23 shows the land carbon fluxes and pools modeled and derived from observations (datasets used in the text) in the model domain > 30° N. Modeled estimates encompass the range of observations, except for the deep SOC pool, where the model underestimates SOC. The same figures for each northern region are given in Fig. S10. At the regional level, model-observed agreement still holds.

Arguably, the main variables that should be well simulated for a high-latitude land ecosystem model regarding future carbon-cycle climate feedbacks (Koven et al., 2013; Burke et al., 2017a) are the carbon stocks in biomass, litter and soils. In this respect, ORCHIDEE-MICT performs generally well for biomass with GSWP3 forcing, including the latitudinal profile, showing a peak between 50 and 60° N, despite the simple constant background mortality used for forest (Krinner et al., 2005) in a region where harsh climate is known to induce mortality events. Note that the DGVM version of ORCHIDEE-MICT has a climate- and PFT-dependent mortality (Zhu et al., 2015) which was adjusted to reproduce the distribution of vegetation types, but it was not activated in this study aiming to reproduce observed stocks from an observed vegetation map. The inclusion of climate-dependent fires adds another factor of mortality in this study. From simulated burned area and fire-induced biomass suppression, we calculated that fires add a mortality of 0.4 % yr^{-1} of biomass in BONA, 0.3 % yr^{-1} in BONEU and 0.6 % yr^{-1} in BOAS, compared to the fixed background mortality rates of 1.25 %. Thus fire is a non-negligible component of biomass mortality, controlling the modeled turnover of forest biomass (Thurner et al., 2016). Interestingly, ORCHIDEE-MICT can reproduce the latitudinal gradient of biomass stocks well, even in warmer regions where NPP is lower than observed (compare Figs. 20 and 15b). This suggests a possible error compensation with too small mortality and NPP in the southern boreal forests. Lack of representation of forest management, and under-representation of other natural disturbances (insect, wind, etc.), could collectively contribute to an overall underestimation of biomass turnover. Carvalhais et al. (2014) reported an average turnover of 53.5 years for boreal forests, using extrapolated global soil database and satellite-derived biomass and GPP estimations. Their estimation of the turnover time integrates both biomass and soil C. Given a longer soil carbon turnover than biomass, the biomass turnover of boreal forests should be smaller than 53.5 years. While ORCHIDEE-derived turnover is between 54 (adding together fire and background mortality) and 80 years (assuming only a 1.25 % background mortality) with a lower boundary close to Carvalhais et al. (2014), given that forest fires impact only a small fraction of forests each year (0.1–3 % on annual basis), the ultimate turnover time in the model could be much longer than Carvalhais et al. (2014). The last factor for overestimation of biomass is that ORCHIDEE rep-

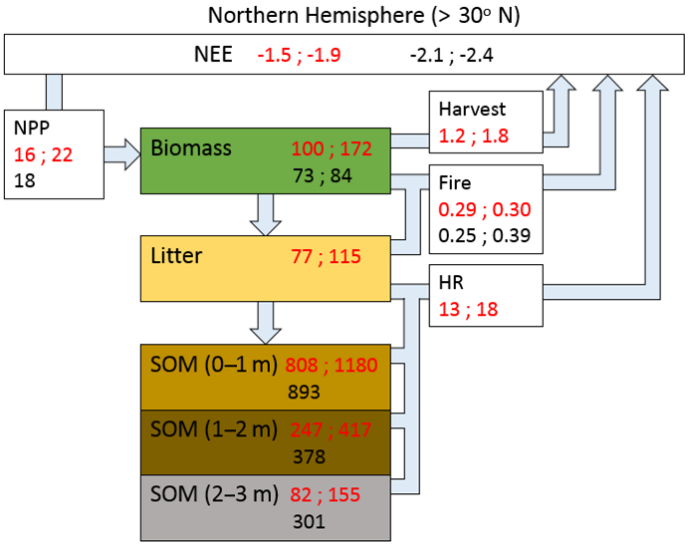

Figure 23. Annual mean land carbon fluxes ($\mathrm{Pg\,C\,yr^{-1}}$) and pool sizes ($\mathrm{Pg\,C}$), averaged over the terrestrial domain higher than 30° N, for the period 2000–2007. The red numbers are the results of the model forced by (left) GSWP3 and (right) CRUNCEP. The black numbers are from observation-based estimates used in the text: NPP from MODIS (NTSG), fire emissions from the (left) GFED4s and (right) GFAS datasets, harvest fluxes including crop harvest and wood product decay in the model (for simplicity, the change in wood product pools is not represented), NEE from the two atmospheric inversions (left) Jena CarboScope and (right) CAMS, forest biomass from (left) Avitabile et al. (2016) and (right) Thurner et al. (2014), and soil carbon from NCSCD (Hugelius et al., 2013) in permafrost regions and HWSD in non-permafrost regions.

resents a mature forest state everywhere due to a lack of age structure in the model, whereas in reality disturbances and management have led to a forest age younger than a mature one.

Regarding SOC, it is critical for carbon climate feedbacks that models can simulate the large current SOC stocks of the high latitudes. This is a particularly difficult problem since frozen high-latitude SOC was formed during the Pleistocene (Yedoma) or the Holocene (peat and tundra soils) through processes that are not incorporated as routine into current models, despite efforts in this direction, e.g., Zhu et al. (2016) for Yedoma and Kleinen et al. (2012) and Spahni et al. (2011) for Holocene peat deposits. The incorporation of slow-forming high-latitude carbon deposits also requires climate history for deeper past periods. In order to reproduce the burial of SOC below the active layer, the strategy followed in ORCHIDEE-MICT is inspired by Koven et al. (2009), who used a diffusion equation to move carbon in the permafrost where no decomposition occurs. Other studies (Koven et al., 2013; Burke et al., 2017a) further limited the rate of decomposition of SOC at depth, to reproduce the lack of oxygen inhibiting decomposition. It should be noted also that the decomposition scheme of SOC is still based on Parton et al. (1988) as classically done in land surface models (Friedlingstein et al., 2006). Different approaches were proposed in models focusing only on SOC decomposition (Wutzler and Reichstein, 2008; Manzoni and Porporato, 2009) based on different assumptions (substrate-driven, decomposer-driven, etc.), but no clear consensus has emerged to date to revise the SOC decomposition scheme in land surface models (Luo et al., 2016). Here we argue that the key to the simulation of a high and realistic SOC stock is the correct representation of soil thermics, illustrated in Fig. 5. A detailed study of the sensitivity of modeled SOC to soil thermics during the spin-up phase will be presented in a follow-up study, but we have already found, comparing SOC with CRUNCEP and GSWP3 climate forcings, the latter giving warmer soil temperature profiles, that SOC is indeed lower in GSWP3. Overall, the simulated circumboreal SOC stocks are comparable with NCSD observations (Fig. 21). This suggests that simulating the formation of frozen carbon with a diffusion-related burial process gives a good performance for the model, although the too stiff profile of SOC (Fig. 21) indicates that a further inhibition of respiration in deep horizons could improve the modeled vertical distribution. Other processes that would tend to make the vertical profile of SOC more uniform with depth is the omission of interactions between SOM and the physical soil environment (Doetterl et al., 2015; Tipping et al., 2016). Modeled SOC is too low in regions covered by peat (lowland Hudson Bay, Ob northern and central basin) and Yedoma (northeastern Siberia and Alaska) (Fig. 21), suggesting that adding these two SOC formation processes should further improve the modeled SOC patterns in longitude, and that in non-peat and non-Yedoma regions, there is no significant model bias for SOC.

Second, for research related to biophysical vegetation–climate feedbacks and understanding the current variability of the carbon cycle, having a correct seasonal representation of GPP, NPP and of the related plant transpiration is a critical requirement for a LSM. The phase of simulated LAI in spring lags satellite observations, in particular for BONA and BOAS sub-regions (Fig. 13). We argued that this lag is related to the late persistence of the snow cover. However, a recent work (Chadburn et al., 2017) shows a late onset even in the absence of snow persistence on site simulations by ORCHIDEE. This calls for a revisit of the phenology-related thresholds at the high latitudes, perhaps by introducing new PFTs (arctic C3 grass and shrub, and non-vascular plants), with their separate set of parameters calibrated, to better represent Arctic vegetation and their phenology (Druel et al., 2017). There is also a lag of GPP (Fig. 14), and of ET (Fig. 11a), but of smaller length (~ 15 days) compared to the lag of LAI. In order to further analyze why the lag of GPP (and ET) in spring is shorter than the one of LAI, we represent separately monthly GPP and LAI for deciduous and evergreen PFTs (Fig. S9). The phase of GPP coincides with that of LAI in deciduous, whereas GPP increases in spring as soil thaw faster and earlier than LAI for evergreens. Thus, it is the modeled spring decoupling between GPP and LAI in evergreen forest that explains the phase bias of GPP being smaller than that of LAI. Note that evergreen tree GPP is modeled to increase rapidly in early spring ORCHIDEE-MICT, even if the model has an inhibition of Vcmax when previous monthly air temperature remains below $-4\,^{\circ}$C (Krinner et al., 2005) to reproduce impaired photosynthesis observed in conifers, a physiological measure to avoid frost damage of photosystems (Leinonen, 1996; Tanja et al., 2003).

Peak summer GPP is overestimated in the BONA and BOEU sub-regions compared to MTE-GPP (Fig. 14), and mean GPP is underestimated at southern sites in western Europe and the US, where $T > 7\,^{\circ}$C (Fig. 16a). We checked that underestimated GPP at warmer sites and in eastern Siberia for the deciduous needle-leaved forest PFT (larch) is due to an overestimation of water stress in summer by the model, since ET is also lower than observed at all the warmer sites. Without the dynamic root allocation to optimize water use in the root zone (see Sect. 4.3), GPP in eastern Siberia would be even lower compared to MTE-GPP (not shown). Lastly, regarding the timing of GPP decrease in fall, ORCHIDEE-MICT shows good performances (Fig. 14) despite the lack of an explicit senescence model for conifers.

Interestingly the reasonable seasonal phase of simulated GPP (Fig. 14) can be contrasted with the larger lag of spring NEE uptake compared to inversion results (Fig. 19). This may be partly explained by the underestimated GPP at the beginning of the growing season (Fig. 14), and also by a possibly too big soil respiration in spring. The moss/lichen surface coverage could be over 70 % under the vast boreal forests (Porada et al., 2016), but we did not prescribe an additional moss layer in the regional simulations, which could lead to a too early thawing of the soil in spring.

The connection between modeled GPP and carbon pools takes place through NPP and its allocation to interconnected pools of variable turnovers. Of critical importance is thus the ability of the model to reproduce CUE, which defines the ratio of NPP to GPP, i.e., carbon available for ecosystem pools. Piao et al. (2010) showed that CUE of forest decreases from 0.5 to 0.3 between 10 and $-10\,^{\circ}$C, due to higher maintenance needs of trees, e.g., to recover from cavitation in spring or maintain tissues during the cold-season period. While mean CUE is correctly simulated (Fig. 17), ORCHIDEE-MICT does not capture its observed decrease towards colder temperatures (data not shown), possibly because allocation and NPP are not driven by sink considerations (Körner, 2003; Fatichi et al., 2014) and thus too much GPP is used to make NPP at colder temperatures.

11 Conclusions

This study has described the inclusion of parameterizations which link soil carbon content and its decomposition rates with permafrost physics and hydrology in the ORCHIDEE-MICT land surface model. The effects of soil organic matter on soil thermal and hydraulic properties are incorporated. The model was evaluated against temperature gradients between the atmosphere and deep soils, and reasonably captured active layer thickness, northern permafrost extent, and soil carbon stocks and profiles. We have shown that the simulated water balance components and their seasonal transition between cold season storage, mostly in solid form, and warm season loss are comparable to observations. Naturally, there remains significant room for improvement. The model appears to underestimate evapotranspiration and overestimate surface temperatures, particularly in the southern portion of the boreal zone. Simulated phenology shows generally a delay in the onset of the growing season. And the snow module underestimates the thermal insulation of snow. Through the use of two different climate forcing datasets across all diagnostic variables, we found that for a large number of these, the variation in output arising from the choice of a forcing was as large as the discrepancy between model and observations. This raises a caution flag against "over-calibrating" the parameters of a LSM to match measured quantities in the presence of large biases in climate input datasets. One critical aspect of forcing data in this respect is the partitioning of precipitation between snowfall and rainfall, which appears to produce a large difference in modeled snow mass and depth. Future improvements of the ORCHIDEE-MICT model include the need for a better floodplain parameterization (Lauerwald et al., 2017) and a better representation of floodplain areas and wetland effects on river discharge. Including an explicit senescence inception model in ORCHIDEE-MICT may contribute to correct the excessive

persistence of LAI during the fall, or even winter in the Yukon and Mackenzie basins. The subgrid-scale representation of permafrost hydrology in discontinuous permafrost areas may be necessary, as might a more realistic description of the slow processes that accumulate carbon in the soil (peat, yedoma, erosion) on very long timescales.

Code and data availability. The source code for ORCHIDEE-MICT version 8.4.1 is available online, but its access is restricted. Consequently, one is required to communicate with the corresponding author for a username and password. The source code can be found at the following address: https://forge.ipsl.jussieu.fr/orchidee/browser/branches/ORCHIDEE-MICT/tags/ORCHIDEE_MICT_8.4.1.

Primary data and scripts used in the analysis and other supplementary information that may be useful in reproducing the author's work can be obtained by contacting the corresponding author.

This software is governed by the CeCILL license under French law and abiding by the rules of distribution of free software. You can use, modify and/or redistribute the software under the terms of the CeCILL license as circulated by CEA, CNRS and INRIA at the following URL: http://www.cecill.info.

Appendix A: Evaluation datasets for the water budget

A1 Total terrestrial water storage

The change in total terrestrial water storage (TWS) is an integrated measure of the ability of a LSM to partition the cold season storage of water as snow and ice, and its decrease from losses to downstream river discharge, plant and soil evapotranspiration, and soil moisture increase. Alkama et al. (2010) showed with the ISBA-TRIP model that seasonal variations in TWS over high-latitude basins resulted primarily from snow accumulation in the cold season, despite a wintertime underestimation of TWS values. Decreasing soil moisture contributed to a small decrease in springtime TWS, while exports with river flow increased dramatically during the snowmelt period. The GRACE (Gravity Recovery And Climate Experiment) satellite mission permits estimation of monthly TWS variations through measurements of the Earth's gravitational field. Three solutions, at 1° resolution, based on spherical harmonic coefficients (Release 05), are obtained by different processing centers, CSR (Center for Space Research), JPL (Jet Propulsion Laboratory) and GFZ (GeoForschungsZentrum Potsdam), and provided in the GRACE Tellus dataset (Swenson and Wahr, 2006; Swenson, 2012; Landerer and Swenson, 2012). We use the ensemble mean of these solutions to reduce uncertainty in GRACE data (Sakumura et al., 2014). To compare TWS simulated by ORCHIDEE-MICT to GRACE data over the common time period between the two meteorological forcing datasets and GRACE data (July 2003–December 2007), we summed the water stocks simulated by ORCHIDEE-MICT, i.e., soil moisture, snowpack, water on the canopy and water stored for the routing reservoirs. In each grid cell, the corresponding 5-year average is removed from the 2003–2007 time series of TWS output from ORCHIDEE-MICT. The comparison of simulated TWS with GRACE data over seven basins in this study (Fig. 2b) is statistically satisfactory given large surface areas occupied by these basins ($> 400\,000\,km^2$ (see Table S4), Swenson et al., 2003).

A2 Snow water mass

The GlobSnow v2.0 SWE dataset is based on a data-assimilation approach combining space-borne passive radiometer data (SMMR, SSM/I and SSMIS) with data from ground-based synoptic weather stations. The record provides SWE information on a daily, weekly and monthly basis, at a spatial resolution of approximately 25 km (in EASE-Grid format), and applies to non-mountainous regions of the Northern Hemisphere, excluding glaciers and Greenland. The product is based on the SWE retrieval methodology developed by Pulliainen (2006) complemented by a time-series melt-detection algorithm (Takala et al., 2009). A complete description of its methodology is given in Takala et al. (2011). SWE estimates are complemented with uncertainty data at the grid cell scale. This work uses monthly averages of original daily data, interpolated to a 1° grid for appropriate comparison with ORCHIDEE-MICT output.

A3 Evapotranspiration (split into components)

The Global Land Evaporation Amsterdam Model (GLEAM) (Miralles et al., 2011) estimates the daily terrestrial ET rate and its components (transpiration, bare-soil evaporation, open-water evaporation, interception loss and sublimation), as well as root-zone soil moisture, at a spatial resolution of 0.25°. It is driven by microwave remote sensing observations and uses satellite soil moisture to constrain potential evaporation rate. The latter is computed with the equation of Priestley and Taylor (1972), which is based on air temperature and net radiation. In the GLEAM v3 product (Martens et al., 2017), representation of evaporative stress has been improved by the use of microwave vegetation optical depth as a proxy for vegetation water content. Other improvements include the use of satellite-based SWE, reanalysis air temperature and radiation, and a multi-source precipitation product. GLEAM v3 contains three sub-versions: version v3.0a is an assimilated product derived from satellite observations and multiple reanalysis climate forcing, while v3.0b and v3.0c are purely satellite-based products. As the latter two do not provide full coverage of high-latitude regions (only 50° S–50° N), v3.0a, which covers the period 1980–2014, is used in our study. We use monthly averages of original daily data, interpolated to a 1° grid for appropriate comparison with ORCHIDEE-MICT output.

A4 River discharge

We use two river discharge databases, one global and another exclusively covering Siberia: the Global Runoff Data Centre (GRDC) product is a global database which collected river discharge data from nearly 7800 stations in 156 countries for the (maximum) period 1807–2017. We use one gauging station per river, the closest to the mouth of the river. For Siberia, we also use daily river discharge at the three gauges in three large Siberian rivers (the Ob, Yenisei and Lena) which have been reconstructed (naturalized discharge) to exclude the human impact from the data. This has been performed by using the Hydrograph Routing Model (HRM) developed at the University of New Hampshire (USA) in collaboration with the Arctic and Antarctic Research Institute (Russia) (Shiklomanov and Lammers, 2009). We use monthly averages of original daily data.

A5 Topsoil moisture

The global ESA CCI SM product (v2.2) provides daily soil moisture (in volumetric units: $m^3\,m^{-3}$), at a spatial resolution of 25 km with quality flags specifying potential sources of errors linked to the presence of water bodies, dense vegetation, snow or frozen soils in the pixel area. Three datasets

are provided based on different combinations of active and passive satellite sensors. In this work, we used the combined active and passive product which covers the whole period from November 1978 to December 2014. The product results from the merging of soil moisture estimations inversed from two types of instruments and two methodologies: passive microwave radiometers (SMMR, SSM/I, TMI, AMSR-E, AMSR2 and WindSat) using the methodology developed by Owe et al. (2008) and active microwave instruments (ERS-1 and 2 and ASCAT) using the algorithm developed by the TU-Wien (Wagner et al., 1999; Bartalis et al., 2007). These two records were first rescaled together and merged with topsoil (10 cm) soil moisture simulations of the GLDAS-NOAH LSM using a CDF-matching approach. Data accuracy was estimated against in situ measurements (Dorigo et al., 2015) to 0.05 $m^3 m^{-3}$.

A6 Root-zone soil moisture

The GLEAM root-zone soil moisture v3.0a database (Martens et al., 2017) is based on both satellite observations and reanalysis data. It is a mixture of the soil water content of three soil tiles: bare soil (0–10 cm), and herbaceous (0–100 cm) and tall vegetation (0–250 cm). The tile fractions are static and derived from the MODerate resolution Imaging Spectroradiometer (MODIS) Global Vegetation Continuous Fields product (MOD44B, Hansen et al., 2005). Obviously, it is hard to compare the ORCHIDEE soil moisture with the GLEAM root-zone soil moisture directly, not only due to the mismatch of defined soil tile depth, but also due to the difference of soil tile fractions. Thus we implement the comparison after normalization of the relative soil moisture values with their respective SD, following Koster et al. (2009).

Appendix B: Evaluation datasets for the air-to-soil temperature continuum

B1 Snow depth

Realistically simulating snow depth is one of the prerequisites for accurately modeling soil thermal dynamics, particularly in winter. Daily snow depth in situ data (1975–2005) from 524, 72, 528, 128 and 528 stations in Europe, Canada, USA, Russia and China were obtained from the European Climate Assessment & Dataset (ECA&D), the National Climate Data and Information Archive of Environment Canada, the United States Historical Climatology Network (USHCN), the Russian Research Institute of Hydrometeorological Information–World Data Center (RIHMI-WDC) (Bulygina et al., 2011), and the National Meteorological Information Center of the China Meteorological Administration (Peng et al., 2010), respectively. Monthly averages were calculated when more than 2/3 of daily snow depth data were available.

B2 Surface soil temperature

The soil temperature product used here (André et al., 2015) resulted from the use of combined passive microwave and thermal infrared data to estimate land surface temperature (LST), during summer snow-free periods (snow-covered pixels are masked) at the northern high latitudes. The product is based on the use of SSM/I-SSMIS 37 GHz measurements at both vertical and horizontal polarizations and is provided on a 25 km resolution EASE grid at a 1 h time step for the period 2000–2011. LST retrievals are based on the assumption of a relationship between surface emissivities at both polarizations (Royer and Poirier, 2010) which was calibrated at pixel scale using cloud-free independent LST data from MODIS instruments. The SSM/I-SSMIS and MODIS data were synchronized by fitting a diurnal cycle model built on skin temperature with reanalysis provided by the European Centre for Medium-Range Weather Forecasts (ECMWF). This product was evaluated at local and circumpolar scales against MODIS LST, and the results show a root mean square error (RMSE) on the order of 2.5 K.

B3 In situ air and soil temperatures

Simultaneous measurements of snow depth, near-surface air temperature and topsoil (at 20 cm depth) temperature from Russian meteorological stations (Bulygina et al., 2011; Sherstiukov, 2012) are used to evaluate the thermal insulating effect of snow during winter, by comparing the relationships between snow depth and the air-to-topsoil temperature gradient (ΔT) (W. Wang et al., 2016). This dataset includes monthly mean values at 268 sites for the period 1980–2000.

B4 Active-layer thickness

The Circumpolar Active Layer Monitoring (CALM) network's in situ dataset was used to evaluate modeled soil active layer thickness. The CALM network aims to observe the response of near-surface permafrost and the active layer to climate change over long timescales. Thaw depth is measured at the end of the thawing season, so that it should be comparable to the maximum active layer thickness in the model. Before comparing to ORCHIDEE-MICT, the data from 221 sites were averaged from 1990 to 2015.

In addition, we used the active layer thickness map derived by Beer et al. (2013) over Yakutia at a spatial resolution of 0.5°. It is based on regional surveys of landscapes and permafrost conditions in Yakutia during the time period 1960–1987. The gridded datasets can be accessed at the PANGAEA repository. Values of active layer thickness (ALT) in this region range between 0.3 m north of 70° N and 3 m south of 65° N. Uncertainty increases with ALT and is highest (up to 1 m) in the south because of the occurrence of discontinuous and sporadic permafrost landscapes.

Appendix C: Evaluation datasets for leaf area, carbon stocks and fluxes

C1 Leaf area index

The leaf area index (LAI) can be derived from satellite measurements, using reflectance measurements and land cover maps. Comparing the seasonal cycle of the satellite products with simulated LAI gives information on the appropriateness of the phenology modules. The amplitude of the cycle is also informative with respect to several photosynthetic parameters (e.g., maximum carboxylation rate Vcmax or specific leaf area).

GIMMS

The Global Inventory Modeling and Mapping Studies (GIMMS) LAI3g dataset is derived from Advanced Very High Resolution Radiometers (AVHRR) measurements. It is more specifically computed from the GIMMS Normalized Difference Vegetation Index (NDVI) 3g, using a neural network and the International Geosphere Biosphere Programme (IGBP) land cover classes (Zhu et al., 2013). The $1/12°$ files cover 30 years from July 1981 to December 2011, at a biweekly resolution. They were aggregated at a 1.0° spatial resolution on the model grid, to enable comparisons of the time series and maps.

GLASS

The Global Land Surface Products (GLASS) LAI product (Liang and Xiao, 2012) is built from AVHRR reflectances over the period 1982–1999 and then from MODIS data over 2000–2012 (Collection 5). The processing is also based on a neural network and the eight biomes of MODIS land cover type 3 (Xiao et al., 2014). The files are available at a spatial resolution of 0.05° with an 8-day frequency and were aggregated at 1.0° spatial resolution.

C2 NEE from atmospheric inversions

We use estimates of NEE (here the net land–atmosphere CO_2 fluxes excluding fossil fuel CO_2 emissions) from two atmospheric inversions where NEE is optimized at the resolution of a global atmospheric transport model each month to match observed CO_2 concentration gradients from a global network of ground-based stations. The inversions are the Copernicus Atmosphere Monitoring Service (CAMS) inversion system (Chevallier et al., 2010) and the Jena CarboScope (Rödenbeck, 2005).

The inversion from CAMS uses atmospheric CO_2 concentration observations from a total of 132 sites covering the period 1979–2015 and includes all sites being added to the network though time, combined with the LMDZ INCA atmospheric transport model and prior information about fossil-fuel CO_2 emissions (from the EDGAR3.2 FastTrack 2000 database) as well as land/ocean–atmosphere fluxes, to minimize a cost function in order to calculate NEE. Here we use the latest version (15r4), in which monthly fluxes are calculated at $1.875° \times 3.75°$ lat–lon resolution.

The Jena CarboScope atmospheric inversion uses the same set of atmospheric CO_2 observation sites available during the temporal observation period (1996–2015) referred to as Jena s96. Jena CarboScope inversion uses fossil fuel emissions from EDGAR 4.2 and the TM3 global atmospheric transport models. Here we use monthly NEE from the latest version of Jena s96 (v3.8), which is provided at $3.8° \times 5.0°$ lat–lon resolution.

C3 Site-level GPP and NPP observations

In situ GPP and NPP measurements

While there are several NPP datasets especially for forest (e.g., Cannel et al., 1992; Olson et al., 2001; Michaletz et al., 2014), few provide both GPP and NPP at the same locations. We used a recent database of in situ co-located GPP and NPP measurements (Campioli et al., 2015), which is an extension of the Luyssaert et al. (2007) database for forests. The database consists of 131 sites, for which annual NPP obtained from biometric measurements and associated uncertainties are provided. The criteria employed by Campioli et al. (2015) for selecting the sites was the availability of methodologically independent and site-specific estimates of NPP and GPP. Carbon use efficiency (CUE) was calculated at each site by taking the ratio of NPP to GPP. Site-level biomes are classified as one of tundra, boreal peatlands, marshes, forests, grasslands or croplands. To study the temperature sensitivity of GPP and NPP, we selected only sites northward of 30° N, where model grid cells were representative of both the vegetation type and meteorological conditions observed at each site. We thus restricted the selection to sites whose IGBP vegetation type had a corresponding fraction greater than 0.5 in the grid cell of the ISLSCP II MODIS IGBP Land Cover product (Friedl et al., 2010). Site years where the absolute difference between local and mean annual temperature (MAT) of the GSWP3 or the CRUNCEP climate forcing fields was higher than 4° were discarded. As no information was given about the time period of site NPP and GPP observations in Campioli et al. (2015), we compared them to mean values of the model over the period 2000–2007. The subset of selected sites consisted then of 52 sites out of 131 in the full dataset.

C4 Gridded GPP and NPP observation-based data

GPP

In addition to GPP from sites, we used the monthly gridded GPP observation-based product Model Ensemble Tree GPP (MTE-GPP) from Jung et al. (2009, 2011) from years 1982 to 2010. This product is the result of a statistical model that

combines measurements at FLUXNET sites with geospatial information from satellite remote sensing (fAPAR) and meteorological data. MTE-GPP is obtained as the median from an ensemble of the 25 best model trees out of an initial set of 1000 and the mean absolute deviation (MAD) of the ensemble is used to define the uncertainty of MTE-GPP, which is also provided as a monthly gridded product. This uncertainty estimate was mentioned by Jung et al. (2011) to be underestimated as compared to the true RMSE. That is why we consider the RMSE from the cross-validation sites as an estimate of uncertainty. The RMSE of mean MTE-GPP at cross-validation sites is $270\,\mathrm{g\,C\,m^{-2}\,yr^{-1}}$. At global scale and over the period 1982–2008, the mean MTE-GPP is $933 \pm 46\,\mathrm{g\,C\,m^{-2}\,yr^{-1}}$ and the total is $119 \pm 6\,\mathrm{Gt\,C\,yr^{-1}}$, the uncertainties being derived from the MAD of the MTE (Jung et al., 2011).

NPP

We use the MOD17A3.005 global annual NPP model driven by satellite observations from the NASA Land Processes Distributed Active Archive Center, at 1 km resolution and aggregated to the 1° grid of the model over the period 2000–2010. Yearly MODIS NPP is computed from yearly and daily components. Among the daily components, MODIS GPP is based upon a LUE model:

$$\mathrm{GPP} = E \cdot \mathrm{fAPAR} \cdot \mathrm{PAR}, \tag{C1}$$

where PAR is the photosynthetically active radiation, fAPAR the fraction of absorbed PAR and E the radiation conversion efficiency. E depends on vegetation type and on meteorological conditions (temperature, vapor pressure deficit (VPD)). PAR, temperature and VPD used in MOD17A3.005-NPP are from the NASA Data Assimilation Office (DAO) and fAPAR is a MODIS product (Knyazikhin et al., 1998). A daily maintenance respiration (MR) was computed for leaves (l) and fine roots (fr), using the LAI MODIS product (Knyazikhin et al., 1998). On a yearly basis, MR was computed for livewood (lw) and growth respiration (GR) for leaves, fine roots, livewood and deadwood (dw). These respirations were computed using a biome-specific parameter look-up table, derived from the BIOME-BGC terrestrial biosphere model (Heinsch et al., 2003). This set of parameters was recalibrated for the MOD17A3.005-NPP collection 5 (Zhao et al., 2005). Yearly MODIS-NPP was thus computed as follows (Running et al., 2004):

$$\mathrm{NPP} = \left\{ \sum_{\mathrm{days}} [\mathrm{GPP} - \mathrm{MR(l)} - MR(\mathrm{fr})] \right\} - \mathrm{MR(lw)} - \mathrm{GR(l)} - \mathrm{GR(fr)} - \mathrm{GR(lw)} - \mathrm{GR(dw)}. \tag{C2}$$

Turner et al. (2006) evaluated MODIS NPP at nine sites representing various biomes, using local meteorological, LAI and above ground NPP measurements as inputs for the BIOME-BGC model to derive NPP over a $25\,\mathrm{km}^2$ area. They showed globally no bias, but NPP was underestimated at the most productive sites (attributed to a negative bias of E) and overestimated at low productivity sites (attributed to a positive bias of MODIS fAPAR). Zhao et al. (2005) evaluated MODIS NPP against the Ecosystem Model–Data Intercomparison (EMDI) global database of NPP measurements (Olson et al., 2001) and found a good agreement except for tropical forests (spatial $R^2 = 0.77$). Zhao et al. (2006) estimated the sensitivity of the MODIS NPP product to the use of different meteorological reanalysis input data, showing differences at the global scale up to more than $20\,\mathrm{Pg\,C\,yr^{-1}}$, with the largest differences in the tropics.

C5 Soil carbon inventories

NCSCD

The Northern Circumpolar Soil Carbon Database quantifies storage of organic carbon in soils of the northern circumpolar permafrost region, comprising four depths up to 3 m (0–30, 30–100, 100–200 and 200–300 cm) (Hugelius et al., 2013). Total SOC storage in the 0–2 and 0–3 m depth ranges in northern permafrost soils are estimated to be 827 ± 108 and $1035 \pm 150\,\mathrm{Pg\,C}$, respectively.

SoilGrids

SoilGrids is a global soil information database with spatial predictions for a selection of soil properties, at 1 km resolution and six depths, up to a maximum of 2 m (0–5, 5–15, 15–30, 30–60, 60–100 and 100–200 cm). About 110 000 soil profiles were used to generate the product, using statistical models based on climatic and biomass indices, lithology, and taxonomic mapping units (Hengl et al., 2014). The gridded maps of soil organic carbon mass fraction, soil bulk density, and volumetric fraction of coarse fragments was used to calculate SOC density in the unit of $\mathrm{kg\,C\,m^{-2}}$ to be comparable with model output (see Eq. 6 in Hengl et al., 2014). However, we found in this product a systematic overestimation of bulk density for organic-rich soils, which is similar to the issue found in the HWSD database (Köchy et al., 2015). Therefore, we followed the adjusting method in Köchy et al. (2015) to correct bulk density for histosols and other soils with organic carbon mass fraction larger than 3 %. This adjustment decreases total SOC stock in northern permafrost regions (the same domain as NCSCD) in the 0–2 m depth range from the original 1724 to 1177 PgC, which we considered acceptable though higher than NCSCD.

C6 Biomass carbon stocks

Two forest biomass datasets are used to evaluate simulated forest biomass. The first is that from Avitabile et al. (2016), which, at a spatial resolution of 0.01°, merges two tropical aboveground forest biomass (AGB) datasets from Saatchi

et al. (2011) and Baccini et al. (2012) with Northern Hemisphere volumetric forest stock growth data from Santoro et al. (2015). The second forest biomass dataset from Thurner et al. (2014) is given at a spatial resolution of 0.01° for 2010 and confined to the Northern Hemisphere (30–80° N). This is derived from the Santoro et al. (2011) forest standing stock data. The two datasets were re-gridded to 1° resolution for comparison with model output. The Avitabile et al. (2016) AGB was converted into total biomass, assuming a constant AGB to total biomass ratio of 0.8 and divided by two to obtain total biomass carbon, under the assumption that the carbon content of dry biomass is 50 %. Liu et al. (2015) synthesized ratios of aboveground to total biomass for different forest biomes in temperate and boreal regions and found that they range between 0.76 and 0.84 according to regional forest inventory assessments. Our uniform 0.8 factor for converting the Avitabile et al. (2016) data thus yields a potential error of ~ 5 % in inferred total biomass carbon, which is within the reported data uncertainties given by Avitabile et al. (2016). Simulated equivalent total forest biomass carbon over the period 2000–2007 was compared with observations.

C7 Burned area and fire emissions

We compared the simulated burned area and fire carbon emission with the Global Fire Emissions Database (GFED4s) dataset, which is based on the GFED modeling framework (van der Werf et al., 2010). The GFED4s burned area data are derived from the MODIS sensor data that are then complemented by specific algorithms to retrieve "small fires" (Randerson et al., 2012). Emissions are computed from a combination of burned area with the revised Carnegie–Ames–Stanford-Approach biogeochemical model (CASA-GFED, described in van der Werf et al., 2010) that provides an estimation of fuel loads and combustion completeness. GFED4s data are provided at a 0.25° spatial resolution with a monthly time step for 1997–2015.

Cropland fires are not yet implemented in the ORCHIDEE-MICT model, but are included in the GFED4s dataset. In order to compare the simulation with GFED4s, it was necessary to correct the simulated burned area for the omission of cropland fires. To do so, we computed for each grid cell the fraction of existing natural PFTs (i.e., all non-cropland PFTs), and divided the simulated burned area in each grid cell by this value. For carbon emissions, the GFED4s dataset provides separate emissions data for cropland and natural fires. In this way, we were able to simply remove cropland fire emissions from GFED for comparison with ORCHIDEE-MICT output.

The Supplement related to this article is available online at https://doi.org/10.5194/gmd-11-121-2018-supplement.

Author contributions. MG and DZ led the study. DZ performed the simulations. FM and AJ-P performed the code versioning of ORCHIDEE-MICT; FM managed the scientific aspects of the updates from the main branch (TRUNK); AJ-P optimized the code; they both assisted with technical aspects of the model and its run environment. HK built the GSWP3 dataset and JC adapted its format to be compatible with ORCHIDEE-MICT. DZ developed SOC-dependent soil physical properties in the model and introduced a reformulation of the hydric stress above the permafrost table. She conducted the evaluation of the soil temperature and permafrost area simulated by ORCHIDEE-MICT. YH provided the comparison of the snow depth with dataset. CO and SD-N processed the satellite datasets and interpreted the soil moisture and land surface temperature. AD contributed to the improvement of the hydrological modeling in the initial ORCHIDEE version and MG led the water budget evaluation. ZY contributed to the comparison of soil moisture with GLEAM. MG, RL and SB supervised the routing scheme. CY built an updated version of SPITFIRE in ORCHIDEE-MICT and, with PL, analyzed the results in biomass carbon stocks, burned area and fire emissions. AB provided the comparison of NEE with atmospheric inversions. FM performed the NPP and GPP evaluations over the sites database. BG, MT and DZ conducted the soil carbon evaluation. YW synthesized the carbon budget evaluation. CO, TW, SP and GK supervised the representation of the high-latitude processes in ORCHIDEE-MICT in coherence with the initial version of ORCHIDEE. DG, XW, EJ, CQ and FW assisted in ensuring consistency between the carbon cycle, water cycle and various other processes in ORCHIDEE. PC contributed to the theoretical concept of the modeling of high-latitude processes. All authors contributed to the writing of the manuscript.

Competing interests. The authors declare that they have no conflict of interest.

Acknowledgements. This work was financially supported by the European Research Council Synergy grant ERC-2013-SyG-610028 IMBALANCE-P. We acknowledge the ORCHIDEE-PROJET group, which developed and tested the ORCHIDEE model revision 3976. We thank Natasha MacBean who contributed to the production of the land cover map. We thank Arsène Druel who processed the GLASS LAI data. Simulations with ORCHIDEE-MICT were performed using computational facilities of the Institut du Développement et des Ressources en Informatique Scientifique (IDRIS, CNRS, France) and of the CCRT (CEA). S. Dantec-Nédélec, G. Krinner, P. Ciais and C. Ottlé were supported by the CLASSIQUE national project (ANR grant no. ANR 2010-CEPL-012-02) and the PAGE 21 project (grant agreement number 282700, funded by the EC seventh Framework Programme theme FP7-ENV-2011). A. Ducharne was supported by the IGEM project "Impact of Groundwater in Earth system Models" (ANR grant no. ANR-14-CE01-0018-01). Discharge station data are kindly provided by the Global Runoff Data Centre, 56068 Koblenz, Germany. GRACE land data are available at http://grace.jpl.nasa.gov, supported by the NASA MEaSUREs Program. The MOD17A3.005 data product was retrieved from the online Data Pool, courtesy of the NASA EOSDIS Land Processes Distributed Active Archive Center (LP DAAC), USGS/Earth Resources Observation and Science (EROS) Center, Sioux Falls, South Dakota (https://lpdaac.usgs.gov/data_access/data_pool). Jena CarboScope inversion data were provided by Christian Rödenbeck and are available at http://www.bgc-jena.mpg.de/CarboScope/?ID=s96_v3.8.

Edited by: Hisashi Sato
Reviewed by: two anonymous referees

References

Alkama, R., Decharme, B., Douville, H., Becker, M., Cazenave, A., Sheffield, J., Voldoire, A., Tyteca, S., and Le Moigne, P.: Global evaluation of the ISBA–TRIP continental hydrological system. Part I: Comparison to GRACE terrestrial water storage estimates and in situ river discharges, J. Hydrometeorol., 11, 583–600, https://doi.org/10.1175/2010jhm1211.1, 2010.

André, C., Ottlé, C., Royer, A., and Maignan, F.: Land surface temperature retrieval over circumpolar Arctic using SSM/I–SSMIS and MODIS data, Remote Sens. Environ., 162, 1–10, https://doi.org/10.1016/j.rse.2015.01.028, 2015.

Atanasiu, L.: Photosynthesis and respiration of three mosses at winter low temperatures, Bryologist, 74, 23–27, https://doi.org/10.2307/3241751, 1971.

Avitabile, V., Herold, M., Heuvelink, G. B. M., Lewis, S. L., Phillips, O. L., Asner, G. P., Armston, J., Ashton, P. S., Banin, L., Bayol, N., Berry, N. J., Boeckx, P., de Jong, B. H. J., DeVries, B., Girardin, C. A. J., Kearsley, E., Lindsell, J. A., Lopez-Gonzalez, G., Lucas, R., Malhi, Y., Morel, A., Mitchard, E. T. A., Nagy, L., Qie, L., Quinones, M. J., Ryan, C. M., Ferry, S. J. W., Sunderland, T., Laurin, G. V., Gatti, R. C., Valentini, R., Verbeeck, H., Wijaya, A., and Willcock, S.: An integrated pan-tropical biomass map using multiple reference datasets, Glob. Change Biol., 22, 1406–1420, https://doi.org/10.1111/gcb.13139, 2016.

Baccini, A., Goetz, S. J., Walker, W. S., Laporte, N. T., Sun, M., Sulla-Menashe, D., Hackler, J., Beck, P. S. A., Dubayah, R., Friedl, M. A., Samanta, S., and Houghton, R. A.: Estimated carbon dioxide emissions from tropical deforestation improved by carbon-density maps, Nat. Clim. Change, 2, 182–185, https://doi.org/10.1038/nclimate1354, 2012.

Baldocchi, D. D., Vogel, C. A., and Hall, B.: Seasonal variation of energy and water vapor exchange rates above and below a boreal jack pine forest canopy, J. Geophys. Res.-Atmos., 102, 28939–28951, https://doi.org/10.1029/96jd03325, 1997.

Bartalis, Z., Wagner, W., Naeimi, V., Hasenauer, S., Scipal, K., Bonekamp, H., Figa, J., and Anderson, C.: Initial soil moisture retrievals from the METOP-A Advanced Scatterometer (ASCAT), Geophys. Res. Lett., 34, https://doi.org/10.1029/2007GL031088, l20401, 2007.

Beer, C., Lucht, W., Gerten, D., Thonicke, K., and Schmullius, C.: Effects of soil freezing and thawing on vegetation carbon density in Siberia: a modeling analysis with the Lund–Potsdam–Jena Dynamic Global Vegetation

Model (LPJ-DGVM), Global Biogeochem. Cy., 21, GB1012, https://doi.org/10.1029/2006gb002760, 2007.

Beer, C., Fedorov, A. N., and Torgovkin, Y.: Permafrost temperature and active-layer thickness of Yakutia with 0.5-degree spatial resolution for model evaluation, Earth Syst. Sci. Data, 5, 305–310, https://doi.org/10.5194/essd-5-305-2013, 2013.

Beven, K.: Infiltration into a class of vertically non-uniform soils, Hydrolog. Sci. J., 29, 425–434, https://doi.org/10.1080/02626668409490960, 1984.

Beven, K. and Germann, P.: Macropores and water flow in soils, Water Resour. Res., 18, 1311–1325, https://doi.org/10.1029/WR018i005p01311, 1982.

Biancamaria, S., Bates, P. D., Boone, A., and Mognard, N. M.: Large-scale coupled hydrologic and hydraulic modelling of the Ob river in Siberia, J. Hydrol., 379, 136–150, https://doi.org/10.1016/j.jhydrol.2009.09.054, 2009.

Bontemps, S., Defourny, P., Radoux, J., Van Bogaert, E., Lamarche, C., Achard, F., Mayaux, P., Boettcher, M., Brockmann, C., Kirches, G., Zulkhe, M., Kalogirou, V., Seifert, F., and Arino, O.: Consistent global land cover maps for climate modelling communities: current achievements of the ESA's land cover CCI, in: Proceedings of the ESA Living Planet Symposium, Edinburgh, 9–13 September 2013, 9–13, 2013.

Boone, A. and Etchevers, P.: An intercomparison of three snow schemes of varying complexity coupled to the same land surface model: local-scale evaluation at an Alpine site, J. Hydrometeorol., 2, 374–394, https://doi.org/10.1175/1525-7541(2001)002<0374:AIOTSS>2.0.CO;2, 2001.

Botta, A., Viovy, N., Ciais, P., Friedlingstein, P., and Monfray, P.: A global prognostic scheme of leaf onset using satellite data, Glob. Change Biol., 6, 709–725, https://doi.org/10.1046/j.1365-2486.2000.00362.x, 2000.

Brown, J., Ferrians Jr, O., Heginbottom, J., and Melnikov, E.: Circum-Arctic map of permafrost and ground-ice conditions (Version 2), Boulder, Colorado USA, NSIDC: National Snow and Ice Data Center, 45, 2002.

Bulygina, O., Groisman, P. Y., Razuvaev, V., and Korshunova, N.: Changes in snow cover characteristics over Northern Eurasia since 1966, Environ. Res. Lett., 6, 045204, https://doi.org/10.1088/1748-9326/6/4/045204, 2011.

Burke, E. J., Dankers, R., Jones, C. D., and Wiltshire, A. J.: A retrospective analysis of pan Arctic permafrost using the JULES land surface model, Clim. Dynam., 41, 1025–1038, https://doi.org/10.1007/s00382-012-1648-x, 2013.

Burke, E. J., Chadburn, S. E., and Ekici, A.: A vertical representation of soil carbon in the JULES land surface scheme (vn4.3_permafrost) with a focus on permafrost regions, Geosci. Model Dev., 10, 959–975, https://doi.org/10.5194/gmd-10-959-2017, 2017a.

Burke, E. J., Ekici, A., Huang, Y., Chadburn, S. E., Huntingford, C., Ciais, P., Friedlingstein, P., Peng, S., and Krinner, G.: Quantifying uncertainties of permafrost carbon–climate feedbacks, Biogeosciences, 14, 3051–3066, https://doi.org/10.5194/bg-14-3051-2017, 2017b.

Campioli, M., Vicca, S., Luyssaert, S., Bilcke, J., Ceschia, E., III, F. S. C., Ciais, P., Fernández-Martínez, M., Malhi, Y., Obersteiner, M., Olefeldt, D., Papale, D., Piao, S. L., Peñuelas, J., Sullivan, P. F., Wang, X., Zenone, T., and Janssens, I. A.: Biomass production efficiency controlled by management in temperate and boreal ecosystems, Nat. Geosci., 8, 843–846, https://doi.org/10.1038/ngeo2553, 2015.

Campoy, A., Ducharne, A., Cheruy, F., Hourdin, F., Polcher, J., and Dupont, J.: Response of land surface fluxes and precipitation to different soil bottom hydrological conditions in a general circulation model, J. Geophys. Res.-Atmos., 118, 10725–10739, https://doi.org/10.1002/jgrd.50627, 2013.

Cannel, M., Malcolm, D., and Robertson, P.: The Ecology of Mixed-Species Stands of Trees: Forest Dynamics, Oxford University Press, Oxford, 1992.

Carsel, R. and Parrish, R.: Developing joint probability distributions of soil water retention characteristics, Water Resour. Res., 24, 755–769, https://doi.org/10.1029/WR024i005p00755, 1988.

Carvalhais, N., Forkel, M., Khomik, M., Bellarby, J., Jung, M., Migliavacca, M., Mu, M., Saatchi, S., Santoro, M., Thurner, M., Weber, U., Ahrens, B., Beer, C., Cescatti, A., Randerson, J. T., and Reichstein, M.: Global covariation of carbon turnover times with climate in terrestrial ecosystems, Nature, 514, 213–217, https://doi.org/10.1038/nature13731, 2014.

Chadburn, S., Burke, E., Essery, R., Boike, J., Langer, M., Heikenfeld, M., Cox, P., and Friedlingstein, P.: An improved representation of physical permafrost dynamics in the JULES land-surface model, Geosci. Model Dev., 8, 1493–1508, https://doi.org/10.5194/gmd-8-1493-2015, 2015a.

Chadburn, S. E., Burke, E. J., Essery, R. L. H., Boike, J., Langer, M., Heikenfeld, M., Cox, P. M., and Friedlingstein, P.: Impact of model developments on present and future simulations of permafrost in a global land-surface model, The Cryosphere, 9, 1505–1521, https://doi.org/10.5194/tc-9-1505-2015, 2015b.

Chadburn, S. E., Krinner, G., Porada, P., Bartsch, A., Beer, C., Belelli Marchesini, L., Boike, J., Ekici, A., Elberling, B., Friborg, T., Hugelius, G., Johansson, M., Kuhry, P., Kutzbach, L., Langer, M., Lund, M., Parmentier, F.-J. W., Peng, S., Van Huissteden, K., Wang, T., Westermann, S., Zhu, D., and Burke, E. J.: Carbon stocks and fluxes in the high latitudes: using site-level data to evaluate Earth system models, Biogeosciences, 14, 5143–5169, https://doi.org/10.5194/bg-14-5143-2017, 2017.

Chevallier, F., Ciais, P., Conway, T. J., Aalto, T., Anderson, B. E., Bousquet, P., Brunke, E. G., Ciattaglia, L., Esaki, Y., Fröhlich, M., Gomez, A., Gomez-Pelaez, A. J., Haszpra, L., Krummel, P. B., Langenfelds, R. L., Leuenberger, M., Machida, T., Maignan, F., Matsueda, H., Morgui, J. A., Mukai, H., Nakazawa, T., Peylin, P., Ramonet, M., Rivier, L., Sawa, Y., Schmidt, M., Steele, L. P., Vay, S. A., Vermeulen, A. T., Wofsy, S., and Worthy, D.: CO_2 surface fluxes at grid point scale estimated from a global 21 year reanalysis of atmospheric measurements, J. Geophys. Res.-Atmos., 115, d21307, https://doi.org/10.1029/2010JD013887, 2010.

Chini, L., Hurtt, G., and Frolking, S.: Harmonized Global Land Use for Years 1500–2100, V1. Data set, Oak Ridge National Laboratory Distributed Active Archive Center, Oak Ridge, Tennessee, 2014.

Compo, G. P., Whitaker, J. S., Sardeshmukh, P. D., Matsui, N., Allan, R. J., Yin, X., Gleason, B. E., Vose, R. S., Rutledge, G., Bessemoulin, P., Brönnimann, S., Brunet, M., Crouthamel, R. I., Grant, A. N., Groisman, P. Y., Jones, P. D., Kruk, M. C., Kruger, A. C., Marshall, G. J., Maugeri, M., Mok, H. Y., Nordli, Ø., Ross, T. F., Trigo, R. M., Wang, X. L., Woodruff, S. D., and

Worley, S. J.: The twentieth century reanalysis project, Q. J. Roy. Meteor. Soc., 137, 1–28, https://doi.org/10.1002/qj.776, 2011.

Decharme, B., Brun, E., Boone, A., Delire, C., Le Moigne, P., and Morin, S.: Impacts of snow and organic soils parameterization on northern Eurasian soil temperature profiles simulated by the ISBA land surface model, The Cryosphere, 10, 853–877, https://doi.org/10.5194/tc-10-853-2016, 2016.

de Rosnay, P., Bruen, M., and Polcher, J.: Sensitivity of surface fluxes to the number of layers in the soil model used in GCMs, Geophys. Res. Lett., 27, 3329–3332, https://doi.org/10.1029/2000gl011574, 2000.

de Rosnay, P., Polcher, J., Bruen, M., and Laval, K.: Impact of a physically based soil water flow and soil-plant interaction representation for modeling large-scale land surface processes, J. Geophys. Res.-Atmos., 107, 4118, https://doi.org/10.1029/2001JD000634, 2002.

Doetterl, S., Stevens, A., Six, J., Merckx, R., Oost, K. V., Pinto, M. C., Casanova-Katny, A., Muñoz, C., Boudin, M., Venegas, E. Z., and Boeckx, P.: Soil carbon storage controlled by interactions between geochemistry and climate, Nat. Geosci., 8, 780–783, https://doi.org/10.1038/ngeo2516, 2015.

Domine, F., Krinner, G., Menegoz, M., Bock, J., Gallet, J.-C., and Anttilaa, K.: Snow-climate feedbacks driven by changes in snow thermal conductivity, in: IPY Oslo science conference, 8–12 June 2010, 2010.

Domine, F., Barrere, M., and Sarrazin, D.: Seasonal evolution of the effective thermal conductivity of the snow and the soil in high Arctic herb tundra at Bylot Island, Canada, The Cryosphere, 10, 2573–2588, https://doi.org/10.5194/tc-10-2573-2016, 2016.

d'Orgeval, T., Polcher, J., and de Rosnay, P.: Sensitivity of the West African hydrological cycle in ORCHIDEE to infiltration processes, Hydrol. Earth Syst. Sci., 12, 1387–1401, https://doi.org/10.5194/hess-12-1387-2008, 2008.

Dorigo, W., Gruber, A., De Jeu, R., Wagner, W., Stacke, T., Loew, A., Albergel, C., Brocca, L., Chung, D., Parinussa, R., and Kidd, R.: Evaluation of the ESA CCI soil moisture product using ground-based observations, Remote Sens. Environ., 162, 380–395, https://doi.org/10.1016/j.rse.2014.07.023, 2015.

Druel, A., Peylin, P., Krinner, G., Ciais, P., Viovy, N., Peregon, A., Bastrikov, V., Kosykh, N., and Mironycheva-Tokareva, N.: Towards a more detailed representation of high-latitude vegetation in the global land surface model ORCHIDEE (ORC-HL-VEGv1.0), Geosci. Model Dev., 10, 4693–4722, https://doi.org/10.5194/gmd-10-4693-2017, 2017.

Ekici, A., Beer, C., Hagemann, S., Boike, J., Langer, M., and Hauck, C.: Simulating high-latitude permafrost regions by the JSBACH terrestrial ecosystem model, Geosci. Model Dev., 7, 631–647, https://doi.org/10.5194/gmd-7-631-2014, 2014.

FAO: FAO, IIASA, ISRIC, ISSCAS and JRC: Harmonized World Soil Database (version 1.2), Tech. rep., FAO, Rome, Italy and IIASA, Laxenburg, Austria, 2012.

Fatichi, S., Leuzinger, S., and Körner, C.: Moving beyond photosynthesis: from carbon source to sink-driven vegetation modeling, New Phytol., 201, 1086–1095, https://doi.org/10.1111/nph.12614, https://doi.org/10.1111/nph.12614, 2014.

Fekete, B. M., Vörösmarty, C. J., Roads, J. O., and Willmott, C. J.: Uncertainties in precipitation and their impacts on runoff estimates, J. Climate, 17, 294–304, https://doi.org/10.1175/1520-0442(2004)017<0294:uipati>2.0.co;2, 2004.

Friedl, M. A., Sulla-Menashe, D., Tan, B., Schneider, A., Ramankutty, N., Sibley, A., and Huang, X.: MODIS Collection 5 global land cover: algorithm refinements and characterization of new datasets, Remote Sens. Environ., 114, 168–182, https://doi.org/10.1016/j.rse.2009.08.016, 2010.

Friedlingstein, P., Cox, P., Betts, R., Bopp, L., von Bloh, W., Brovkin, V., Cadule, P., Doney, S., Eby, M., Fung, I., Bala, G., John, J., Jones, C., Joos, F., Kato, T., Kawamiya, M., Knorr, W., Lindsay, K., Matthews, H., Raddatz, T., Rayner, P., Reick, C., Roeckner, E., Schnitzler, K., Schnur, R., Strassmann, K., Weaver, A., Yoshikawa, C., and Zeng, N.: Climate–carbon cycle feedback analysis: results from the C4MIP model intercomparison, J. Climate, 19, 3337–3353, https://doi.org/10.1175/jcli3800.1, 2006.

Gouttevin, I., Krinner, G., Ciais, P., Polcher, J., and Legout, C.: Multi-scale validation of a new soil freezing scheme for a land-surface model with physically-based hydrology, The Cryosphere, 6, 407–430, https://doi.org/10.5194/tc-6-407-2012, 2012a.

Gouttevin, I., Menegoz, M., Domine, F., Krinner, G., Koven, C., Ciais, P., Tarnocai, C., and Boike, J.: How the insulating properties of snow affect soil carbon distribution in the continental pan-Arctic area, J. Geophys. Res., 117, G02020, https://doi.org/10.1029/2011jg001916, 2012b.

Gray, D., Toth, B., Zhao, L., Pomeroy, J., and Granger, R.: Estimating areal snowmelt infiltration into frozen soils, Hydrol. Process., 15, 3095–3111, https://doi.org/10.1002/hyp.320, 2001.

Green, W. H. and Ampt, G.: Studies on soil physics, 1. The flow of air and water through soils, J. Agr. Sci., 4, 1–24, 1911.

Guimberteau, M., Drapeau, G., Ronchail, J., Sultan, B., Polcher, J., Martinez, J.-M., Prigent, C., Guyot, J.-L., Cochonneau, G., Espinoza, J. C., Filizola, N., Fraizy, P., Lavado, W., De Oliveira, E., Pombosa, R., Noriega, L., and Vauchel, P.: Discharge simulation in the sub-basins of the Amazon using ORCHIDEE forced by new datasets, Hydrol. Earth Syst. Sci., 16, 911–935, https://doi.org/10.5194/hess-16-911-2012, 2012.

Haddeland, I., Clark, D. B., Franssen, W., Ludwig, F., Voß, F., Arnell, N. W., Bertrand, N., Best, M., Folwell, S., Gerten, D., Gomes, S., Gosling, S. N., Hagemann, S., Hanasaki, N., Harding, R., Heinke, J., Kabat, P., Koirala, S., Oki, T., Polcher, J., Stacke, T., Viterbo, P., Weedon, G. P., and Yeh, P.: Multimodel estimate of the global terrestrial water balance: setup and first results., J. Hydrometeorol., 12, 869–884, https://doi.org/10.1175/2011jhm1324.1, 2011.

Hansen, M. C., Townshend, J. R. G., DeFries, R. S., and Carroll, M.: Estimation of tree cover using MODIS data at global, continental and regional/local scales, Int. J. Remote Sens., 26, 4359–4380, https://doi.org/10.1080/01431160500113435, 2005.

Heinsch, F. A., Reeves, M., Votava, P., Kang, S., Milesi, C., Zhao, M., Glassy, J., Jolly, W. M., Loehman, R., Bowker, C. F. Kimball, J. S., Nemani, R. R., and Running, S. W.: GPP and NPP (MOD17A2/A3) Products NASA MODIS Land Algorithm, Tech. rep., The University of Montana, Missoula, 2003.

Hengl, T., de Jesus, J. M., MacMillan, R. A., Batjes, N. H., Heuvelink, G. B. M., Ribeiro, E., Samuel-Rosa, A., Kempen, B., Leenaars, J. G. B., Walsh, M. G., and Gonzalez, M. R.: SoilGrids1km – Global Soil Information Based on Automated Mapping, PLOS ONE, 9, 1–17, https://doi.org/10.1371/journal.pone.0105992, 2014.

Hollesen, J., Matthiesen, H., Møller, A. B., and Elberling, B.: Permafrost thawing in organic Arctic soils accelerated by ground heat production, Nat. Clim. Change, 5, 574–578, https://doi.org/10.1038/nclimate2590, 2015.

Hudson, B. D.: Soil organic matter and available water capacity, J. Soil Water Conserv., 49, 189–194, 1994.

Hugelius, G., Tarnocai, C., Broll, G., Canadell, J. G., Kuhry, P., and Swanson, D. K.: The Northern Circumpolar Soil Carbon Database: spatially distributed datasets of soil coverage and soil carbon storage in the northern permafrost regions, Earth Syst. Sci. Data, 5, 3–13, https://doi.org/10.5194/essd-5-3-2013, 2013.

Jarvis, P., Massheder, J., Hale, S., Moncrieff, J., Rayment, M., and Scott, S.: Seasonal variation of carbon dioxide, water vapor, and energy exchanges of a boreal black spruce forest, J. Geophys. Res.-Atmos., 102, 28953–28966, https://doi.org/10.1029/97jd01176, 1997.

Jung, M., Reichstein, M., and Bondeau, A.: Towards global empirical upscaling of FLUXNET eddy covariance observations: validation of a model tree ensemble approach using a biosphere model, Biogeosciences, 6, 2001–2013, https://doi.org/10.5194/bg-6-2001-2009, 2009.

Jung, M., Reichstein, M., Margolis, H., Cescatti, A., Richardson, A., Arain, M., Arneth, A., Bernhofer, C., Bonal, D., Chen, J., Gianelle, D., Gobron, N., Kiely, G., Kutsch, W., Lasslop, G., Law, B. E., Lindroth, A., Merbold, L., Montagnani, L., Moors, E. J., Papale, D., Sottocornola, M., Vaccari, F., and Williams, C.: Global patterns of land-atmosphere fluxes of carbon dioxide, latent heat, and sensible heat derived from eddy covariance, satellite, and meteorological observations, J. Geophys. Res.-Biogeo., 116, G00J07, https://doi.org/10.1029/2010JG001566, 2011.

Kajimoto, T., Matsuura, Y., Osawa, A., Prokushkin, A. S., Sofronov, M. A., and Abaimov, A. P.: Root system development of *Larix gmelinii* trees affected by micro-scale conditions of permafrost soils in central Siberia, Plant Soil, 255, 281–292, https://doi.org/10.1007/978-94-017-2923-9_27, 2003.

Kalnay, E., Kanamitsu, M., Kistler, R., Collins, W., Deaven, D., Gandin, L., Iredell, M., Saha, S., White, G., Woollen, J., Zhu, Y., Leetmaa, A., Reynolds, R., Chelliah, M., Ebisuzaki, W., Higgins, W., Janowiak, J., Mo, K. C., Ropelewski, C., Wang, J., Jenne, R., and Joseph, D.: The NCEP/NCAR 40-year reanalysis project, B. Am. Meteorol. Soc., 77, 437–471, https://doi.org/10.1175/1520-0477(1996)077<0437:tnyrp>2.0.co;2, 1996.

Kleinen, T., Brovkin, V., and Schuldt, R. J.: A dynamic model of wetland extent and peat accumulation: results for the Holocene, Biogeosciences, 9, 235–248, https://doi.org/10.5194/bg-9-235-2012, 2012.

Knyazikhin, Y., Martonchik, J., Diner, D., Myneni, R., Verstraete, M., Pinty, B., and Gobron, N.: Estimation of vegetation canopy leaf area index and fraction of absorbed photosynthetically active radiation from atmosphere-corrected MISR data, J. Geophys. Res.-Atmos., 103, 32239–32256, https://doi.org/10.1029/98jd02461, 1998.

Köchy, M., Hiederer, R., and Freibauer, A.: Global distribution of soil organic carbon – Part 1: Masses and frequency distributions of SOC stocks for the tropics, permafrost regions, wetlands, and the world, Soil, 1, 351–365, https://doi.org/10.5194/soil-1-351-2015, 2015.

Konings, A., Williams, A., and Gentine, P.: Sensitivity of grassland productivity to aridity controlled by stomatal and xylem regulation, Nat. Geosci., 10, 284–288, https://doi.org/10.1038/ngeo2903, 2017.

Körner, C.: Alpine Plant Life: Functional Plant Ecology of High Mountain Ecosystems; with 47 Tables, Springer Science & Business Media, Springer, Berlin, Germany, 2003.

Koster, R. D., Guo, Z., Yang, R., Dirmeyer, P. A., Mitchell, K., and Puma, M. J.: On the nature of soil moisture in land surface models, J. Climate, 22, 4322–4335, https://doi.org/10.1175/2009jcli2832.1, 2009.

Koven, C., Friedlingstein, P., Ciais, P., Khvorostyanov, D., Krinner, G., and Tarnocai, C.: On the formation of high-latitude soil carbon stocks: effects of cryoturbation and insulation by organic matter in a land surface model, Geophys. Res. Lett., 36, l21501, https://doi.org/10.1029/2009GL040150, 2009.

Koven, C. D., Riley, W. J., Subin, Z. M., Tang, J. Y., Torn, M. S., Collins, W. D., Bonan, G. B., Lawrence, D. M., and Swenson, S. C.: The effect of vertically resolved soil biogeochemistry and alternate soil C and N models on C dynamics of CLM4, Biogeosciences, 10, 7109–7131, https://doi.org/10.5194/bg-10-7109-2013, 2013.

Krinner, G., Viovy, N., de Noblet-Ducoudre, N., Ogee, J., Polcher, J., Friedlingstein, P., Ciais, P., Sitch, S., and Prentice, I.: A dynamic global vegetation model for studies of the coupled atmosphere-biosphere system, Global Biogeochem. Cy., 19, 1–33, https://doi.org/10.1029/2003gb002199, 2005.

Krull, E. S., Skjemstad, J. O., and Baldock, J. A.: Functions of soil organic matter and the effect on soil properties, Cooperative Research Centre for Greenhouse Accounting, Glen Osmond, South Australia, 2004.

Landerer, F. W. and Swenson, S.: Accuracy of scaled GRACE terrestrial water storage estimates, Water Resour. Res., 48, W04531, https://doi.org/10.1029/2011wr011453, 2012.

Lauerwald, R., Regnier, P., Camino-Serrano, M., Guenet, B., Guimberteau, M., Ducharne, A., Polcher, J., and Ciais, P.: ORCHILEAK (revision 3875): a new model branch to simulate carbon transfers along the terrestrial–aquatic continuum of the Amazon basin, Geosci. Model Dev., 10, 3821–3859, https://doi.org/10.5194/gmd-10-3821-2017, 2017.

Lawrence, D. M. and Slater, A. G.: Incorporating organic soil into a global climate model, Clim. Dynam., 30, 145–160, https://doi.org/10.1007/s00382-007-0278-1, 2008.

Lawrence, D. M., Slater, A. G., Romanovsky, V. E., and Nicolsky, D. J.: Sensitivity of a model projection of near-surface permafrost degradation to soil column depth and representation of soil organic matter, J. Geophys. Res.-Earth, 113, F02011, https://doi.org/10.1029/2007jf000883, 2008.

Lehner, B. and Döll, P.: Development and validation of a global database of lakes, reservoirs and wetlands, J. Hydrol., 296, 1–22, https://doi.org/10.1016/j.jhydrol.2004.03.028, 2004.

Leinonen, I.: A simulation model for the annual frost hardiness and freeze damage of Scots pine, Ann. Bot.-London, 78, 687–693, https://doi.org/10.1006/anbo.1996.0178, 1996.

Liang, S. and Xiao, Z.: Global Land Surface Products: Leaf Area Index Product Data Collection (1985–2010), Tech. rep., Normal University, Beijing, China, 2012.

Liu, Y. Y., Van Dijk, A. I., De Jeu, R. A., Canadell, J. G., McCabe, M. F., Evans, J. P., and Wang, G.: Recent reversal in loss

of global terrestrial biomass, Nat. Clim. Change, 5, 470–474, https://doi.org/10.1038/nclimate2581, 2015.

Loth, B., Graf, H.-F., and Oberhuber, J. M.: Snow cover model for global climate simulations, J. Geophys. Res., 98, 451–10, https://doi.org/10.1029/93jd00324, 1993.

Luo, Y., Ahlström, A., Allison, S. D., Batjes, N. H., Brovkin, V., Carvalhais, N., Chappell, A., Ciais, P., Davidson, E. A., Finzi, A., Georgiou, K., Guenet, B., Hararuk, O., Harden, J. W., He, Y., Hopkins, F., Jiang, L., Koven, C., Jackson, R. B., Jones, C. D., Lara, M. J., Liang, J., Mcguire, A. D., Parton, W., Peng, C., Randerson, J. T., Salazar, A., Sierra, C. A., Smith, M. J., Tian, H., Todd-Brown, K. E. O., Torn, M., Van Groenigen, K.-J., Wang, Y.-P., West, T. O., Wei, Y., Wieder, W. R., Xia, J., Xu, X., Xu, X., and Zhou, T.: Toward more realistic projections of soil carbon dynamics by Earth system models, Global Biogeochem. Cy., 30, 40–56, https://doi.org/10.1002/2015gb005239, 2016.

Luyssaert, S., Inglima, I., Jung, M., Richardson, A., Reichstein, M., Papale, D., Piao, S., Schulze, E., Wingate, L., Matteucci, G., Aragao, L., Aubinet, M., Beers, C., Bernhofer, C., Black, G., Bonal, D., Bonnefond, J., Chambers, J., Ciais, P., Cook, B., Davis, K., Dolman, A., Gielen, B., Goulden, M., Grace, J., Granier, A., Grelle, A., Griffis, T., Grünwald, T., Guidolotti, G., Hanson, P., Harding, R., Hollinger, D., Hutyra, L., Kolari, P., Kruijt, B., Kutsch, W., Lagergren, F., Laurila, T., Law, B., Le Maire, G., Lindroth, A., Loustau, D., Malhi, Y., Mateu, J., Migliavacca, M., Misson, L., Montagnani, L., Moncrieff, J., Moors, E., Munger, J., Nikinmaa, E., Ollinger, S., Pita, G., Rebmann, C., Roupsard, O., Saigusa, N., Sanz, M., Seufert, G., Sierra, C., Smith, M.-L., Tang, J., Valentini, R., Vesala, T., and Janssens, I. A.: CO_2 balance of boreal, temperate, and tropical forests derived from a global database, Glob. Change Biol., 13, 2509–2537, https://doi.org/10.1111/j.1365-2486.2007.01439.x, 2007.

MacBean, N., Maignan, F., Peylin, P., Bacour, C., Bréon, F.-M., and Ciais, P.: Using satellite data to improve the leaf phenology of a global terrestrial biosphere model, Biogeosciences, 12, 7185–7208, https://doi.org/10.5194/bg-12-7185-2015, 2015.

Magand, C., Ducharne, A., Le Moine, N., and Gascoin, S.: Introducing hysteresis in snow depletion curves to improve the water budget of a land surface model in an Alpine catchment, J. Hydrometeorol., 15, 631–649, https://doi.org/10.1175/jhm-d-13-091.1, 2014.

Manzoni, S. and Porporato, A.: Soil carbon and nitrogen mineralization: theory and models across scales, Soil Biol. Biochem., 41, 1355–1379, https://doi.org/10.1016/j.soilbio.2009.02.031, 2009.

Marcott, S. A., Shakun, J. D., Clark, P. U., and Mix, A. C.: A reconstruction of regional and global temperature for the past 11,300 years, Science, 339, 1198–1201, https://doi.org/10.1126/science.1228026, available at: http://science.sciencemag.org/content/339/6124/1198 (last access: 15 September 2016), 2013.

Martens, B., Miralles, D. G., Lievens, H., van der Schalie, R., de Jeu, R. A. M., Fernández-Prieto, D., Beck, H. E., Dorigo, W. A., and Verhoest, N. E. C.: GLEAM v3: satellite-based land evaporation and root-zone soil moisture, Geosci. Model Dev., 10, 1903–1925, https://doi.org/10.5194/gmd-10-1903-2017, 2017.

McAdam, S. A. and Brodribb, T. J.: The evolution of mechanisms driving the stomatal response to vapor pressure deficit, Plant Physiol., 167, 833–843, https://doi.org/10.1104/pp.114.252940, 2015.

McGuire, A. D., Koven, C., Lawrence, D. M., Clein, J. S., Xia, J., Beer, C., Burke, E., Chen, G., Chen, X., Delire, C., Jafarov, E., MacDougall, A. H., Marchenko, S., Nicolsky, D., Peng, S., Rinke, A., Saito, K., Zhang, W., Alkama, R., Bohn, T. J., Ciais, P., Decharme, B., Ekici, A., Gouttevin, I., Hajima, T., Hayes, D. J., Ji, D., Krinner, G., Lettenmaier, D. P., Luo, Y., Miller, P. A., Moore, J. C., Romanovsky, V., Schädel, C., Schaefer, K., Schuur, E. A., Smith, B., Sueyoshi, T., and Zhuang, Q.: Variability in the sensitivity among model simulations of permafrost and carbon dynamics in the permafrost region between 1960 and 2009, Global Biogeochem. Cy., 30, 1015–1037, https://doi.org/10.1002/2016gb005405, 2016.

Medlyn, B. E., Zaehle, S., De Kauwe, M. G., Walker, A. P., Dietze, M. C., Hanson, P. J., Hickler, T., Jain, A. K., Luo, Y., Parton, W. I., Prentice, I. C., Thornton, P. E., Wang, S., Wang, Y.-P., Weng, E., Iversen, C. M., McCarthy, H. R., Warren, J. M., Oren, R., and Norby, R. J.: Using ecosystem experiments to improve vegetation models, Nat. Clim. Change, 5, 528–534, https://doi.org/10.1038/nclimate2621, 2015.

Michaletz, S. T., Cheng, D., Kerkhoff, A. J., and Enquist, B. J.: Convergence of terrestrial plant production across global climate gradients, Nature, 512, 39–43, https://doi.org/10.1038/nature13470, 2014.

Miralles, D. G., Holmes, T. R. H., De Jeu, R. A. M., Gash, J. H., Meesters, A. G. C. A., and Dolman, A. J.: Global land-surface evaporation estimated from satellite-based observations, Hydrol. Earth Syst. Sci., 15, 453–469, https://doi.org/10.5194/hess-15-453-2011, 2011.

Morris, P. J., Baird, A. J., and Belyea, L. R.: Bridging the gap between models and measurements of peat hydraulic conductivity, Water Resour. Res., 51, 5353–5364, https://doi.org/10.1002/2015WR017264, 2015.

Motoya, K., Masuda, K., Takata, K., and Oki, T.: Sensitivity of precipitation gauge correction for the estimation of the global water balance, Eos Transactions, American Geophysical Union, 83, 2002.

Mualem, Y.: A new model for predicting the hydraulic conductivity of unsaturated porous media, Water Resour. Res., 12, 513–522, https://doi.org/10.1029/WR012i003p00513, 1976.

Muskett, R. R. and Romanovsky, V. E.: Groundwater storage changes in arctic permafrost watersheds from GRACE and in situ measurements, Environ. Res. Lett., 4, 045009, https://doi.org/10.1088/1748-9326/4/4/045009, 2009.

Naudts, K., Ryder, J., McGrath, M. J., Otto, J., Chen, Y., Valade, A., Bellasen, V., Berhongaray, G., Bönisch, G., Campioli, M., Ghattas, J., De Groote, T., Haverd, V., Kattge, J., MacBean, N., Maignan, F., Merilä, P., Penuelas, J., Peylin, P., Pinty, B., Pretzsch, H., Schulze, E. D., Solyga, D., Vuichard, N., Yan, Y., and Luyssaert, S.: A vertically discretised canopy description for ORCHIDEE (SVN r2290) and the modifications to the energy, water and carbon fluxes, Geosci. Model Dev., 8, 2035–2065, https://doi.org/10.5194/gmd-8-2035-2015, 2015.

New, M., Hulme, M., and Jones, P.: Representing twentieth-century space-time climate variability. Part II: Development of 1901–96 monthly grids of terrestrial surface climate, J. Climate, 13, 2217–2238, https://doi.org/10.1175/1520-0442(2000)013<2217:rtcstc>2.0.co;2, 2000.

Ngo-Duc, T., Polcher, J., and Laval, K.: A 53-year forcing data set for land surface models, J. Geophys. Res.-Atmos., 110, D06116, https://doi.org/10.1029/2004JD005434, 2005.

Novick, K. A., Ficklin, D. L., Stoy, P. C., Williams, C. A., Bohrer, G., Oishi, A. C., Papuga, S. A., Blanken, P. D., Noormets, A., Sulman, B. N., Scott, R. L., Wang, L., and Phillips, R. P.: The increasing importance of atmospheric demand for ecosystem water and carbon fluxes, Nat. Clim. Change, 6, 1023–1027, https://doi.org/10.1038/nclimate3114, 2016.

O'Donnell, J. A., Harden, J. W., McGuire, A. D., and Romanovsky, V. E.: Exploring the sensitivity of soil carbon dynamics to climate change, fire disturbance and permafrost thaw in a black spruce ecosystem, Biogeosciences, 8, 1367–1382, https://doi.org/10.5194/bg-8-1367-2011, 2011.

Oki, T., Nishimura, T., and Dirmeyer, P.: Assessment of annual runoff from land surface models using Total Runoff Integrating Pathways (TRIP), J. Meteorol. Soc. Jpn., 77, 235–255, https://doi.org/10.2151/jmsj1965.77.1b_235, 1999.

Olson, R., Johnson, K., Zheng, D., and Scurlock, J.: Global and Regional Ecosystem Modeling: Databases of Model Drivers and Validation Measurements, ORNL Technical Memorandum TM-2001/196, Oak Ridge National Laboratory, Oak Ridge, Tennessee, USA, https://doi.org/10.2172/814241, 2001.

Oren, R., Sperry, J., Katul, G., Pataki, D., Ewers, B., Phillips, N., and Schäfer, K.: Survey and synthesis of intra-and interspecific variation in stomatal sensitivity to vapour pressure deficit, Plant Cell Environ., 22, 1515–1526, https://doi.org/10.1046/j.1365-3040.1999.00513.x, 1999.

Owe, M., de Jeu, R., and Holmes, T.: Multisensor historical climatology of satellite-derived global land surface moisture, J. Geophys. Res.-Earth, 113, F01002, https://doi.org/10.1029/2007jf000769, 2008.

Pan, Y., Chen, J. M., Birdsey, R., McCullough, K., He, L., and Deng, F.: Age structure and disturbance legacy of North American forests, Biogeosciences, 8, 715–732, https://doi.org/10.5194/bg-8-715-2011, 2011.

Papa, F., Prigent, C., and Rossow, W.: Monitoring flood and discharge variations in the large Siberian rivers from a multi-satellite technique, Surv. Geophys., 29, 297–317, https://doi.org/10.1007/s10712-008-9036-0, 2008.

Parton, W., Schimel, D. S., Cole, C., and Ojima, D.: Analysis of factors controlling soil organic matter levels in Great Plains grasslands, Soil Sci. Soc. Am. J., 51, 1173–1179, https://doi.org/10.2136/sssaj1987.03615995005100050015x, 1987.

Parton, W. J., Stewart, J. W., and Cole, C. V.: Dynamics of C, N, P and S in grassland soils: a model, Biogeochemistry, 5, 109–131, https://doi.org/10.1007/bf02180320, 1988.

Peng, S., Piao, S., Ciais, P., Fang, J., and Wang, X.: Change in winter snow depth and its impacts on vegetation in China, Glob. Change Biol., 16, 3004–3013, https://doi.org/10.1111/j.1365-2486.2010.02210.x, 2010.

Peng, S., Ciais, P., Krinner, G., Wang, T., Gouttevin, I., McGuire, A. D., Lawrence, D., Burke, E., Chen, X., Decharme, B., Koven, C., MacDougall, A., Rinke, A., Saito, K., Zhang, W., Alkama, R., Bohn, T. J., Delire, C., Hajima, T., Ji, D., Lettenmaier, D. P., Miller, P. A., Moore, J. C., Smith, B., and Sueyoshi, T.: Simulated high-latitude soil thermal dynamics during the past 4 decades, The Cryosphere, 10, 179–192, https://doi.org/10.5194/tc-10-179-2016, 2016.

Peng, S., Ciais, P., Maignan, F., Li, W., Chang, J., Wang, T., and Yue, C.: Sensitivity of land use change emission estimates to historical land use and land cover mapping, Global Biogeochem. Cy., 31, 626–643, https://doi.org/10.1002/2015GB005360, 2017.

Peterson, B. J., Holmes, R. M., McClelland, J. W., Vörösmarty, C. J., Lammers, R. B., Shiklomanov, A. I., Shiklomanov, I. A., and Rahmstorf, S.: Increasing river discharge to the Arctic Ocean, Science, 298, 2171–2173, 2002.

Piao, S., Luyssaert, S., Ciais, P., Janssens, I. A., Chen, A., Cao, C., Fang, J., Friedlingstein, P., Luo, Y., and Wang, S.: Forest annual carbon cost: a global-scale analysis of autotrophic respiration, Ecology, 91, 652–661, https://doi.org/10.1890/08-2176.1, 2010.

Polcher, J.: Les processus de surface à l'échelle globale et leurs interactions avec l'atmosphère, Habilitation à diriger des recherches, University Pierre et Marie Curie, Paris, France, 2003.

Pomeroy, J. W., Parviainen, J., Hedstrom, N., and Gray, D. M.: Coupled modelling of forest snow interception and sublimation, Hydrol. Process., 12, 2317–2337, https://doi.org/10.1002/(SICI)1099-1085(199812)12:15<2317::AID-HYP799>3.0.CO;2-X, 1998.

Porada, P., Ekici, A., and Beer, C.: Effects of bryophyte and lichen cover on permafrost soil temperature at large scale, The Cryosphere, 10, 2291–2315, https://doi.org/10.5194/tc-10-2291-2016, 2016.

Poulter, B., Ciais, P., Hodson, E., Lischke, H., Maignan, F., Plummer, S., and Zimmermann, N. E.: Plant functional type mapping for earth system models, Geosci. Model Dev., 4, 993–1010, https://doi.org/10.5194/gmd-4-993-2011, 2011.

Poulter, B., MacBean, N., Hartley, A., Khlystova, I., Arino, O., Betts, R., Bontemps, S., Boettcher, M., Brockmann, C., Defourny, P., Hagemann, S., Herold, M., Kirches, G., Lamarche, C., Lederer, D., Ottlé, C., Peters, M., and Peylin, P.: Plant functional type classification for earth system models: results from the European Space Agency's Land Cover Climate Change Initiative, Geosci. Model Dev., 8, 2315–2328, https://doi.org/10.5194/gmd-8-2315-2015, 2015.

Priestley, C. and Taylor, R.: On the assessment of surface heat flux and evaporation using large-scale parameters, Mon. Weather Rev., 100, 81–92, https://doi.org/10.1175/1520-0493(1972)100<0081:otaosh>2.3.co;2, 1972.

Prigent, C., Lettenmaier, D. P., Aires, F., and Papa, F.: Toward a high-resolution monitoring of continental surface water extent and dynamics, at global scale: from GIEMS (Global Inundation Extent from Multi-Satellites) to SWOT (Surface Water Ocean Topography), Surv. Geophys., 37, 339–355, https://doi.org/10.1007/978-3-319-32449-4_7, 2016.

Pulliainen, J.: Mapping of snow water equivalent and snow depth in boreal and sub-arctic zones by assimilating space-borne microwave radiometer data and ground-based observations, Remote Sens. Environ., 101, 257–269, https://doi.org/10.1016/j.rse.2006.01.002, available at: http://www.sciencedirect.com/science/article/pii/S0034425706000241 (last access: 15 September 2016), 2006.

Randerson, J. T., Chen, Y., van der Werf, G. R., Rogers, B. M., and Morton, D. C.: Global burned area and biomass burning emissions from small fires, J. Geophys. Res.-Biogeo., 117, g04012, https://doi.org/10.1029/2012JG002128, 2012.

Rawlins, M. A., Fahnestock, M., Frolking, S., and Vörösmarty, C. J.: On the evaluation of snow water equivalent estimates over the terrestrial Arctic drainage basin, Hydrol. Process., 21, 1616–1623, https://doi.org/10.1002/hyp.6724, 2007.

Rawls, W., Pachepsky, Y., Ritchie, J., Sobecki, T., and Bloodworth, H.: Effect of soil organic carbon on soil water retention, Geoderma, 116, 61–76, https://doi.org/10.1016/S0016-7061(03)00094-6, available at: http://www.sciencedirect.com/science/article/pii/S0016706103000946 (last access: 17 January 2016), quantifying agricultural management effects on soil properties and processes, 2003.

Reynolds, C., Jackson, T., and Rawls, W.: Estimating soil water-holding capacities by linking the Food and Agriculture Organization soil map of the world with global pedon databases and continuous pedotransfer functions, Water Resour. Res., 36, 3653–3662, https://doi.org/10.1029/2000wr900130, 2000.

Ringeval, B., Decharme, B., Piao, S. L., Ciais, P., Papa, F., de Noblet-Ducoudré, N., Prigent, C., Friedlingstein, P., Gouttevin, I., Koven, C., and Ducharne, A.: Modelling sub-grid wetland in the ORCHIDEE global land surface model: evaluation against river discharges and remotely sensed data, Geosci. Model Dev., 5, 941–962, https://doi.org/10.5194/gmd-5-941-2012, 2012.

Rödenbeck, C.: Estimating CO_2 sources and sinks from atmospheric mixing ratio measurements using a global inversion of atmospheric transport, Technical Reports, Max Planck Institute for Biogeochemistry, Jena, Germany, 2005.

Royer, A. and Poirier, S.: Surface temperature spatial and temporal variations in North America from homogenized satellite SMMR-SSM/I microwave measurements and reanalysis for 1979–2008, J. Geophys. Res.-Atmos., 115, d08110, https://doi.org/10.1029/2009JD012760, 2010.

Running, S. W., Nemani, R. R., Heinsch, F. A., Zhao, M., Reeves, M., and Hashimoto, H.: A continuous satellite-derived measure of global terrestrial primary production, BioScience, 54, 547–560, https://doi.org/10.1641/0006-3568(2004)054[0547:acsmog]2.0.co;2, 2004.

Saatchi, S. S., Harris, N. L., Brown, S., Lefsky, M., Mitchard, E. T. A., Salas, W., Zutta, B. R., Buermann, W., Lewis, S. L., Hagen, S., Petrova, S., White, L., Silman, M., and Morel, A.: Benchmark map of forest carbon stocks in tropical regions across three continents, P. Natl. Acad. Sci. USA, 108, 9899–9904, https://doi.org/10.1073/pnas.1019576108, 2011.

Sakumura, C., Bettadpur, S., and Bruinsma, S.: Ensemble prediction and intercomparison analysis of GRACE time-variable gravity field models, Geophys. Res. Lett., 41, 1389–1397, https://doi.org/10.1002/2013GL058632, 2014.

Santoro, M., Beer, C., Cartus, O., Schmullius, C., Shvidenko, A., McCallum, I., Wegmüller, U., and Wiesmann, A.: Retrieval of growing stock volume in boreal forest using hyper-temporal series of Envisat ASAR ScanSAR backscatter measurements, Remote Sens. Environ., 115, 490–507, https://doi.org/10.1016/j.rse.2010.09.018, available at: http://www.sciencedirect.com/science/article/pii/S0034425710002919 (last access: 17 January 2016), 2011.

Santoro, M., Beaudoin, A., Beer, C., Cartus, O., Fransson, J. E., Hall, R. J., Pathe, C., Schmullius, C., Schepaschenko, D., Shvidenko, A., Thurner, M., and Wegmüller, U.: Forest growing stock volume of the northern hemisphere: spatially explicit estimates for 2010 derived from Envisat ASAR, Remote Sens. Environ., 168, 316–334, https://doi.org/10.1016/j.rse.2015.07.005, available at: http://www.sciencedirect.com/science/article/pii/S003442571530064X (last access: 15 September 2016), 2015.

Schaefer, K. and Jafarov, E.: A parameterization of respiration in frozen soils based on substrate availability, Biogeosciences, 13, 1991–2001, https://doi.org/10.5194/bg-13-1991-2016, 2016.

Schulze, E.-D., Lloyd, J., Kelliher, F., Wirth, C., Rebmann, C., Lühker, B., Mund, M., Knohl, A., Milyukova, I., Schulze, W., Ziese, W., Varlagin, A., Sogachev, A., Valentini, R., Dore, S., Grigoriev, S., Kollet, O., Panfyorov, M., Tchebakova, N., and Vygodskaya, N.: Productivity of forests in the Eurosiberian boreal region and their potential to act as a carbon sink – a synthesis, Glob. Change Biol., 5, 703–722, https://doi.org/10.1046/j.1365-2486.1999.00266.x, 1999.

Sherstiukov, A.: Statistical quality control of soil temperature dataset, RIHMI-WDC, 176, 224–232, 2012.

Shiklomanov, A. and Lammers, R.: Record Russian river discharge in 2007 and the limits of analysis, Environ. Res. Lett., 4, 045015, https://doi.org/10.1088/1748-9326/4/4/045015, 2009.

Spahni, R., Wania, R., Neef, L., van Weele, M., Pison, I., Bousquet, P., Frankenberg, C., Foster, P. N., Joos, F., Prentice, I. C., and van Velthoven, P.: Constraining global methane emissions and uptake by ecosystems, Biogeosciences, 8, 1643–1665, https://doi.org/10.5194/bg-8-1643-2011, 2011.

Sturm, M. and Johnson, J. B.: Thermal conductivity measurements of depth hoar, J. Geophys. Res.-Sol. Ea., 97, 2129–2139, https://doi.org/10.1029/91JB02685, 1992.

Swenson, S.: GRACE monthly land water mass grids NETCDF RELEASE 5.0. Ver. 5.0 PO.DAAC, CA, USA, Tech. rep., Dataset, JPL, California, USA, https://doi.org/10.5067/TELND-NC005 (last accessed: 25 January 2016), 2012.

Swenson, S. and Wahr, J.: Post-processing removal of correlated errors in GRACE data, Geophys. Res. Lett., 33, L08402, https://doi.org/10.1029/2005GL025285, 2006.

Swenson, S., Wahr, J., and Milly, P.: Estimated accuracies of regional water storage variations inferred from the Gravity Recovery and Climate Experiment (GRACE), Water Resour. Res., 39, 1223, https://doi.org/10.1029/2002WR001808, 2003.

Takala, M., Pulliainen, J., Metsamaki, S. J., and Koskinen, J. T.: Detection of snowmelt using spaceborne microwave radiometer data in Eurasia from 1979 to 2007, IEEE T. Geosci. Remote, 47, 2996–3007, https://doi.org/10.1109/tgrs.2009.2018442, 2009.

Takala, M., Luojus, K., Pulliainen, J., Derksen, C., Lemmetyinen, J., Kärnä, J.-P., Koskinen, J., and Bojkov, B.: Estimating northern hemisphere snow water equivalent for climate research through assimilation of space-borne radiometer data and ground-based measurements, Remote Sens. Environ., 115, 3517–3529, https://doi.org/10.1016/j.rse.2011.08.014, available at: http://www.sciencedirect.com/science/article/pii/S0034425711003166 (last access: 15 September 2016), 2011.

Tanja, S., Berninger, F., Vesala, T., Markkanen, T., Hari, P., Mäkelä, A., Ilvesniemi, H., Hänninen, H., Nikinmaa, E., Huttula, T., Laurila, T., Aurela, M., Grelle, A., Lindroth, A., Arneth, A., Shibistova, O., and Lloyd, J.: Air temperature triggers the recovery of evergreen boreal forest photosynthesis in spring, Glob. Change Biol., 9, 1410–1426, https://doi.org/10.1046/j.1365-2486.2003.00597.x, 2003.

Tarnocai, C., Canadell, J. G., Schuur, E. A. G., Kuhry, P., Mazhitova, G., and Zimov, S.: Soil organic carbon pools in the northern circumpolar permafrost region, Global Biogeochem. Cy., 23, gB2023, https://doi.org/10.1029/2008GB003327, 2009.

Thonicke, K., Spessa, A., Prentice, I. C., Harrison, S. P., Dong, L., and Carmona-Moreno, C.: The influence of vegetation, fire spread and fire behaviour on biomass burning and trace gas emissions: results from a process-based model, Biogeosciences, 7, 1991–2011, https://doi.org/10.5194/bg-7-1991-2010, 2010.

Thurner, M., Beer, C., Santoro, M., Carvalhais, N., Wutzler, T., Schepaschenko, D., Shvidenko, A., Kompter, E., Ahrens, B., Levick, S. R., and Schmullius, C.: Carbon stock and density of northern boreal and temperate forests, Global Ecol. Biogeogr., 23, 297–310, https://doi.org/10.1111/geb.12125, 2014.

Thurner, M., Beer, C., Carvalhais, N., Forkel, M., Santoro, M., Tum, M., and Schmullius, C.: Large-scale variation in boreal and temperate forest carbon turnover rate related to climate, Geophys. Res. Lett., 43, 4576–4585, https://doi.org/10.1002/2016GL068794, 2016.

Tipping, E., Somerville, C. J., and Luster, J.: The C : N : P : S stoichiometry of soil organic matter, Biogeochemistry, 130, 117–131, https://doi.org/10.1007/s10533-016-0247-z, 2016.

Turner, D. P., Ritts, W. D., Cohen, W. B., Gower, S. T., Running, S. W., Zhao, M., Costa, M. H., Kirschbaum, A. A., Ham, J. M., Saleska, S. R., and Ahl, D. E.: Evaluation of MODIS NPP and GPP products across multiple biomes, Remote Sens. Environ., 102, 282–292, https://doi.org/10.1016/j.rse.2006.02.017, available at: http://www.sciencedirect.com/science/article/pii/S0034425706000873 (last access: 7 October 2016), 2006.

van der Werf, G. R., Randerson, J. T., Giglio, L., Collatz, G. J., Mu, M., Kasibhatla, P. S., Morton, D. C., DeFries, R. S., Jin, Y., and van Leeuwen, T. T.: Global fire emissions and the contribution of deforestation, savanna, forest, agricultural, and peat fires (1997–2009), Atmos. Chem. Phys., 10, 11707-11735, https://doi.org/10.5194/acp-10-11707-2010, 2010.

Van Genuchten, M. T.: A closed-form equation for predicting the hydraulic conductivity of unsaturated soils, Soil Sci. Soc. Am. J., 44, 892–898, https://doi.org/10.2136/sssaj1980.03615995004400050002x, 1980.

Van Wijk, M., Williams, M., Laundre, J., and Shaver, G.: Interannual variability of plant phenology in tussock tundra: modelling interactions of plant productivity, plant phenology, snowmelt and soil thaw, Glob. Change Biol., 9, 743–758, https://doi.org/10.1046/j.1365-2486.2003.00625.x, 2003.

Vörösmarty, C. J., Fekete, B., Meybeck, M., and Lammers, R.: Global system of rivers: its role in organizing continental land mass and defining land-to-ocean linkages, Global Biogeochem. Cy., 14, 599–621, https://doi.org/10.1029/1999gb900092, 2000.

Wagner, W., Lemoine, G., and Rott, H.: A method for estimating soil moisture from ERS scatterometer and soil data, Remote Sens. Environ., 70, 191–207, https://doi.org/10.1016/S0034-4257(99)00036-X, available at: http://www.sciencedirect.com/science/article/pii/S003442579900036X (last access: 15 September 2016), 1999.

Wang, T., Ottlé, C., Boone, A., Ciais, P., Brun, E., Morin, S., Krinner, G., Piao, S., and Peng, S.: Evaluation of an improved intermediate complexity snow scheme in the ORCHIDEE land surface model, J. Geophys. Res.-Atmos., 118, 6064–6079, https://doi.org/10.1002/jgrd.50395, 2013.

Wang, S., Huang, J., Yang, D., Pavlic, G., and Li, J.: Long-term water budget imbalances and error sources for cold region drainage basins, Hydrol. Process., 29, 2125–2136, https://doi.org/10.1002/hyp.10343, 2015.

Wang, T., Peng, S., Krinner, G., Ryder, J., Li, Y., Dantec-Nédélec, S., and Ottlé, C.: Impacts of satellite-based snow albedo assimilation on offline and coupled land surface model simulations, PLoS One, 10, e0137275, https://doi.org/10.1371/journal.pone.0137275, 2015.

Wang, F., Cheruy, F., and Dufresne, J.-L.: The improvement of soil thermodynamics and its effects on land surface meteorology in the IPSL climate model, Geosci. Model Dev., 9, 363-381, https://doi.org/10.5194/gmd-9-363-2016, 2016.

Wang, W., Rinke, A., Moore, J. C., Ji, D., Cui, X., Peng, S., Lawrence, D. M., McGuire, A. D., Burke, E. J., Chen, X., Decharme, B., Koven, C., MacDougall, A., Saito, K., Zhang, W., Alkama, R., Bohn, T. J., Ciais, P., Delire, C., Gouttevin, I., Hajima, T., Krinner, G., Lettenmaier, D. P., Miller, P. A., Smith, B., Sueyoshi, T., and Sherstiukov, A. B.: Evaluation of air–soil temperature relationships simulated by land surface models during winter across the permafrost region, The Cryosphere, 10, 1721–1737, https://doi.org/10.5194/tc-10-1721-2016, 2016.

Wen, L., Nagabhatla, N., Lü, S., and Wang, S.-Y.: Impact of rain snow threshold temperature on snow depth simulation in land surface and regional atmospheric models, Adv. Atmos. Sci., 30, 1449–1460, https://doi.org/10.1007/s00376-012-2192-7, 2013.

Woo, M.-K. and Thorne, R.: Streamflow in the Mackenzie basin, Canada Arctic, 56, 328–340, 2003.

Wutzler, T. and Reichstein, M.: Colimitation of decomposition by substrate and decomposers – a comparison of model formulations, Biogeosciences, 5, 749–759, https://doi.org/10.5194/bg-5-749-2008, 2008.

Xiao, Z., Liang, S., Wang, J., Chen, P., Yin, X., Zhang, L., and Song, J.: Use of general regression neural networks for generating the GLASS leaf area index product from time-series MODIS surface reflectance, IEEE T. Geosci. Remote, 52, 209–223, https://doi.org/10.1109/tgrs.2013.2237780, 2014.

Yang, D., Robinson, D., Zhao, Y., Estilow, T., and Ye, B.: Streamflow response to seasonal snow cover extent changes in large Siberian watersheds, J. Geophys. Res.-Atmos., 108, D18, https://doi.org/10.1029/2002jd003149, 2003.

Yang, D., Kane, D., Zhang, Z., Legates, D., and Goodison, B.: Bias corrections of long-term (1973–2004) daily precipitation data over the northern regions, Geophys. Res. Lett., 32, L19501, https://doi.org/10.1029/2005gl024057, 2005.

Yin, X. and Struik, P.: C_3 and C_4 photosynthesis models: an overview from the perspective of crop modelling, NJAS-Wagen. J. Life Sc., 57, 27–38, 2009.

Yoshimura, K. and Kanamitsu, M.: Dynamical global downscaling of global reanalysis, Mon. Weather Rev., 136, 2983–2998, https://doi.org/10.1175/2008mwr2281.1, 2008.

Yue, C., Ciais, P., Cadule, P., Thonicke, K., Archibald, S., Poulter, B., Hao, W. M., Hantson, S., Mouillot, F., Friedlingstein, P., Maignan, F., and Viovy, N.: Modelling the role of fires in the terrestrial carbon balance by incorporating SPITFIRE into the global vegetation model ORCHIDEE – Part 1: simulating histor-

ical global burned area and fire regimes, Geosci. Model Dev., 7, 2747-2767, https://doi.org/10.5194/gmd-7-2747-2014, 2014.

Yue, C., Ciais, P., Cadule, P., Thonicke, K., and van Leeuwen, T. T.: Modelling the role of fires in the terrestrial carbon balance by incorporating SPITFIRE into the global vegetation model ORCHIDEE – Part 2: Carbon emissions and the role of fires in the global carbon balance, Geosci. Model Dev., 8, 1321–1338, https://doi.org/10.5194/gmd-8-1321-2015, 2015.

Zhao, M., Heinsch, F. A., Nemani, R. R., and Running, S. W.: Improvements of the MODIS terrestrial gross and net primary production global data set, Remote Sens. Environ., 95, 164–176, https://doi.org/10.1016/j.rse.2004.12.011, available at: http://www.sciencedirect.com/science/article/pii/S0034425705000106 (last access: 7 October 2016), 2005.

Zhao, M., Running, S. W., and Nemani, R. R.: Sensitivity of Moderate Resolution Imaging Spectroradiometer (MODIS) terrestrial primary production to the accuracy of meteorological reanalyses, J. Geophys. Res.-Biogeo., 111, g01002, https://doi.org/10.1029/2004JG000004, 2006.

Zhao, Y., Ciais, P., Peylin, P., Viovy, N., Longdoz, B., Bonnefond, J. M., Rambal, S., Klumpp, K., Olioso, A., Cellier, P., Maignan, F., Eglin, T., and Calvet, J. C.: How errors on meteorological variables impact simulated ecosystem fluxes: a case study for six French sites, Biogeosciences, 9, 2537–2564, https://doi.org/10.5194/bg-9-2537-2012, 2012.

Zhou, S., Medlyn, B., Sabaté, S., Sperlich, D., and Prentice, I. C.: Short-term water stress impacts on stomatal, mesophyll and biochemical limitations to photosynthesis differ consistently among tree species from contrasting climates, Tree Physiol., 34, 1035–46, https://doi.org/10.1093/treephys/tpu072, 2014.

Zhu, D., Peng, S. S., Ciais, P., Viovy, N., Druel, A., Kageyama, M., Krinner, G., Peylin, P., Ottlé, C., Piao, S. L., Poulter, B., Schepaschenko, D., and Shvidenko, A.: Improving the dynamics of Northern Hemisphere high-latitude vegetation in the ORCHIDEE ecosystem model, Geosci. Model Dev., 8, 2263–2283, https://doi.org/10.5194/gmd-8-2263-2015, 2015.

Zhu, D., Peng, S., Ciais, P., Zech, R., Krinner, G., Zimov, S., and Grosse, G.: Simulating soil organic carbon in yedoma deposits during the Last Glacial Maximum in a land surface model, Geophys. Res. Lett., 43, 5133–5142, https://doi.org/10.1002/2016gl068874, 2016.

Zhu, Z., Bi, J., Pan, Y., Ganguly, S., Anav, A., Xu, L., Samanta, A., Piao, S., Nemani, R. R., and Myneni, R. B.: Global data sets of vegetation leaf area index (LAI) 3g and Fraction of Photosynthetically Active Radiation (FPAR) 3g derived from Global Inventory Modeling and Mapping Studies (GIMMS) Normalized Difference Vegetation Index (NDVI3g) for the period 1981 to 2011, Remote Sens., 5, 927–948, https://doi.org/10.3390/rs5020927, 2013.

Zimov, S. A., Zimova, G. M., Daviodov, S. P., Daviodova, A. I., Voropaev, Y. V., Voropaeva, Z. V., Prosiannikov, S. F., Prosiannikova, O. V., Semiletova, I. V., and Semiletov, I. P.: Winter biotic activity and production of CO_2 in Siberian soils: a factor in the greenhouse effect, J. Geophys. Res.-Atmos., 98, 5017–5023, https://doi.org/10.1029/92JD02473, 1993.

Zimov, N. S., Zimov, S. A., Zimova, A. E., Zimova, G. M., Chuprynin, V. I., and Chapin, F. S.: Carbon storage in permafrost and soils of the mammoth tundra-steppe biome: role in the global carbon budget, Geophys. Res. Lett., 36, l02502, https://doi.org/10.1029/2008gl036332, 2009.